Hadronic Fragmentation Studies in ep Scattering at HERA

Keith Thomas Donovan

Department of Physics,
Queen Mary and Westfield College,
University of London

A thesis submitted in accordance with the regulations for the Degree of Doctor of Philosophy in the University of London

December 7, 1998

Abstract

Deep inelastic ep scattering (DIS) data recorded in 1996 using the H1 detector at HERA are analysed in the Breit frame of reference. A review of the theory relevant to this thesis and a description of the detector are included.

The details behind the author's publication of a test on the jet finding cone algorithm are given. This test was performed by examining the algorithm's performance when it operates over a random distribution of particles in a detector. The resulting distributions, particularly the energy profiles, show similar trends to published spectra from various sources.

The event shape variable Thrust (T_z) is studied in the current hemisphere of the Breit frame. A method is devised for obtaining the proportion of gluons in the proton (BGF events) as a function of $x_{Bjorken}$, effectively the fraction of the proton's four–momentum carried by the struck quark. This is achieved by comparison with Monte Carlo models.

Rapidity, pseudo–rapidity and invariant energy spectra are examined in the Breit frame. Comparisons are made with various "Monte Carlo" simulation models and to MLLA/LPHD predictions. The rapidity distributions do not show the trends predicted by some theories at low particle transverse momentum. The invariant energy distributions show fair agreement with MLLA/LPHD predictions made for e^+e^- data over a wide range of energy scales; the data move closer to the prediction as energy scale increases and/or as selections are made to remove leading order processes.

Declaration

No portion of the work referred to in this thesis has been submitted in support of an application for another degree or qualification of this or any other institute of learning.

Copyright

Contents

List of Figures

List of Tables

For my Faye.

Preface

This thesis has two distinct aspects. The major section examines various spectra resulting from electron–proton (and positron–proton) scattering at HERA but other topics are considered. The HERA analysis uses data taken by the H1 detector in the 1996 run period and examines it in the Breit frame of reference. The result of the thesis is not a calculated number but rather a series of figures which are compared to theory.

Chapter one gives details of the HERA collider and the H1 detector. Particular attention is paid to the areas of the detector that are used in the analysis. Chapter two describes the kinematics and physics processes occurring at HERA and concentrates on DIS processes that are examined later in the analysis. QCD predictions are discussed further in Chapter three, which goes on to review the Monte Carlo models that are later compared to data.

Chapter four is not part of the H1 analysis and is based on a two author paper which explores how the jet–finding cone algorithm deals with random noise in a typical calorimeter system and compares its findings to results published by a variety of experiments.

The event selection and the cuts that are applied to the data and Monte Carlo are given in Chapter five and the Breit frame is described in Chapter six. Chapter seven details how the data are corrected using Monte Carlo models and gives the of resolution and purity of variables used later in the analysis.

The event shape variable Thrust (T_z) is studied in Chapter eight. A method is devised for obtaining the proportion of gluons in the proton (BGF events) as a function of $x_{Bjorken}$. This is achieved by comparison with Monte Carlo models.

Rapidity, pseudo–rapidity and invariant energy spectra are examined in the Breit frame in Chapter nine. This work has been published in a paper, a conference paper and in another paper to be published in the near future.

Chapter 1

The H1 Detector

1.1 HERA

The HERA [1] ring is 6.3 km in circumference and lies 20 metres below ground. It consists of two independent accelerators which were designed to accelerate and store electrons (throughout this thesis electrons and positrons will be referred to, generically, as electrons) at an energy of 30 GeV and protons at 820 GeV. The counter rotating beams have zero degree crossing at four interaction points equally spaced around the HERA ring. H1 is situated in the North Hall (see Fig. 1.1).

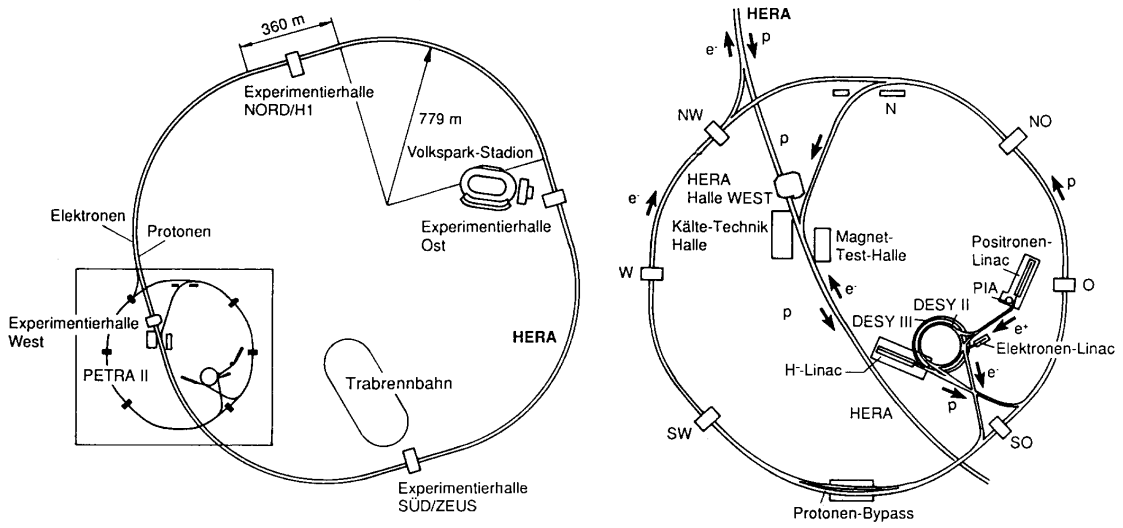

Figure 1.1: *Schematic view of the HERA accelerator.*

During the 1996 run period the energy of the positrons was 27.5 GeV and the proton

energy was 820 GeV giving a total centre of mass energy $\sqrt{s} = 314$ GeV. HERA was filled with 175 paired bunches and in addition there were 14 unpaired positron and 6 unpaired proton 'pilot' bunches, used for calibration and background monitoring studies. The bunch crossing time at HERA is 96 ns.

The electrons and protons both go through a chain of pre–accelerators before injection into the main ring. The electrons are first accelerated by a 500 MeV linear accelerator before injection into a small storage ring. The electrons are then allowed to accumulate into a single bunch of 60 mA and are then injected into DESY II. From there, they are again accelerated to 7 GeV and injected into PETRA II which is filled with 70 bunches at a rate of 12.5 Hz. These bunches can then be injected into the HERA main ring. The accelerating procedure is repeated two more times so HERA can be filled with up to 210 bunches, typically producing a current of 40 mA. For the protons a 50 MeV linear accelerator strips negatively charged hydrogen ions of electrons and injects them into DESY III. Once inside DESY III they are accelerated to 7.5 GeV and then injected into PETRA II and from there they are accelerated once again this time to 40 GeV before the final transfer to the HERA main ring. Typically between 190 and 210 bunches are injected with a current of around 80 mA.

Two experiments H1 and ZEUS have been built to detect electron–proton collisions. These are located in the North and South Halls respectively (see Fig. 1.1). The other two Halls are taken up by HERMES and HERA–B. HERMES is in the East Hall and examines collisions between a polarised electron beam and atomic beams in order to make measurements on the polarised nucleon structure functions. HERA–B is situated in the West hall and will investigate collisions between the proton beam halo and wires placed inside the beam pipe, primarily as a B meson "factory".

1.2 H1

The H1 detector [2, 3] is an all purpose 4π detector designed to investigate all the processes originating from electron–proton interactions. A $r - z$ view of the H1 detector is shown in Fig. 1.2.

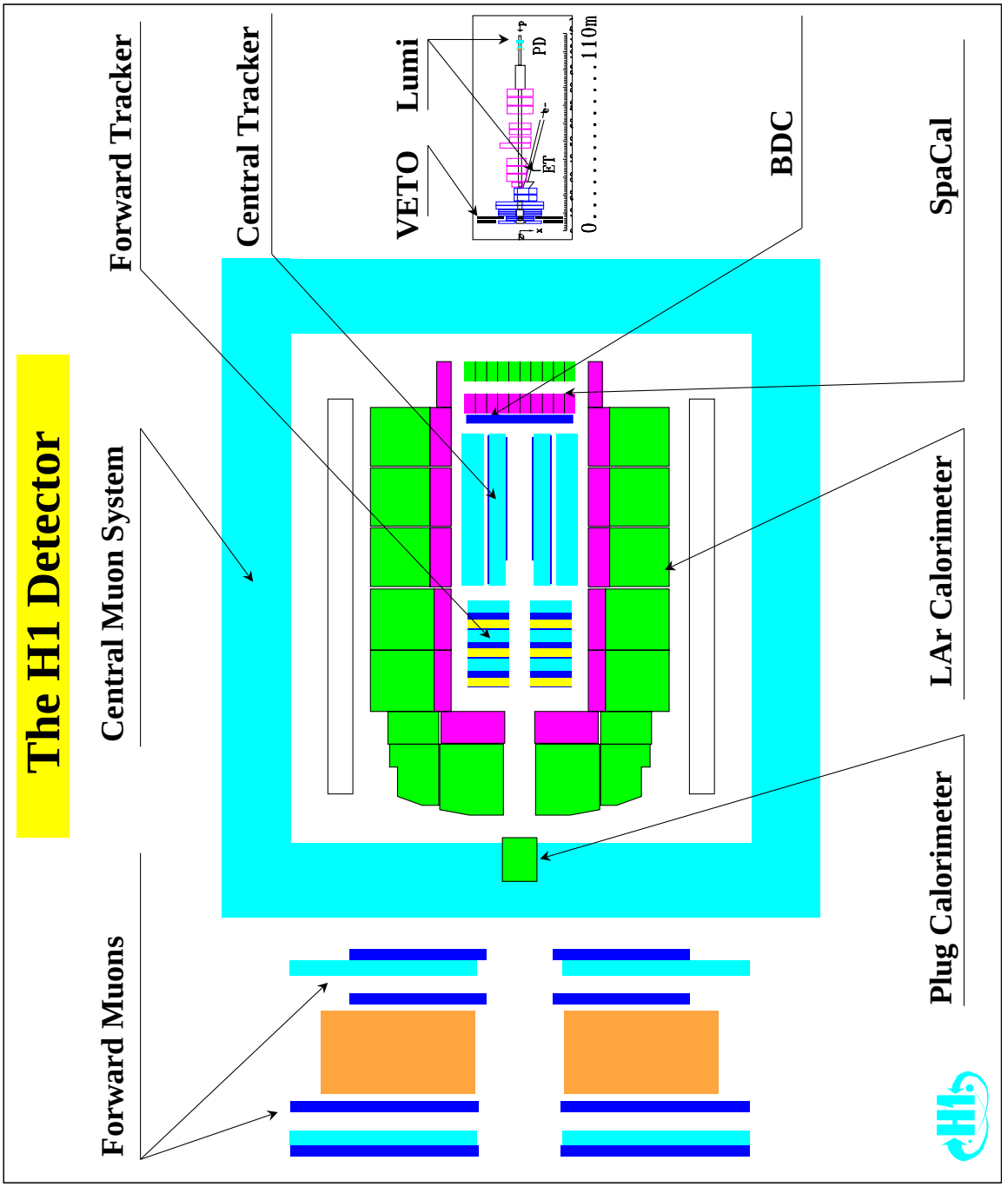

Figure 1.2: *The H1 Detector (r–z view).*

H1 uses a right handed coordinate system with the z–axis running parallel to the beams and the incoming proton beam pointing in the positive z direction. The polar angle θ is measured with respect to the z–axis so a proton which has not scattered has an angle $\theta = 0$ and is said to be going in the 'forward' direction, similarly a non–scattered electron ($\theta = \pi$) is going in the backward direction. The positive x–axis is then towards the centre of the HERA ring and the positive y direction is vertically straight up.

The H1 detector has an asymmetric design to match the asymmetric beam energies. The detector is thus more densely instrumented in the forward direction to measure the larger multiplicities and energy flow in the direction of the proton. The backward region is designed to measure the momentum and energy of the scattered electron, these quantities are important in determining the kinematics of a particular event.

The detector has a uniform 1.15 T magnetic field produced by a superconducting solenoid outside the calorimeters. The momenta of charged particles are determined by the tracking detectors which determine the curvature of the particles' trajectories in this field. The tracking in the central area of the detector is performed by two jet and two z drift chambers and in the forward direction by three planar and three radial drift chamber modules. H1 also has a backward drift chamber and a silicon vertex detector close to the beam pipe, these were added in the 1994/1995 winter shutdown of the experiment.

Energy measurements are made by the liquid argon calorimeter, the spaghetti calorimeter (SpaCal), and the plug calorimeter. These are surrounded by the instrumented iron return yoke, also known as the 'tail catcher' since it detects any hadronic energy escaping out of the main calorimeters. The instrumented iron also identifies muons as does the forward muon system which lies either side of a magnetised toroid at the front of the experiment.

The luminosity system consists of a electron tagger and a photon tagger, these are located in the backward direction 33 m and 103 m, respectively, from the interaction point. The luminosity is determined by measuring the rate of the Bethe–Heitler process $ep \to ep\gamma$.

1.3 Tracking

The asymmetry between the electron and proton beam energies at HERA means that many charged particles are produced in the forward direction at small angles. This divides the tracking detectors of H1 into three regions so that good triggering and reconstruction efficiency can be maintained over the whole detector. These three regions are covered by the Forward Tracking Detector (FTD), the Central Tracking Detector (CTD) and the Backward Drift Chamber (BDC) see Fig. 1.3.

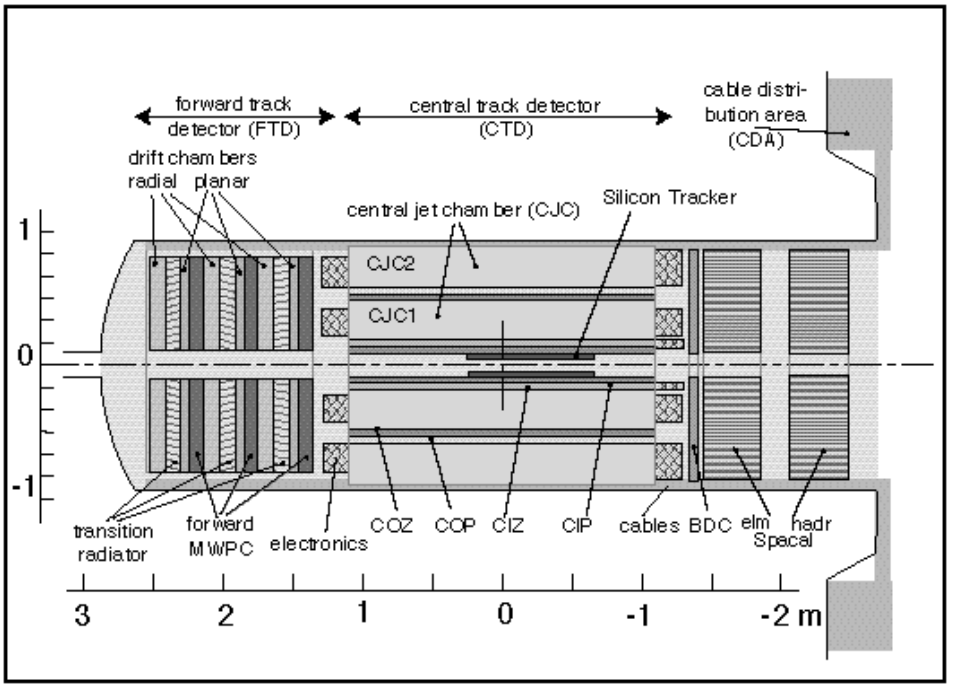

Figure 1.3: *The H1 trackers (r–z view).*

1.3.1 The Central Tracker

The Central Tracking Detector is made up of a number of different elements. Track reconstruction is performed by two concentric drift chambers, the inner Central Jet Chamber, CJC1 ($200 < r < 453.5$ mm) and the outer Central Jet Chamber, CJC2 ($527 < r < 843$ mm). The wires of these detectors, which run parallel to the beam pipe, are grouped into drift cells which are shifted 30° from the radial direction. This improves track resolution by ensuring that the ionisation electrons drift perpendicular to the high momentum tracks in the ambient magnetic field and resolves the left–right ambiguity. The two chambers

cover the region $25° < \theta < 155°$ and achieve a resolution in the $r - \phi$ plane of 170 μm. By comparing the arrival time of the signals at each end of the wire the z–coordinate may be measured with a resolution equal to 1% of the length of the wire (≈ 2 cm). See Fig. 1.4.

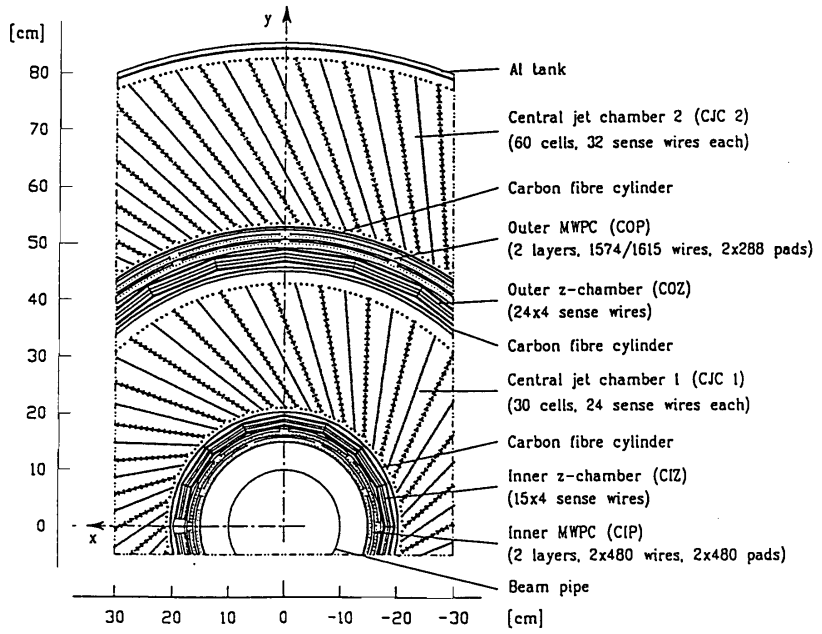

Figure 1.4: *The Central tracker.*

To improve track resolution in the z–direction there are two smaller drift chambers. The Central Inner Z–chamber, CIZ ($173 < r < 193$ mm, $16° < \theta < 169°$), lies inside CJC1 and the Central Outer Z–chamber, COZ ($456 < r < 480$ mm, $25° < \theta < 156°$), lies between CJC1 and CJC2, which means that the chambers can be used for mutual calibration. The CIZ and COZ typically have a resolution of 300 μm in the z–direction and between 4° and 7° in ϕ.

The CIZ is constructed in 17 regions in ϕ forming a polygon ring arrangement. There are 15 rings in the z direction, each of which is 12 cm long. Each of the 4 sense wires is inclined at 45° to the chamber axis and the wires point back at the interaction region. Tracks originating at the interaction point will thus travel along the plane of the wires. In the polar range $20° < \theta < 170°$ the z resolution in the CIZ is 320 μm.

The COZ has a similar structure to the CIZ except that it has 24 regions in ϕ and 24 rings in the z direction, each of length 9 cm. Again the COZ has four sense wires but they are not staggered and are strung at a constant z coordinate so the left–right

ambiguity has to be removed by software. The z resolution is dependent on the angle at which the particle enters the sub–detector, and is maximum at a polar angle of 90° where $\sigma \approx 200$ μm but decreases to $\sigma \approx 500$ μm for low crossing angles.

Central Tracker trigger information is provided by two proportional chambers. Tracks that originate from the interaction point trigger the proportional chambers. The Central Inner Proportional chamber (CIP) is inside CJC1 and the Central Outer Proportional chamber (COP) is between the CJC2 and the COZ. (see Fig. 1.4). Both the CIP and the COP consist of two layers of proportional chambers with the inner layer rotated by 22.5° relative to the outer layer. The time resolution of the proportional chambers is ≤ 75 ns as determined using cosmic ray events.

1.3.2 The Forward Tracker

The Forward Tracking Detector covers the region $5° < \theta < 30°$, and consists of three identical supermodules. Each supermodule contains planar and radial drift chambers, proportional chambers and transition radiators, (see Fig. 1.5). The Forward Tracker has to exist in a quite hostile environment; the primary track multiplicity in this region is between 10–15 for a typical event, and many secondary events are produced from interactions with the end wall of the CJC.

The planar drift chambers are situated nearest to the interaction point in each of the supermodules. The planar chambers are made up of three layers, the wires in each layer being perpendicular to the beam axis but rotated through 60° with respect to the previous layer. Each planar module achieves an angular resolution in the $x - y$ plane of less than 1 mrad. This precision in the $x - y$ plane allows tracks which pass through both the central and forward trackers to be linked together.

The next chambers in each supermodule in the direction away from the interaction point are the multi–wire proportional chambers (MWPC). These are used for triggering and bunch crossing timing. The MWPCs comprise two planes of wires interleaved with three cathode pads. Each pad is segmented into 20 annuli; the 16 innermost annuli are themselves segmented azimuthally into sections of $\pi/8$ and the 4 outermost pads are segmented so that each pad covers an azimuthal angle of $\pi/16$. A track that travels through all three MWPC modules will fall into the polar angular region $6.6° < \theta < 18.0°$ while a track which goes through two of the three modules will be in the range $5.1° < \theta < 21.6°$. The time resolution of these tracks has been measured at 20 ns, which is much

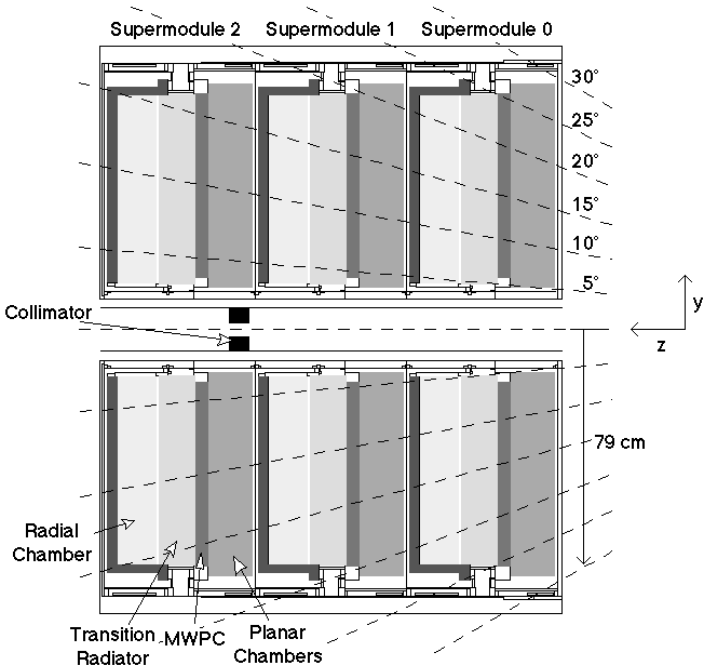

Figure 1.5: *The Forward tracker.*

less than the bunch crossing rate.

The transition radiator (TR) is the next chamber encountered. These chambers consist of 400 polypropylene foils which produce X–rays when a particle of sufficiently high velocity (γ) passes through them. The most forward chamber in each supermodule is the radial drift chamber. In principle these detect the photons produced in the TRs and can use the information to distinguish between electrons and pions. This can be done because the rate at which X-rays are produced is proportional to γ, which is much larger for electrons. The X-rays produced by TRs have an energy spectrum which peaks at around 6 keV for 20 GeV electrons. Test beams have shown that given the right gas mixtures a 90% electron acceptance can be achieved with only 10% pion contamination providing the track has a momentum less than 80 GeV and it passes through all three supermodules of the FTD. The radial geometry of the wires gives a precise momentum measurement with a resolution of $\sigma_p/p^2 < 0.003$ GeV^{-1}. The second and third radials are rotated by 3.75° and 2.5° respectively, to ensure a track does not travel along a cathode plane.

1.3.3 The Backward Drift Chamber

The Backward Drift Chamber (BDC) is situated just in front of SpaCal. The BDC replaced the Backward Proportional Chamber (BPC) during the 1994–1995 shutdown of the experiment. The BDC consists of four double layers, which are arranged into different stereo views each of which is rotated by 11.25° with respect to the previous layer. It has a much better resolution than the BPC and also provides trigger information for the trigger level 1 (unlike the BPC).

1.3.4 The Silicon Tracker

The Silicon Tracker is divided into two sections, the central part (CST) and the backward silicon tracker (BST). Both of these were installed in the detector during the winter 1994–1995 shutdown. They are both positioned close to the beam between the beam pipe and the central tracker. The CST is designed to improve vertex determination whilst the BST is used to improve reconstruction of backward small angle tracks (i.e. θ close to 180°).

1.4 The H1 Magnet

The magnetic field inside the H1 detector is provided by four super–conducting solenoids. The magnets have a diameter of $\sim$ 6m and are situated outside the calorimetry.

Each magnet consists of the super–conducting material (a Niobium–Titanium composite bound in copper) which is then clad in aluminium and wound on an aluminium former for support. The instrumented iron tail catcher serves as a flux return for the magnetic field. The magnetic force on each end cap of the instrumented iron is approximately 1500 tonnes. Mapping of the magnetic field has shown that in the sensitive tracking region the field varies by less than 3% with an average value of 1.15 Tesla.

1.5 Calorimetry

The calorimetry in H1 was designed to complement the tracking detectors. The calorimeters were designed for energy measurement, to identify electrons and for accurate mea-

surement of jets with high particle densities. The resolution of calorimeters improves at higher energies (as $1/\sqrt{E}$) while the momentum resolution of the trackers degrades as the particles are bent less in the magnetic field. The calorimeters also measure the energy of neutral hadrons which the trackers can not detect. The calorimetry consists of the Liquid Argon (LAr) Calorimeter which covers the central and forward regions and the Spaghetti Calorimeter (SpaCal) which occupies the backward region. Additionally there is a forward plug calorimeter in the proton direction and the instrumented iron tail catcher which measures hadronic leakage from the LAr and the SpaCal.

1.5.1 The Liquid Argon Calorimeter

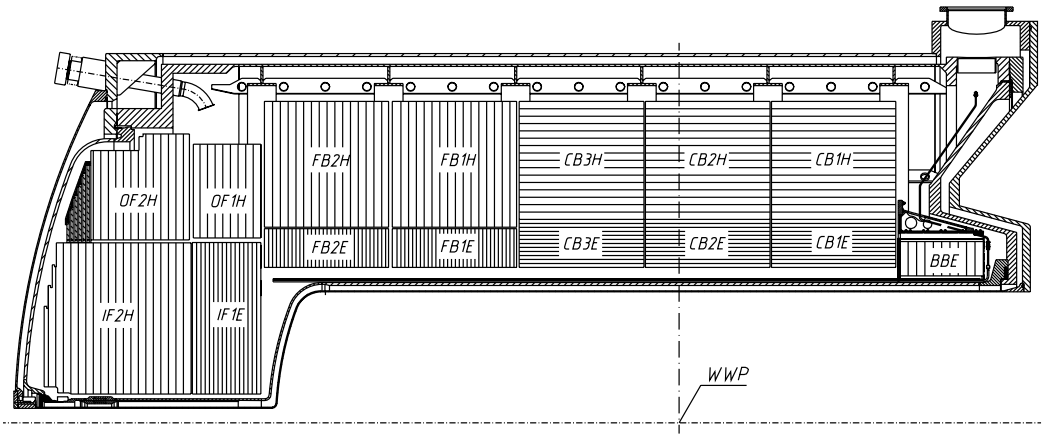

Figure 1.6: *The Liquid Argon Calorimeter.*

The Liquid Argon Calorimeter, LAr, covers the angular region $4° < \theta < 153°$. (see Fig. 1.6). It is divided into two parts, an inner electromagnetic section and an outer hadronic section. The electromagnetic section has lead plates as absorbers and has a depth of 20-30 radiation lengths and the hadronic section has steel absorbers with a total depth of 4.5 to 8 interaction lengths.

The calorimeter is divided into eight "wheels", each of which is self–supporting. Six of the wheels are in the barrel region and are segmented into eight stacks or octants in ϕ. The LAr has good segmentation with 45000 cells. The energy resolution determined

using test beams is $12\%/\sqrt{E(\mathrm{GeV})} \oplus 1\%$ for electrons and $45\%/\sqrt{E(\mathrm{GeV})} \oplus 1\%$ for pions. The calorimeter is non–compensating with the response to hadrons approximately 30% less than that for electrons. This is corrected by a weighting procedure during offline reconstruction. The electromagnetic energy scale has been measured to a precision of 3%, determined by comparing the energy deposited in the calorimeter with the corresponding measurement for track momentum. The hadronic energy scale is known to a precision of 6%, as determined by investigating the average transverse momentum balance between the hadronic system and the scattered electron.

1.5.2 SpaCal

The Lead/Scintillating–fibre Calorimeter or Spaghetti Calorimeter (SpaCal) was installed in the backward region of the H1 detector during the 1994/1995 winter shutdown (see Fig. 1.7). The SpaCal was designed to replace the Backward Electro–Magnetic Calorimeter (BEMC) and the QMW Time–of–Flight (ToF) device. It has a good angular resolution and an energy resolution of better than 0.7% for a 27.5 GeV electron. The SpaCal's principal tasks are to identify and accurately measure the scattered lepton in "low" momentum transfer DIS events as well as measuring the hadrons produced in photoproduction events and to be capable of providing time information to suppress background events at the first trigger level.

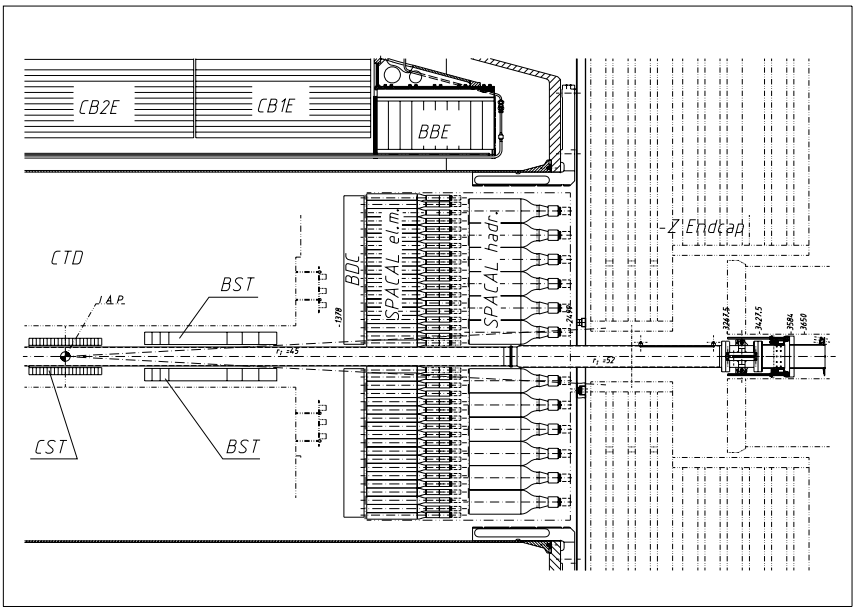

Figure 1.7: *The Lead/Scintillating–fibre Calorimeter (SpaCal).*

The SpaCal is made up of an electromagnetic and a hadronic section and has an angular acceptance of $153^\circ < \theta < 177.5^\circ$. The electromagnetic section is constructed from 0.5 mm radius scintillating plastic fibres embedded in a lead absorber matrix. This produces a lead–to–fibre ratio of 2.3 : 1 in the electromagnetic section. The light from the fibres is read out by photomultipliers, producing a time resolution of better than 1 ns together with a low noise level. The electromagnetic section is 28 radiation lengths deep and the high sampling frequency, due to the narrow fibres, allows an energy resolution of $7.5\%/\sqrt{E(\mathrm{GeV})}$ as well as millimetre spatial precision to be achieved. The hadronic section is made in a similar way but with a fibre radius of 1 mm to give a lead–to–fibre ratio of 3.4 : 1. The hadronic section adds 1.02 interaction lengths of material to the electromagnetic section, which is 1.0 interaction length deep; the energy resolution for hadrons is $\sigma_E/E = 30\%/\sqrt{E(\mathrm{GeV})}$.

1.5.3 The Plug Calorimeter

The Plug Calorimeter is situated close to the beam pipe in the forward direction. It was designed to fill the gap in acceptance between the forward liquid argon calorimeter and the beam pipe and so covers the region $0.7^\circ < \theta < 3.5^\circ$. The purpose of the plug is to minimise loss of transverse momentum, which is particularly important in charged current events where the event kinematics can only be determined from the hadronic final state.

The plug is made up of 9 layers of copper absorber plates sandwiched with 8 layers of silicon detector. It has a total depth of 4.3 interaction lengths. Due to lateral and longitudinal shower leakage and coarse sampling the resolution of the plug is only $150\%/\sqrt{E(\mathrm{GeV})}$.

1.5.4 The Instrumented Iron

The Instrumented Iron return yoke measures the amount of hadronic energy leaking out of the LAr calorimeter and so is usually known as the tail catcher. Streamer tubes are placed between the layers of the iron yoke to detect muon tracks and hadronic showers in the region $5^\circ < \theta < 175^\circ$. The tail catcher has a total depth of 4.5 interaction lengths and the hadronic energy resolution has been measured to be $150\%/\sqrt{E(\mathrm{GeV})}$.

1.6 Forward Muons

The Forward Muon Detector (FMD) is designed to detect high energy muons produced in the forward direction in the region $3^\circ < \theta < 17^\circ$ with a momentum between 5 and 200 GeV. The FMD consists of three double layered drift chambers each side of a toroidal magnet. Muons that reach the FMD have to travel through a large amount of dead material first. This is responsible for the lower limit on the measured muon momentum. The upper limit is set by the magnetic field strength of the toroid. Muons which have momentum below the 5 GeV limit would be detected in the Forward Tracker. The resolution of the Forward Muon Detector is $dp/p \approx 0.3$. The forward muons can also be used to detect particles produced in secondary interactions with collimators. These collimators protect the detector from synchrotron radiation.

1.7 Luminosity System

The Luminosity System [4] consists of two low angle crystal calorimeters, the electron tagger and the photon tagger, placed at -33 m and -103 m, respectively. The luminosity system relies on the Bethe–Heitler reaction $ep \to ep\gamma$. As both the photon and the electron are detected, two different methods can be used to calculate the luminosity. The main source of background is bremsstrahlung from the beam gas, $eA \to eA\gamma$, which occurs at approximately 10% of the Bethe–Heitler rate, but can be removed by using data from the electron pilot bunches. The luminosity is given by:

$$\mathcal{L} = \frac{R_{tot} - (I_{tot}/I_0)R_0}{\sigma_{vis}}$$

where R_{tot} is the total rate of the bremsstrahlung events, R_0 is the rate of electron pilot bunches, I_{tot} and I_0 are the corresponding electron beam currents and σ_{vis} is the visible part of the Bethe–Heitler cross section.

The two methods used to determine event rate are the coincidence method, which requires detection of the electron and the photon, and the single photon method, which counts the rate of photons above a certain threshold energy. The electrons are deflected into the electron tagger by a set of warm quadrupoles and a bending magnet situated in the region $-5.8 < z < -23.8$ m. The photons enter the photon detector via the photon exit window in the beam pipe which is located at $z = -92.3$ m. A layout of the luminosity system can be seen in Fig. 1.8 and the luminosity produced by HERA during its operation

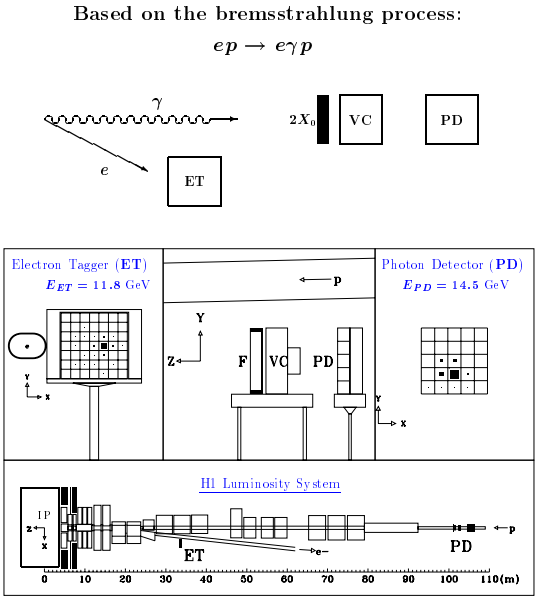

Figure 1.8: *The layout of the H1 Luminosity System.*

can be seen in table 1.1.

1.8 Trigger and Readout

The purpose of the H1 trigger is to distinguish between electron–proton physics events and background processes. The multilevel trigger system also separates different event classes such as DIS and photoproduction and scales low Q^2 processes. Due to the high bunch crossing rate and to keep dead time to a minimum the trigger system is "pipe–lined." Pipe lining means that the output signals from the various sub–detectors are fed into front end digitising units for storage. The same output signals are also fed into the sub–detector trigger where conversion to "trigger elements" takes place. The trigger elements are then sent to the central trigger logic. Here the signals are combined to make the level 1 and level 2 triggers. The level 1 trigger has nine elements each relating to a particular detector sub–trigger. When an event satisfies the selection criteria, and is worth further examination, a "keep" signal is sent out. This is sent for possible physics events or other events of interest that could be used for detector calibration such as cosmic ray events. When the keep signal is sent, the detector read outs are disabled and the information in

year	e^+/e^-	$\langle z \rangle$ (cm)	$\langle I_e \rangle$ (mA)	$\langle I_p \rangle$ (mA)	$\langle L_{sp} \rangle$ ($\mathrm{cm^{-2}s^{-1}mA^{-1}}$)	$\int L_{\mathrm{HERA}}$ ($\mathrm{pb^{-1}}$)	$\int L_{\mathrm{H1}}$ ($\mathrm{pb^{-1}}$)
1992	e^-	-	1.40	1.07	1.87×10^{29}	0.055	0.030
1993	e^-	-5.7	7.72	10.79	3.15×10^{29}	0.989	0.565
	e^-	+72.0	8.33	11.39	1.68×10^{29}	0.010	0.003
1994	e^-	-0.2	10.49	28.55	3.37×10^{29}	0.938	0.532
	e^+	+5.0	17.00	41.02	3.62×10^{29}	4.892	3.442
	e^+	+67.9	16.78	41.17	2.77×10^{29}	0.086	0.067
1995	e^+	-1.7	18.40	54.00	4.06×10^{29}	10.673	5.978
	e^+	+70.1	17.91	57.50	2.85×10^{29}	0.260	0.153
	e^+	-72.7	17.84	49.44	2.45×10^{29}	0.122	0.064
1996	e^+	-1.5	20.60	60.26	4.05×10^{29}	14.366	8.919
1997	e^+	-2.1	28.18	73.51	4.82×10^{29}	34.084	27.345

Table 1.1: *A Summary of H1 operations from 1992 to 1997. The lepton ring of HERA can be filled with either electrons or positrons. To improve the kinematic range of the experiment the interaction vertex can be moved away from the nominal position;* $\langle z \rangle$ *is the mean shift from the nominal position, a positive shift means the interaction point was shifted in the proton beam direction. The average lepton (*$\langle I_e \rangle$*) and proton (*$\langle I_p \rangle$*) beam currents are given for each year, along with the specific luminosity (*$\langle L_{sp} \rangle$*), the integrated luminosity produced by HERA (*$\int L_{\mathrm{HERA}}$*) and the integrated luminosity recorded on tape by H1 (*$\int L_{\mathrm{H1}}$*).*

the pipe–lines is read out. The time between the initial interaction and the final level 1 trigger decision is 2.5 μs (24 bunch crossings); the decision introduces no dead time. Dead time is produced by further event reconstruction after the event has been accepted. The level 2 trigger then analyses the event, taking, on average, a further 20 μs. The level 2 sub–trigger also examines the event topology, the events which survive this are passed to the Central Data Acquisition (CDAQ) system for a level 4 decision to be made. If the events fail then the detector is re–enabled. The trigger rates and the dead time at each trigger level can be seen in Figure 1.9.

The "event builder" combines the data from each subdetector after the information has been read out by the CDAQ. The full event is passed onto the level 4 trigger. By this time the size of the events has been reduced from about 3 Mbytes to 100 Kbytes by online data compression. The level 4 trigger uses a simplified version of the full event reconstruction routines to examine the event topologies in order to discriminate between the different classes of events and to find a vertex position for background rejection. Accepted events are written to tape and fully reconstructed. The time between the initial level 1 keep signal and when all the data are available to the level 4 trigger is approximately 1 ms.

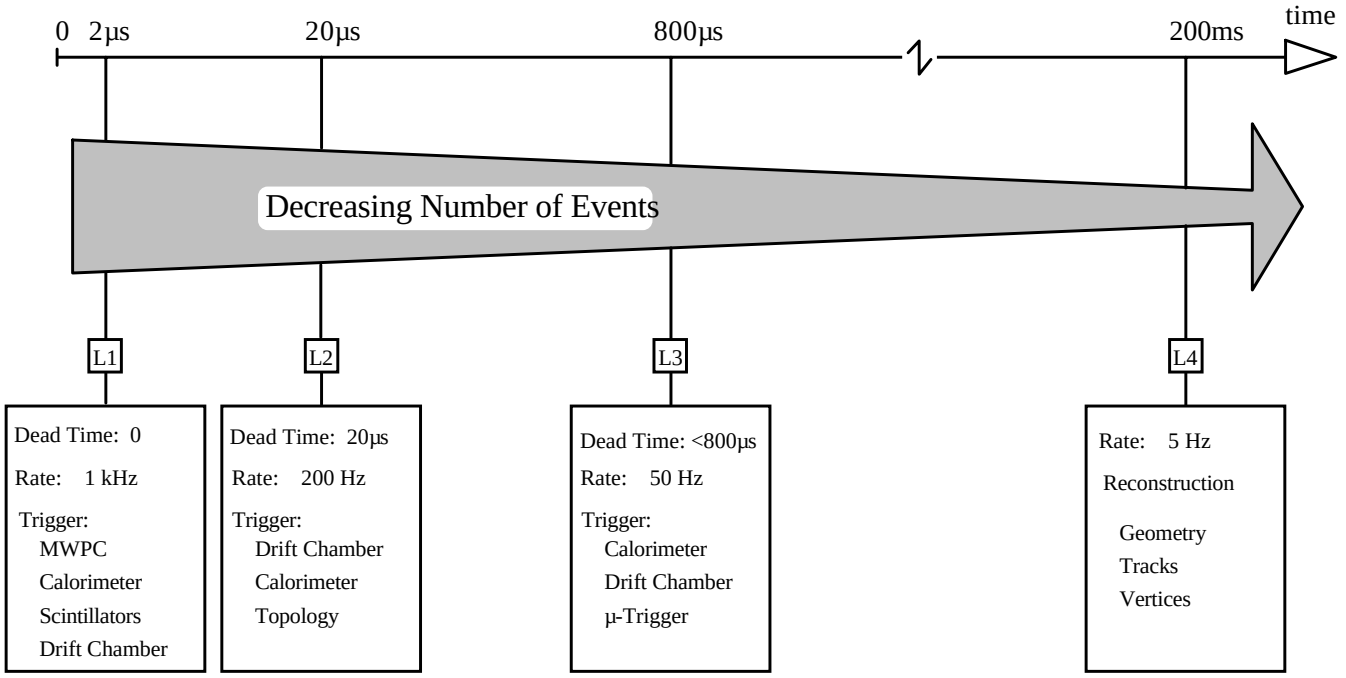

Figure 1.9: *The H1 Trigger System.*

Chapter 2

HERA Physics

The HERA ep collider at DESY has accessed a new kinematic region of lepton–nucleon scattering. When compared to older fixed target experiments, the phase space in Q^2 has increased by two orders of magnitude and at low Q^2 has lowered the detectable values of x by two orders of magnitude.

This section will describe briefly the physics processes occurring at HERA and define some of the kinematic variables that are used in this thesis.

2.1 Deep Inelastic Scattering

Deep Inelastic Scattering, DIS, occurs when a high virtuality boson interacts directly, electroweakly, with a parton inside the proton, $ep \to lX$. The struck parton and the proton remnant will then fragment, producing jets. A Feynman diagram of the neutral current process is shown in Fig. 2.1 and how the event appears in the H1 detector can be seen in Fig. 2.2. In the neutral current interaction a photon (or a Z^0) is the mediator and the outgoing lepton is unchanged. In the charged current interaction the mediator is a $W^{\pm}$ and the outgoing lepton is an electron–neutrino.

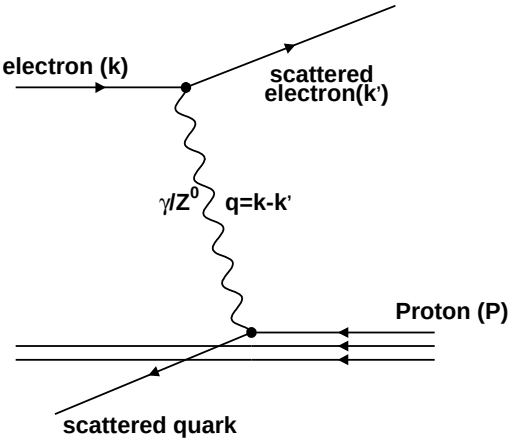

Figure 2.1: *Deep Inelastic Scattering*

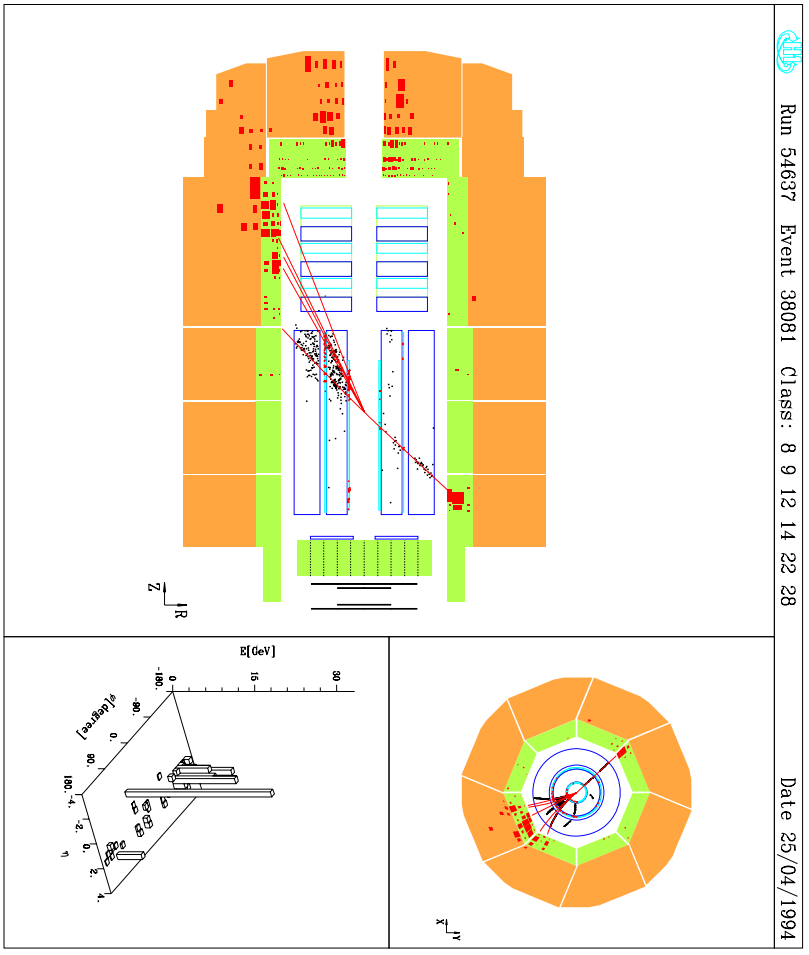

Figure 2.2: *A Typical Deep Inelastic Scattering event in the H1 detector.*

2.1.1 Kinematics

The kinematics of DIS processes are determined by two independent variables, usually chosen from Q^2, x (Bjorken x), W or y. Q^2 is the negative four–momentum transfer squared between the incoming and outgoing lepton. In the naïve quark parton model and in the infinite momentum frame, x is the fraction of the proton's momentum carried by the parton and, in the rest frame of the proton, y is the fractional energy loss of the scattered lepton. From Fig. 2.1 and using Lorentz invariant notation the kinematic variables are defined as:

$$Q^2 = -q^2 = -(k - k')^2 \tag{2.1}$$

$$x = \frac{Q^2}{2P.q} \tag{2.2}$$

$$y = \frac{P.q}{P.k} \tag{2.3}$$

where k is the four–momentum of the incoming electron, k' is the four–momentum of the outgoing lepton, P is the four–momentum of the incoming proton and q is the four–momentum of the exchanged boson. Neglecting the mass of the proton, the centre of mass energy squared, s, is given by:

$$s = (k + P)^2 \approx 4E_pE_e \tag{2.4}$$

where E_p is the proton beam energy and E_e is the electron beam energy. The mass squared of the hadronic system is:

$$W^2 = (P + q)^2 \approx Q^2 \left(\frac{1 - x}{x}\right) \tag{2.5}$$

With the current HERA beam energies a maximum s of 90200 GeV^2 can be achieved. Using

$$Q^2 = sxy \tag{2.6}$$

and assuming the deep inelastic regime ($Q^2 > 1$ GeV^2), it can be seen that x values as small as 10^{-4} can be accessed. The kinematic variables are often calculated using the "electron only" method. This uses the polar angle θ_e and the energy E'_e of the scattered electron with the following equations

$$Q^2 = 4E_e E'_e \cos^2 \frac{\theta_e}{2} \tag{2.7}$$

$$y = 1 - \frac{E'_e}{E_e} \sin^2 \frac{\theta_e}{2} \tag{2.8}$$

and equation 2.6 to calculate the kinematic variables.

The differential cross section for DIS at HERA is usually written in terms of the kinematic variables and probability functions known as structure functions. The Neutral Current cross section is:

$$\frac{d\sigma^{NC}}{dxdy} = \frac{4\pi\alpha_e^2}{sx^2y^2} \left[\left(1 - y + \frac{y^2}{2}\right) F_2(x,Q^2) - \frac{y^2}{2} F_L(x,Q^2) \pm \left(y - \frac{y^2}{2}\right) xF_3(x,Q^2) \right] \tag{2.9}$$

where the positive (negative) sign is for electron (positron) scattering and F_L, F_1, F_2 and F_3 are structure functions related by:

$$F_L(x,Q^2) = F_2(x,Q^2) - 2xF_1(x,Q^2) \tag{2.10}$$

and the Charged Current cross section for DIS is:

$$\frac{d\sigma^{CC}}{dxdy} = \frac{G_F^2.s}{2\pi \left(1 + \frac{Q^2}{M_W^2}\right)^2} \left[\left(1 - y + \frac{y^2}{2}\right) F_2(x,Q^2) - \frac{y^2}{2} F_L(x,Q^2) \pm \left(\frac{y^2}{2} - y\right) xF_3(x,Q^2) \right] \tag{2.11}$$

The structure functions F_1, F_2 are related to the magnetic dipole moment and electromagnetic charge distributions of the proton respectively and F_3 measures the contributions from Z^0 (neutral currect) and $W^{\pm}$ (charged current) exchange. The structure functions are measured at HERA in a previously inaccessible kinematic region as well as in the fixed target region.

2.2 Transverse Energy Flow

Parton densities are conventionally evolved in Q^2 by DGLAP equations [5]. At low x ($x < 10^{-2}$), the structure function $F_2(x, Q^2)$ rises sharply with decreasing x [6, 7]. In this low x region the DGLAP equations may not be applicable as they discard the sizable contribution from $\ln(1/x)$ terms. BFKL evolution equations [8] do contain the $\ln(1/x)$ terms.

A more sensitive method of determining whether the BFKL or the DGLAP evolution equations better describe the low x regime at the lowest order of expansion is by examining the transverse energy flow (E_T). The dominant process at low Bjorken x is a virtual boson–gluon fusion process with contributions from a gluon "ladder". This can be seen in Fig. 2.3. In the DGLAP picture, the parton cascade is evolved in Q^2 this leads to a strong ordering in transverse momentum, $k^2_{Tn} >> k^2_{Tn-1} >> ...k^2_{T1}$, while the longitudinal parton momentum scaled by the proton momentum is only softly ordered, $x_n < x_{n-1} < ... < x_1$. In the BFKL scheme the parton cascade has a strong ordering in the fractional momentum, $x_n << x_{n-1} << ... << x_1$, but there is no ordering in transverse momentum, which follows a random walk. Therefore the BFKL evolution is expected to produce more transverse energy from gluon radiation than in the DGLAP evolution at low Bjorken x.

2.3 Photoproduction

The dominant ep cross–sections at HERA are photoproduction processes [9]. The electrons scatter through only small angles and emit quasi–real photons (low Q^2), which then go on to interact with the proton. Photoproduction can be split into three categories:

- Vector Dominance Model (VDM) processes. In the VDM the photon fluctuates into a low mass vector meson which then interacts with the proton.
- Direct processes. The photon interacts directly with a quark or gluon from the proton.
- Resolved processes. A quark or gluon from the photon interacts with a parton from the proton. This results in a jet, the photon remnant, travelling roughly in the direction of the incident photon as well as jet(s) from the interaction with the proton (see Fig. 2.4).

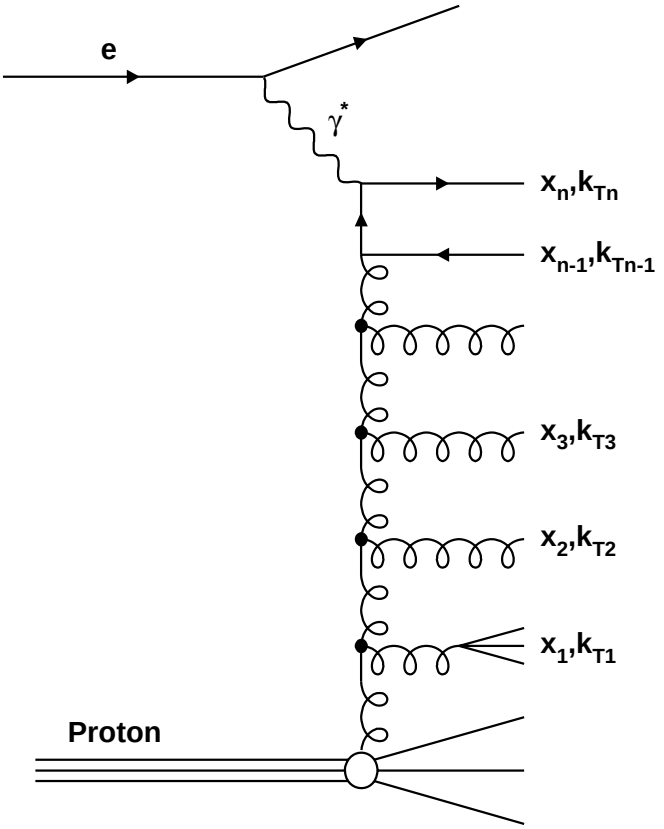

Figure 2.3: *Schematic Feynman diagram for ep DIS at low Bjorken x.*

Due to the large cross–section of photoproduction events and the similarity between photoproduction and DIS events the former process constitutes a major source of background to the latter one. Resolved photoproduction processes in which the photon exhibits hadronic behaviour can be described by photon structure functions F^{γ}.

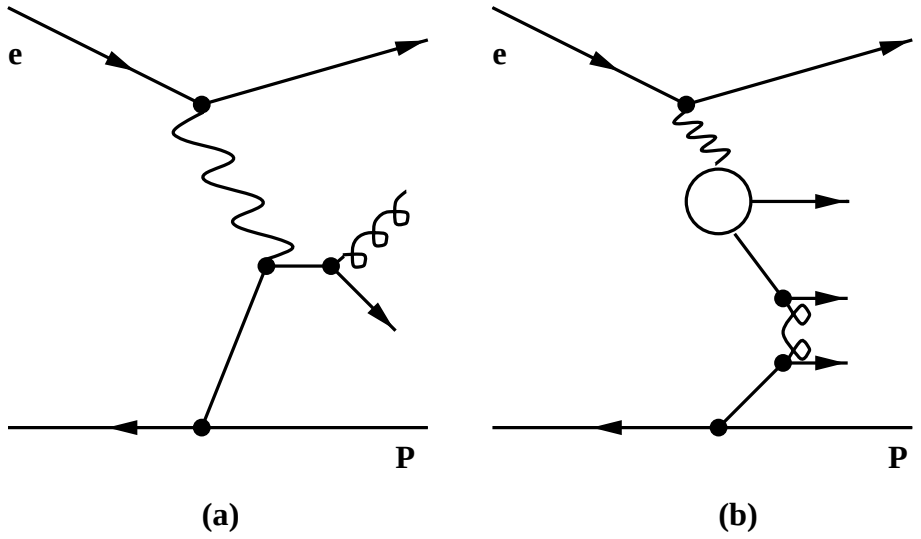

Figure 2.4: *Examples of hard photoproduction (γp) processes (a) direct (Compton–QCD) and (b) resolved photon processes.*

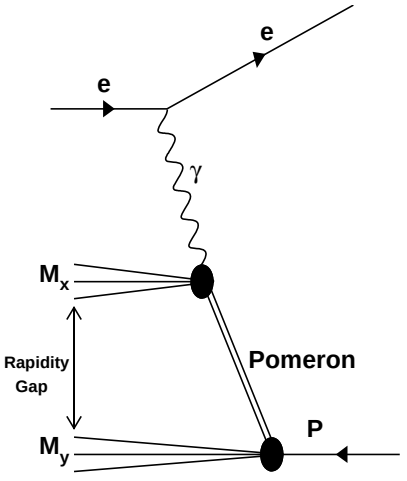

Figure 2.5: *Diagram for a deep inelastic event where the virtual photon scatters from a colourless object (pomeron) inside the proton.*

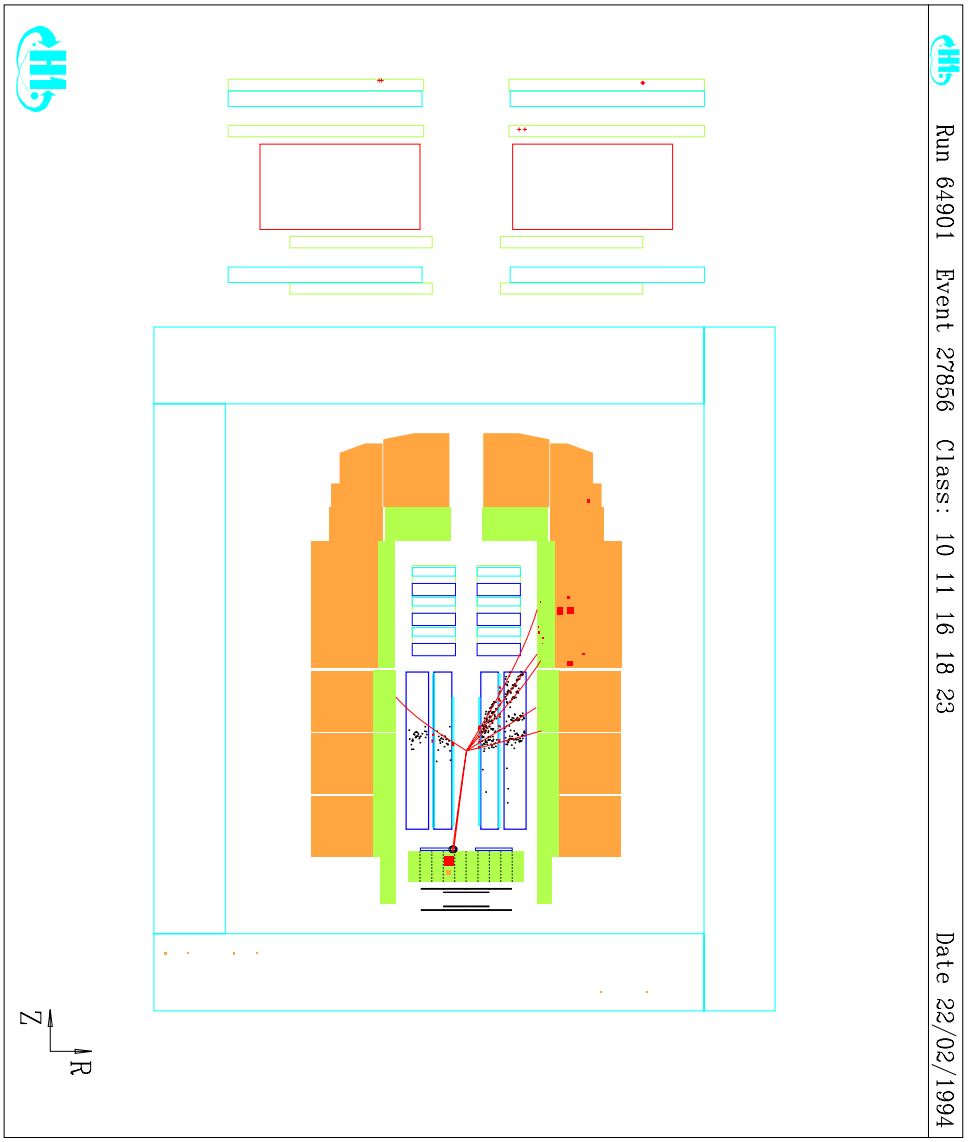

Figure 2.6: *A Typical Diffractive (Rapidity Gap) event in the H1 detector.*

2.4 Large Rapidity Gap Events

Typically DIS events have energy flow in the proton direction. This flow can be interpreted as the fragmentation of the proton remnant or alternatively as soft radiation from the exchanged object. However, both H1 [10] and ZEUS [11] have a class of events, approximately 6% of the DIS sample, where this energy flow is not present. These large rapidity gap (so called due to the large area of rapidity space devoid of energy) or diffractive events are thought to be produced by a colourless exchange between the proton and the mediating boson. The colourless exchange particle is usually referred to as the 'pomeron'. A diagram of the lowest order diffractive process is shown in Fig. 2.5 and how a rapidity gap event appears in the H1 detector is shown in Fig. 2.6.

2.5 Exotics

As with any other particle physics experiment, H1 conducts searches for new particles outside the Standard Model. The HERA experiments particularly concentrate these searches on excited leptons, leptoquarks and contact interactions. Leptoquarks are bound states of quarks and leptons, and contact interactions result from quark or lepton sub–structure.

Recent results from HERA report that both H1 [12] and ZEUS [13] have witnessed an excess of events at very high Q^2 ($Q^2 > 15000$ GeV^2). The possibility of a statistical fluctuation is low. However, other possible explanations involving leptoquark production or contact interactions also do not appear to be likely.

Chapter 3

QCD Models

3.1 QCD

Quantum Chromodynamics (QCD) is the theory of the strong interaction between coloured objects (quarks and gluons). Quarks were discovered in the 1960s when DIS experiments provided the first evidence that nucleons are composed of pointlike particles. A quark has never been observed in isolation. This result is known as quark confinement and is due the fact that although the strong force is small in magnitude at short distances ($<< 10^{-15}$m) it increases quickly and indefinitely as the distance between the coloured objects grows. The "charge" of the strong gauge group is "colour" which can take one of three values (or their anti–values) usually called red, green or blue. The gauge bosons of the theory, the gluons, are also coloured and therefore can self couple. It is this property that causes the strong force to grow at large distances. Gluons are created from the vacuum around a bare coloured object and produce an anti–screening effect which increases the strength of the colour field around the object as the distance from the coloured object grows.

The vacuum polarisation contribution to quark–quark scattering causes the effective coupling constant of QCD, α_s, to decrease as the energy scale of a process, Q^2, increases (known as asymptotic freedom). In the leading logarithmic approximation the coupling constant is written as:

$$\alpha_s(Q^2) = \frac{12\pi}{(33 - 2N_f)\ln(Q^2/\Lambda^2_{\overline{MS}})} \tag{3.1}$$

where N_f is the number of quark flavours and $\Lambda_{\overline{MS}}$ is a scale constant that must be

determined by experiment. Perturbative QCD breaks down when α_s becomes too large and the scale at which this occurs is characterised by $\Lambda_{\overline{MS}}$.

3.2 Quark Parton Model

In the Quark Parton Model (QPM) QCD radiation is ignored so the QPM can be thought of as being 0^{th} order in QCD. In the QPM the proton is made up of three "valence" quarks together with many quark–antiquark pairs (predominately $u\bar{u}$, $d\bar{d}$ and $s\bar{s}$), called "sea" quarks. In this model DIS is viewed as the scattering of the electron off of a parton carrying a fraction, x, of the proton's momentum.

Evidence that nucleons were composed of partons was produced in SLAC in the 1960s. When the proton is probed with a sufficiently high Q^2 photon its constituents can be resolved. The proton structure function $F_2(x, Q^2)$ appeared to be independent of Q^2 at a given x value [14, 15]. This phenomenon is known as Bjorken scaling and is evidence for the existence of partons.

If weak interactions are neglected ($F_3 \to 0$) the cross-section for DIS given by the QPM can be written in terms of two dimensionless structure functions $F_1(x, Q^2)$ and $F_2(x, Q^2)$:

$$\frac{d^2\sigma}{dQ^2dx} = \frac{4\pi\alpha^2}{xQ^4}\Big((1-y)F_2(x,Q^2) + xy^2F_1(x,Q^2)\Big) \tag{3.2}$$

The structure functions can be related by the Callan and Gross relation:

$$2xF_1(x) = F_2(x) \tag{3.3}$$

if the charged constituents of the proton are spin $\frac{1}{2}$ particles.

The structure function F_2 gives a measure of how the proton's momentum is distributed amongst its constituent charged partons. F_2 can be expressed as:

$$F_2(x) = \sum_i e_i^2 x f_i(x) \tag{3.4}$$

where $f_i(x)$ is the probability that the parton i with charge e_i carries a fraction x of the

proton's momentum.

By comparing F_2 measured in neutrino–nucleon scattering with that measured in electron scattering it was confirmed that $F_2^{\nu N} \simeq \frac{18}{5} F_2^{eN}$, as expected for quarks with fractional charge.

3.3 Leading Order Processes

Matrix elements can be calculated to a given order in α_s, thus producing a description of parton emissions. All the Monte Carlo generators used in this analysis incorporate first order (leading order) calculations, although Monte Carlos such as Cyclops, exist with next to leading order calculations. Leading order effects include the radiation of a gluon by the quark, before or after the interaction with the virtual photon, corresponding to initial state and final state Compton QCD (CQCD) processes respectively (see Fig. 3.1). Another leading order process is the interaction of a gluon from within the proton and the virtual boson by the production of a $q\overline{q}$ pair, known as Boson–Gluon Fusion (BGF), see Fig. 3.2.

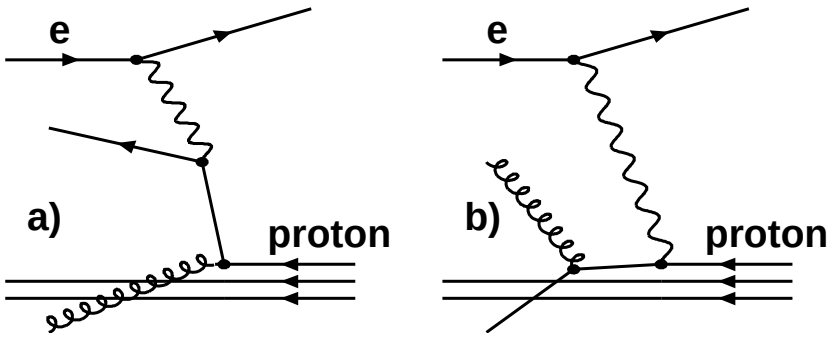

Figure 3.1: *Feynman diagrams for (a) initial state Compton QCD and (b) final state Compton QCD.*

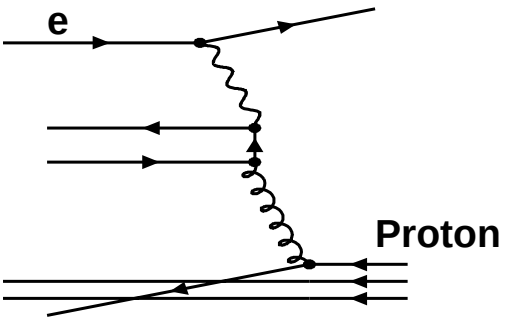

Figure 3.2: *A Feynman diagram for a Boson–Gluon Fusion event.*

3.4 Parton Showers

In the previous section it was mentioned that some higher order matrix elements are calculable but the calculation of matrix elements above leading order is extremely difficult. As an alternative a scheme using parton showers (both initial and final state) can be adopted.

The parton shower scheme allows for the incoherent splitting of the parent parton into two daughters; the possible transitions are $q \to qg$, $g \to q\overline{q}$ and $q \to gg$. The probability of each splitting is defined in terms of z, the energy fraction taken from the parent parton by the daughter. For final state showers, analytical techniques using Sudakov form factors select the mass and energy of the parent parton produced in the hard sub–process. The mass squared of the parton must be positive so final state parton showers are often referred to as time–like showers. The showering is ordered by the use of the parton mass as a virtuality scale and daughters go on to become parents until a virtuality cut off is reached. The initial state showers work in reverse as the highly virtual partons entering the hard sub–process are known and the parent partons have to be derived. Initial state parton showers can be referred to as space–like as the mass squared of the partons is negative.

In the leading order approximation the probability of a branching $a \to bc$ to occur

during a small change $dt = dQ^2_{\rm evol}/Q^2_{\rm evol}$ of the evolution parameter $t = \ln(Q^2_{\rm evol}/\Lambda^2)$ is given by the Altarelli–Parisi equations [16]:

$$\frac{d\mathcal{P}_{a\to bc}}{dt} = \int dz \frac{\alpha_s(Q^2)}{2\pi} \mathcal{P}_{a\to bc}(z) \tag{3.5}$$

where $\mathcal{P}_{a\to bc}(z)$ are the Altarelli–Parisi splitting kernels which describe the probability that a parton of four–momentum zp will be produced from a parton of initial momentum p. The splitting functions are:

$$\mathcal{P}_{qq(z)} = \frac{4}{3}\left[\frac{1+z^2}{1-z}\right] \tag{3.6}$$

$$\mathcal{P}_{qg(z)} = \frac{1}{2}[z^2 + (1-z)^2] \tag{3.7}$$

$$\mathcal{P}_{gq(z)} = \frac{4}{3}\left[\frac{1+(1-z)^2}{z}\right] \tag{3.8}$$

$$\mathcal{P}_{gg(z)} = 6\left[\frac{(1-z)}{z} + z(1-z) + \frac{z}{(1-z)}\right] \tag{3.9}$$

and the corresponding diagrams are shown in Fig. 3.3.

3.5 The Colour Dipole Model

The Colour Dipole Model (CDM) [17] is implemented in the Ariadne Monte Carlo [18] and gives a good description of data produced in both e^+e^- [19] and lepto–production [20] experiments. In the CDM most QCD radiation of quarks and gluons is described in terms of radiation from colour dipoles between partons rather than treating each parton as an independent emitter.

The CDM works by assuming that a gluon emitted by a $q\overline{q}$ pair can be thought of as radiation coming from the colour dipole between the q and the $\overline{q}$. The emission of a second, softer, gluon can then be looked upon as radiation from two independent dipoles, one between the q and the original gluon and the other between the $\overline{q}$ and the gluon. This

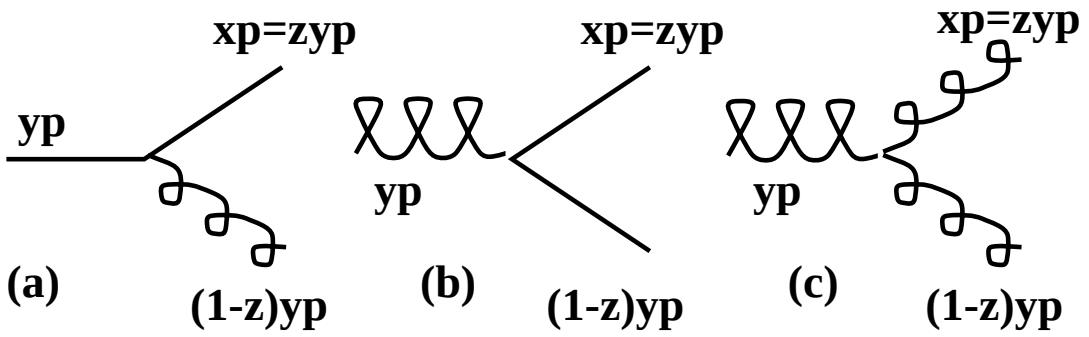

Figure 3.3: *The partonic processes described by the Altarelli–Parisi splitting kernels (a) $\mathcal{P}_{qq(z)}$, (b) $\mathcal{P}_{gq(z)}$, (c) $\mathcal{P}_{gg(z)}$.*

process can be extended for a third gluon and so on. For gluon emission there are three colour dipoles – one for $q\overline{q}$ pairs, one for qg (or $\overline{q}g$ pairs) and one for gg dipoles. The cross section for each dipole can be calculated using the appropriate Feynman diagram.

The gluons emitted by the colour dipoles do not obey strong angular ordering. In this sense the CDM representation is similar to the BFKL evolution.

3.5.1 The CDM in Deep Inelastic Scattering

The CDM when applied to Deep Inelastic Scattering does not distinguish initial and final state QCD radiation as conventional parton cascades do. Instead, it assumes that all radiation can be described by the colour dipole between the struck quark and the proton remnant. The situation is therefore very similar to the e^+e^- case with one small difference. In e^+e^- both the q and the $\overline{q}$ can be thought of as point–like, but for DIS only the struck quark is point like, the proton remnant must be considered as an extended object. The radiation of small wavelengths from an extended object is suppressed. This is taken into account by the CDM and results in a phase space reduction which leads to the suppression of radiation in the target region when compared to the e^+e^- case.

The CDM does not describe BGF events. As the CDM only considers the radiation

between the struck quark and the proton remnant, it does not account for the incoming gluon splitting into a quark–antiquark pair. To overcome the problem a first order matrix element is used to generate the BGF process and further emission is performed by dipole radiation.

3.6 Fragmentation

Fragmentation is considered as a two stage process described by the breakdown of the perturbative approach in the limit $Q \sim \Lambda_{\overline{MS}} \sim 100 - 400$ MeV. The two stages are: the perturbative phase of gluon emission and the non–perturbative hadronisation stage. Hadronisation describes the process of transforming the final state partons into a jet of hadrons. Phenomenological methods are used to model the low energy behaviour.

3.6.1 Local Parton–Hadron Duality

Local Parton–Hadron Duality (LPHD) [22] is the simplest assumption for hadronisation but it is not implemented in any Monte Carlo. LPHD assumes that the general features (e.g. energy flow etc.) of the partonic final state can be related to the hadronic spectra by the introduction of overall normalisation constants. These constants are determined by experiment. This approach has the advantage that the results of analytical calculations can be compared directly to the measured distributions of the hadrons even at low energy scales without using any further hadronisation model.

3.6.2 Independent Fragmentation

Feynman and Field first proposed the Independent Fragmentation Model [23]. The model is based around the two ends of a colour string fragmenting independently. Both energy and momentum are not conserved simultaneously by the model and it does not reproduce particle densities, for these reasons it is not used very often.

3.6.3 String Fragmentation

The confinement picture, where the energy stored in the colour field between a quark and an anti–quark increases as the separation between them grows, is supported by lattice QCD studies. If the simplest case is examined, and gluons are ignored, the struck quark is knocked out of the proton and in doing so a string is formed between the quark and the proton. As the quark and proton separate the potential energy between them increases to the point where a quark–antiquark pair can tunnel out of the vacuum, or to look at it another way the string breaks into two less energetic strings (see Fig. 3.4). Further breaking can then occur. In the Lund string model this string breaking continues until only on mass shell hadrons remain.

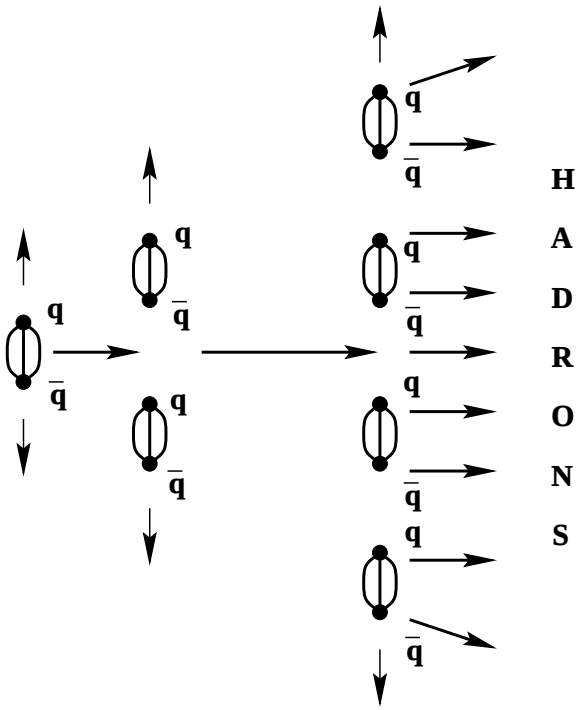

Figure 3.4: *A graphical representation of the string fragmentation model. The string between a $q\overline{q}$ pair breaks creating more strings of lower energy, this process continues until the final state hadrons are created.*

3.6.4 Cluster Fragmentation

The HERWIG [24] Monte Carlo operates by modelling the formation and decay of colourless clusters. The partons are generated perturbatively and then all final state gluons are divided non–perturbatively into light (up or down) quark and anti–quark pairs. Coloured objects that are close to one another are combined into colourless objects which then decay according to known branching ratios and available phase space.

3.7 Soft Colour Interactions

Soft colour interactions (SCI) were originally conceived as a model for explaining rapidity gap events [25]. This idea did not prove to be particularly successful but final state soft colour interactions must occur at some level. At low x most events are of a boson–gluon fusion type so if the string model is used, two fragmenting strings would span the BGF diagram, see Fig. 3.5a. While the quark–antiquark pair leave the proton, soft gluons can be exchanged between them and the proton remnant; in this case there will be more particles and energy per unit rapidity, see Fig 3.5b. These gluons do not greatly affect the momentum of the $q\overline{q}$ pair but can change their colour configuration, perhaps even producing a colour singlet so that the $q\overline{q}$ pair is no longer connected to the proton (Fig 3.5c), producing rapidity gaps.

3.8 Monte Carlo Generators

The "workhorse" Monte Carlo used in this analysis is based on the Ariadne Monte Carlo [18]. Ariadne is a member of the Lund family of Monte Carlos and is used to generate the QCD cascade process. To generate a whole event Ariadne must be interfaced with other programs. The LEPTO Monte Carlo [25] uses leading order QED matrix elements to generate the electro–weak scattering process; JETSET [21] is used to perform the hadronisation and particle decays and Django is used to model the radiative effects. This combination is referred to as the MEAR (Matrix Element + ARiadne) Monte Carlo, where ME refers to the QCD Matrix Element used to generate the BGF events. For comparison and to assess systematic errors a second Monte Carlo is used. This Monte Carlo again uses matrix elements but soft emissions are described by Leading—Log DGLAP parton showers therefore the Monte Carlo is known as MEPS (Matrix Element + Parton

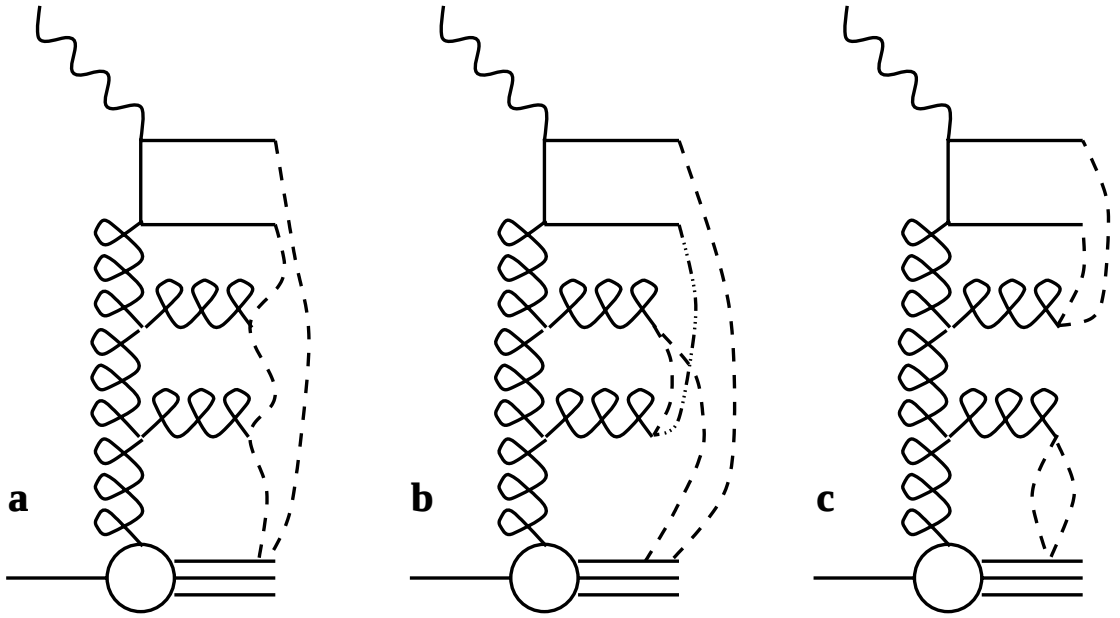

Figure 3.5: *The string configurations (dashed and dotted lines) for the usual scenario (a) and after soft colour interactions, producing (b) longer strings or (c) a rapidity gap.*

Shower). With MEPS it is possible to implement soft colour interactions during the formation of the hadronic final state, so comparisons can be made both with and without SCI.

Chapter 4

Cone Algorithm

4.1 Introduction

This chapter is based on the author's publication [26] and is not connected to the H1 analysis. In particle physics experiments, partonic substructure manifests itself, dynamically, in the form of collimated showers or 'jets' of hadrons. In order to get further information on the direction or energy of such partons it is necessary to adopt standard definitions of such jets, and then test these against simulations of the fragmentation process thus obtaining factors with which to 'correct' data. Having found the axis of a jet the precise details (shape) of the energy deposition around it are often used to discover further details of, for example, the nature (gluon or quark) of the jet [27], to ascertain the importance of final state multiple interactions [39, 40], or other kinematic details [28]. This chapter concentrates on the sensitivities of such studies of jet profiles, the jet topology of events and inclusive transverse energy spectra. Algorithmic reliability for reconstruction of parton four-momenta is a different subject and is not considered within this analysis.

Jet finding algorithms can be split into two generic categories using respectively geometric or dynamic quantities [29]. Geometric algorithms define jets purely as *areas* of localised energy deposit, whereas dynamic algorithms (eg the 'JADE' [30] or 'Durham' [31] algorithms) use kinematic rather than angular information. Most of the studies of jet-profiles in the literature [32, 33] have used geometric or 'cone' algorithms and this section investigates the biases of such algorithms on the resulting properties of jets and jet–profiles. A detailed description of such cone algorithms can be found in [33, 34].

For this analysis a simple Monte–Carlo program was written which simulates random

(isotropic) hadronic hits in a typical, fine–grained, calorimeter system. A jet–finding algorithm using a search–cone technique finds jets and the corresponding energy profiles are constructed. These profiles, jet transverse (E_T) spectra, and other properties are then compared with those obtained in real data. In particular it will be shown how results of search–cone jet finding algorithms are severely (software) trigger biased [33, 35].

This analysis is radically different from previous work [36] in which search cone algorithms have been used to compare specific input energy distributions with the profiles seen in data. Here the distribution of hits in the calorimeter is purely isotropic. Any structure in the resulting profiles is thus entirely the result of algorithmic selection of statistical fluctuations.

4.2 The Monte–Carlo Program

A simple Monte–Carlo program has been written to represent events observed in a generic calorimeter system. This program contains essentially no physics. There is not even consideration of conservation of momentum.

Most cone algorithms work in the space of pseudo-rapidity ($\eta = -\ln(\tan\theta/2)$) and azimuthal angle ($\phi$), since *differences* in such variables are invariant to Lorentz boosts along the $z-$axis of the interacting particles in photoproduction and hadron–hadron collisions. Additionally, for large parts of the central plateau, inclusive measurements and scaling theory [37] predict isotropic distributions in these variables and since $\eta \to \infty$ for the spectator system there is good separation of jets from such target remnants.

The model calorimeter is divided into $30(\phi) \times 25(\eta)$ cells, in the form of a grid made to wrap in the ϕ-direction and arbitrarily covering the region $-1 \leq \eta \leq 3.3$ to aid comparison with existing data. The energy was distributed in the grid by randomly placing a number of 'hits' (with fixed value n=30) in this grid. The transverse energy of each separate hit, E_t, is determined randomly according to an exponentially decreasing distribution, ie. the probability is $P(E_t)dE_t = \lambda e^{-E_t/\lambda}dE_t$. The average E_t, $< E_t >= \lambda$, is set as 1 GeV by default. When two (or more) hits occur in the same cell the energies of the hits are summed and their centre of energy position calculated. This distribution of hits constitutes an event.

Therefore, the Monte–Carlo program has only two, independent, variables, the average

energy of a hit, λ, and the multiplicity of such hits, n. Effects due to the variation of these parameters will be covered in later sections.

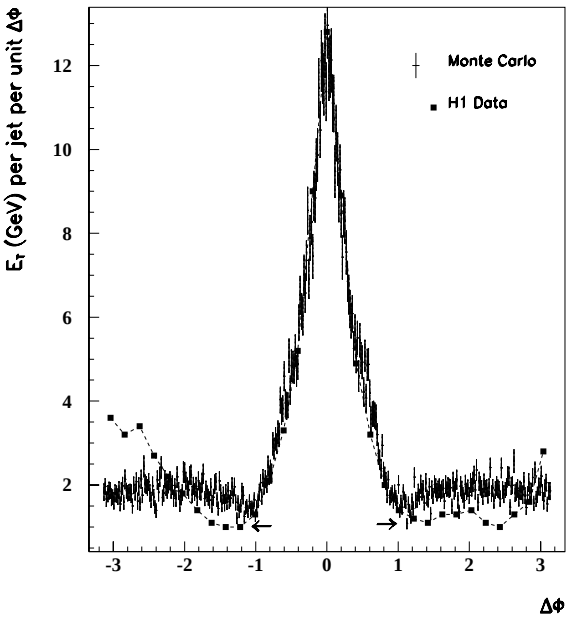

Figure 4.1: *The comparison of the "toy" Monte–Carlo energy profile results (fine lines) with real H1 data (solid squares). The toy Monte Carlo has a fixed multiplicity of 30 and an average energy of 1 GeV. The cone threshold is set at 9 GeV. See text for discussion of arrowed areas of data.*

4.3 The Jet Finding Algorithm

The Jet Finding algorithm used a search cone centred on particular high energy hits and is almost identical to the LUCELL algorithm of JETSET [21] which in turn is utilised by the analysis code of many particle physics experiments. The program arranges all hits or potential 'initiators' within one event in order of decreasing transverse energy. Starting with the highest energy initiator, the transverse energies of all hits within the search cone area are summed and, if the total is above a given threshold value, E_T', a jet has been found. The centre of energy of the jet is then calculated and energy weighted profiles are formed in both the ϕ and η projections with respect to this axis. For a ϕ–profile (Fig. 4.1) all the hits within an interval of $\delta\eta = \pm 1$ of the jet axis are included. The algorithm ensures that hits within a given jet do not contribute to another jet. If a jet is

not detected, the algorithm creates a new search cone centred on the next highest energy initiator, and this process may be iterated over all acceptable possibilities.

The algorithm contains several internal parameters which, as will be demonstrated, strongly determine the observed energy profiles. Apart from the most important value of E_T' there is a second threshold value (not to be confused with the *jet* threshold value) which determines acceptable initiators. Additionally, the radius and shape ($\Delta R = \sqrt{(\alpha\Delta\phi^2 + \beta\Delta\eta^2)}$ where Δ refers to the difference between the current axis and a given hit) of the search cone can also be altered. For the default circular search cone α and β are set equal to one. However, an elliptic cone can be produced with any other values thus enabling searches with cones of the same threshold and area, but of different *shape*, on the same sets of events.

4.4 Results

For Monte–Carlo values of the energy per hit in the region of 1 GeV, multiplicities in the neighbourhood of 30 and using appropriate threshold (9 GeV) and search–cone size values (ΔR=1), the energy profiles compare well with real data, as can be seen from Fig. 4.1 [39]. The net effect is of a sharp peak sitting on a plateau whose height scales with the multiplicity and average energy per hit. In data this is sometimes referred to as an 'underlying event' and has been interpreted as being due to multiple interactions of partons not involved in the hard scattering process [39, 33, 38].

The correlated recoil jet seen in photoproduction data is not reproduced in this simple simulation since conservation of transverse momentum is not included. Note a very important element of detail (arrows in Fig 4.1): in real data there is a small signal of excess energy just *outside* the search cone, which is never reproduced in these Monte–Carlo simulations.

From Fig. 4.2 it can be seen that the jets are produced by statistical fluctuations in both the multiplicity (a) and the average energy per hit (b) because *both* increase around the jet axis. Fig. 4.1 can be looked upon as the product of Fig. 4.2a and Fig. 4.2b.

In data [41], jet profiles have been described as having a 'hard' core ($|\Delta\phi| < 0.2$) and wings ($0.2 \leq |\Delta\phi| < 1.0$). The simple model already duplicates this effect and in this case it is due mainly to the initiator hit, close to the centre of the jet and moved only by the

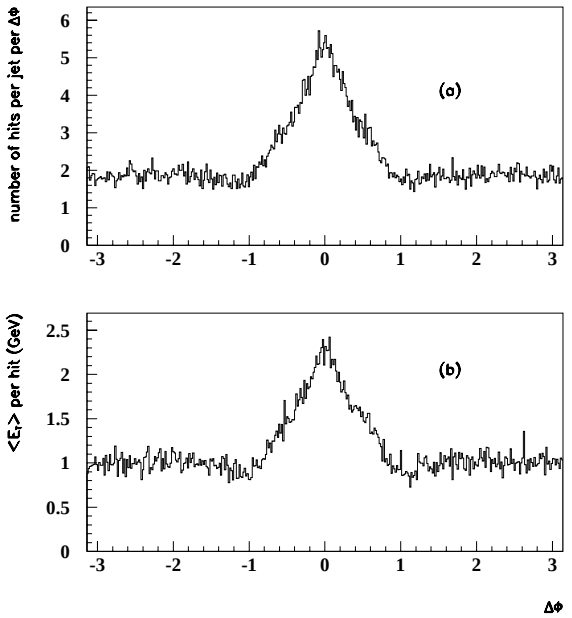

Figure 4.2: *(a) The number profile of hits per jet per unit $\Delta\phi$ and (b) the average transverse energy profile per hit. All the hits within an interval of $\delta\eta = \pm 1$ of the jet axis are included.*

weighting procedure that occurs when the jet axis is calculated. The jets produced at a low threshold or with high energy hits have a harder core because they are dominated by the initiator . The wings are therefore caused by the more numerous, smaller energy, hits needed to raise the jet energy above threshold. Jet profiles for events with high average hit energy tend to have small dips (Fig. 4.3c) in the background plateau, just outside of the cone radius. These dips appear to be very similar to the dips seen in low energy "mini" jets in [42].

4.4.1 Monte–Carlo Dependent Effects

Fig. 4.1 was produced using a fixed multiplicity of 30 and an average energy of 1 GeV per hit. Variation of either parameter has a significant effect on the shape of the jet profile.

In Fig. 4.3 it can be seen how the jet profiles produced depend on the average energy per hit (a) and (c) and the multiplicity (b) and (d). A higher average energy (Fig. 4.3c has an average energy of 2.0 GeV per hit) will produce taller, thinner jets as the jet is made up from a few, high energy, hits. The reverse is also true, as can be seen from

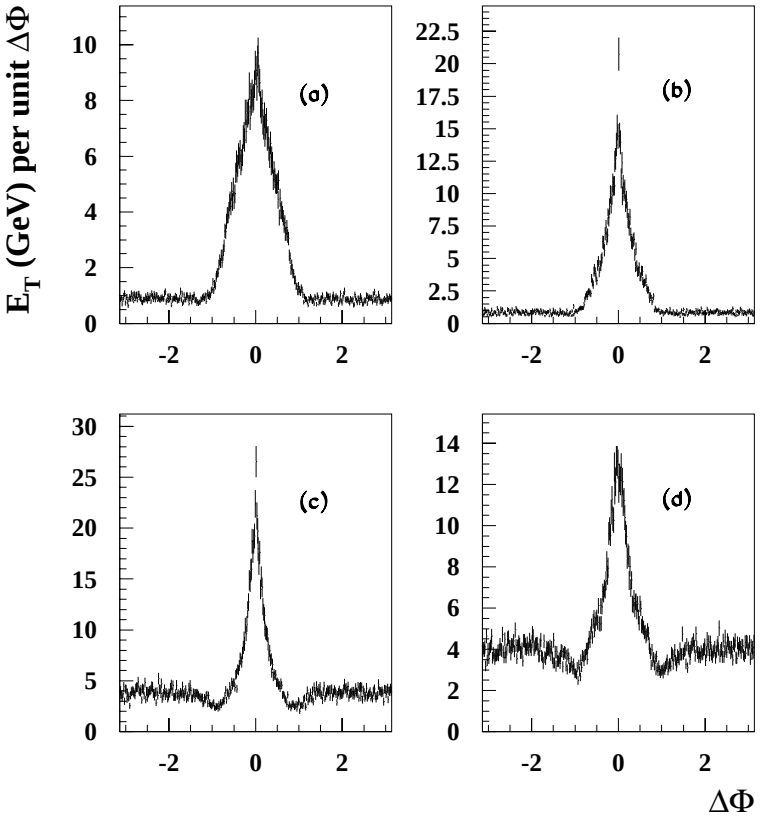

Figure 4.3: *Jet profiles obtained using ((a)* $< E_T >= 0.5\,GeV$ *and (c)* $< E_T >= 2.0\,GeV$*) increasing average energies per hit and ((b)*$n = 15$ *and (d)*$n = 60$*) increasing multiplicities, n. The jet algorithm parameters are held constant throughout.*

Fig. 4.3a which has hits of average energy 0.5 GeV. A disproportionately high centre bin sometimes occurs, caused by single, isolated, high energy initiator hits passing the threshold by themselves.

A low multiplicity (Fig. 4.3b utilises a multiplicity of 15) also results in taller, thinner jet profiles because the average spacing between hits is increased. This can also be seen in the lower level of the background plateau for this choice of parameter. Again the reverse is true. Fig. 4.3d is the result of a multiplicity of 60 and is wider with a higher background. In this plot it is also possible to distinguish between the effect of the central initiator and the other hits inside the cone which form the 'shoulders' of the profile.

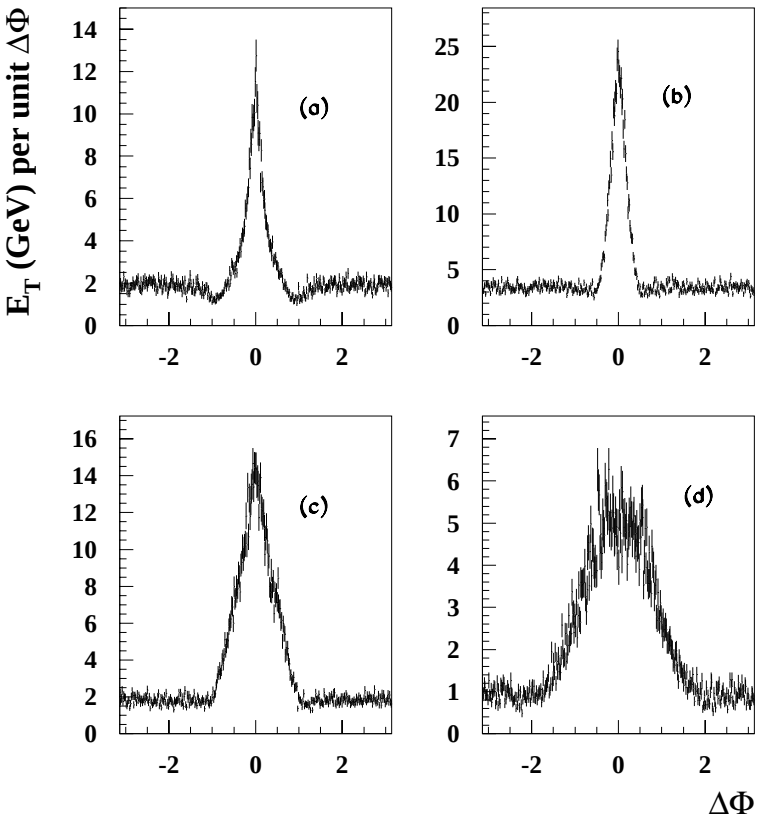

Figure 4.4: *Jet profiles obtained using ((a) E_T=5 GeV and (c) E_T=13 GeV) increasing thresholds and ((b) and (d)) wider ϕ dimensions of search cone. The toy Monte–Carlo parameters are held constant throughout.*

4.4.2 Algorithmic Effects

Changing the algorithm parameters can also affect the *shape* of the jet profiles. This can be seen in Fig. 4.4 where the toy Monte–Carlo parameters have been held constant at a multiplicity of 30 and an average energy per hit of 1 GeV. Here we alter two of the algorithmic parameters; the jet threshold value (a) and (c) and the shape (or radius) of the search cone (b) and (d).

A low threshold (Fig. 4.4a has a threshold of 5 GeV) is more easily achieved and so on average fewer hits are required to form a jet. The resulting profiles tend to be thinner and are dominated by events with a single initiator. Fig. 4.4c has a threshold of 13 GeV and shows that the reverse argument holds when many hits in a broad area are required to reach the threshold.

Changing the shape of the search cone results in very different jet profiles, even when the search algorithms are run over the same data. An elliptical search cone elongated in the η direction (Fig. 4.4b) with a width of only half a radian in the ϕ direction but with the same area as the cone in Fig. 4.1 produces a profile with the jet fully contained within that smaller area. A similarly elongated cone in the ϕ direction (Fig. 4.4d $\Delta\phi$=2 radians) is also contained in the same net area but with a completely different projection of the energy profile. Fig. 4.4b has a background level twice as high as Fig. 4.1. As an elliptical cone was used all the hits within an interval of $\delta\eta = \pm 2$ of the jet axis are included, so the background is twice as high. The reverse is true for Fig. 4.4d. Error bars are larger since the statistics are consequently lower.

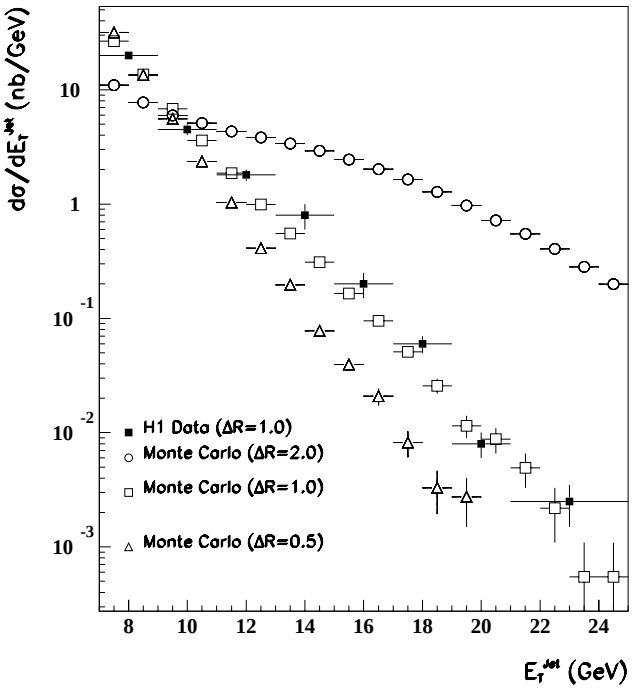

Figure 4.5: *The comparison of inclusive jet cross sections taken from H1 data (solid squares) with those taken from the toy Monte–Carlo ($\Delta R = 1$ open squares, $\Delta R = 2$ circles and $\Delta R = 0.5$ triangles). The simulation is normalised to have the same area as the data (see text).*

4.5 Jet Transverse Energy Spectrum

The jet transverse energy spectrum starts at the threshold value and falls exponentially, a reflection of the energy spectrum of the individual hits. Fig. 4.5 compares the inclusive differential jet cross section in *ep* photoproduction interactions [39] as a function of transverse energy with jet transverse energy spectra in this work. The Monte–Carlo energy spectra have been normalised to the observed data cross–section. Three different search cone radii were used ($\Delta R = 0.5$, 1.0 and 2.0) to examine how this affected the gradient.

When simulated events are searched with the same cone size as used for data ($\Delta R = 1$) the results using an average transverse energy of 1 GeV per hit and a multiplicity of 30 closely resemble real data but the results with different sizes are radically changed. Changing these Monte–Carlo parameters also affects the gradient. An increased average transverse energy per hit results in a flatter gradient as more jets of a higher energy are produced. The reverse argument also holds. Changing the multiplicity also has an effect, although it is less pronounced. An increased multiplicity again produces a flatter spectrum, whilst a low multiplicity results in a steeper slope.

4.6 Jet Rate

The number of jets produced per event (jet rate) as a function of the total visible energy in the event has a distinctive shape (see Fig. 4.6). As the event energy grows, the rate at which no jets are found falls steeply as $\geq$ 1–jet events are produced. The relative rate of these 1–jet events grows and then falls as the 2–jet events begin to take over. This process then happens again with the 2 and 3–jet events which will dominate given sufficient transverse energy.

Fig. 4.6 shows how the jet rate found in the simple Monte–Carlo compares with real data [39]. The only significant difference between the two can be explained by the conservation of transverse momentum. The Monte–Carlo jet rate for the 1–jet events is slightly higher than in data, and correspondingly lower for the 2–jet events. Momentum conservation will make it more likely for two (azimuthally back–to–back) jets to be produced. A crucial point is not only does the simple Monte Carlo produce jets that *look* like the data, but it also produces these jets at the same *rate* as in the data.

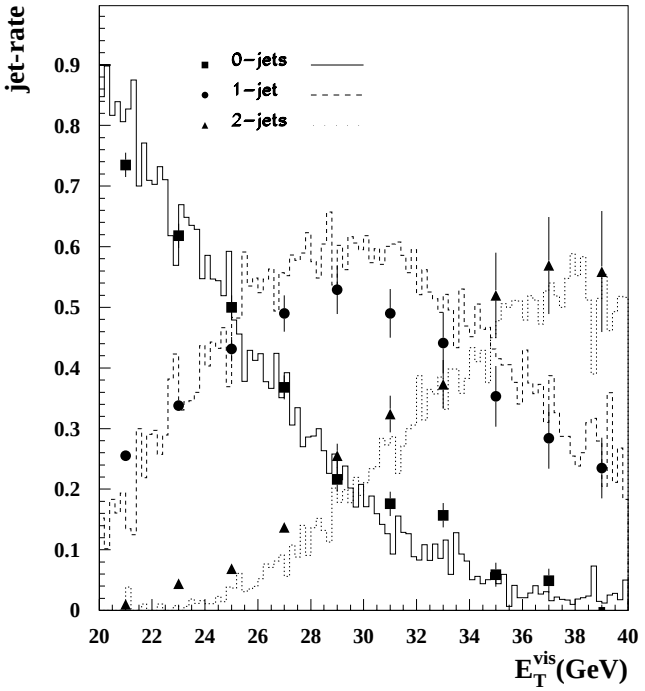

Figure 4.6: *The comparison of toy Monte–Carlo (lines) jet topologies with those in H1 data (points). In both cases, the threshold for defining a jet is set to 7 GeV, the search cone has a radius 1.0.*

4.7 Jet Widths

A previous work [39] noted that a simple Gaussian plus background shape does not fit the $\Delta\phi$ data as well as the following three parameter function:

$$f(\Delta\phi) = A\exp(-(\sqrt{\Delta\phi}+b)^4 + b^4) + P$$

The full width (Γ) at half maximum above the plateau P is :

$$\Gamma = 2((\ln 2 + b^4)^{1/4} - b)^2$$

This function was compared with the toy Monte Carlo jet profiles produced in this analysis and was found to give a significantly better fit than a simple Gaussian.

The fitted full width Γ at half maximum above the plateau is plotted against the scaled jet energy $2E_T^{jet}/\sqrt{s_{ep}}$ in Fig. 4.7. The data of [39] is reproduced in Fig. 4.7 and the line

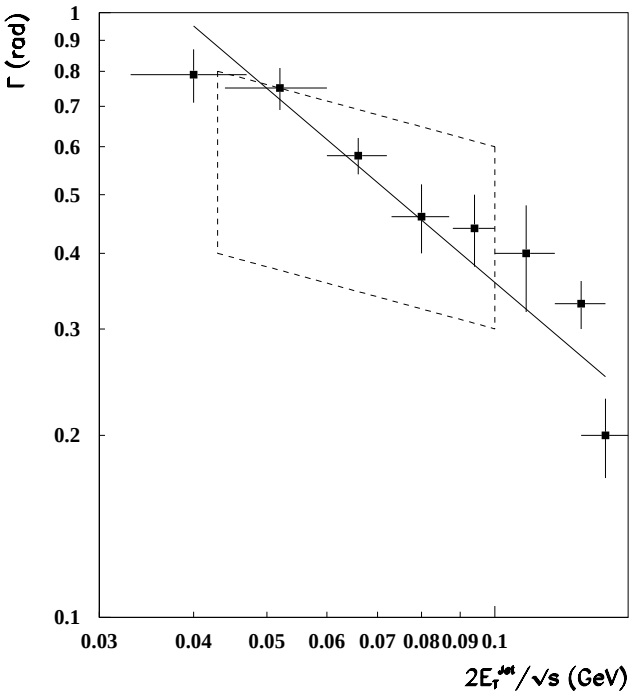

Figure 4.7: *The comparison of jet widths taken from H1 data (points) with those taken from the Monte–Carlo (inside the dashed line) the straight line is a* $1/E_T^{jet}$ *fit to the data.*

is the best fit line from the corresponding figure in [39]. The area inside the dashed line is the region attainable in this analysis with an acceptable χ^2 (i.e. $\chi^2/ndf < 1.8$). The jet energy was increased simply by increasing the average energy per hit, λ, and/or the multiplicity, n, so that the fits remained within the χ^2 range. The value of $\sqrt{s_{ep}}$ was taken to be 300 GeV.

The area inside the dashed line does show the same trend as the data in that the width decreases with the jet energy. This is the case because the jet energy is increased by either raising the average energy of each hit or increasing the number of hits or both. Fig. 4.3 shows that as the multiplicity increases the width of the jets grows slowly, while the average energy per hit increases the width decreases at a much faster rate. Therefore the width of a jet tends to decrease as the jet energy increases.

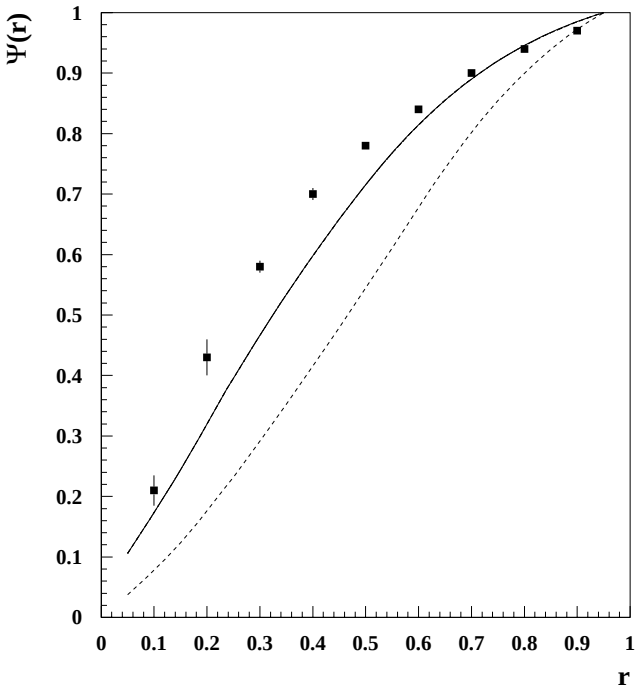

Figure 4.8: *The measured jetshape $\psi(r)$ for jets with $14 < E_T^{jet} < 17$ GeV and in the η_{jet} range between -1 and 2. The squares are ZEUS data and the solid line is the simple Monte Carlo with a multiplicity of 12 and an average E_T of 1.5 GeV. The dashed line is the simple Monte Carlo with a multiplicity of 30 and an average E_T of 1.0 GeV (the same as in Fig. 4.1).*

4.8 Jetshape

Previous papers [27, 33] examined structure within a jet, found with the cone algorithm. The jetshape $\psi(r)$ is defined as the average fraction of a jet's transverse energy E_T^{jet} that lies within a cone of radius r in $\eta - \phi$ space measured from the jet axis.

$$\psi(r) = \frac{1}{N_{jets}} \sum_{jets} \frac{E_T^{jet}(r)}{E_T^{jet}(r=1)}$$

$E_T^{jet}(r)$ is the energy of the jet between the jet axis ($r = 0$) and r. The sum runs over all N_{jets} jets in the sample. By definition $\psi(r = 1) = 1$ and $\psi(r = 0) = 0$. Again the data from [27] could be compared to the results obtained from the simple Monte Carlo (Fig. 4.8).

The simple Monte Carlo with a fixed multiplicity of 12 and an average energy per hit of 1.5 GeV agrees as well with the data as more sophisticated Monte Carlos. Due to the high transverse energy of these jets (the threshold is 14 GeV) and the relatively low multiplicity these jets were produced infrequently. However, when the default multiplicity of 30 and average energy of 1.0 GeV are used the agreement is not so good. It should be noted that the jets found are of a higher energy than in earlier sections as this was the only availiable data for the comparison. In the data the multiplicity and the average hit energy are therefore functions of jet energy, and as the jet energy increases the simple Monte Carlo finds it increasingly more difficult to reproduce the jetshape.

4.9 Conclusions

Jet–finding algorithms using the cone technique are defined by search parameters. Such algorithms still find 'jets' in a simple isotropic simulation containing no explicit physics. The jets produced exhibit the same properties as jets found in real data and, when the threshold is low (7 GeV), are found at the same rate as in the data. This is not to say that the jets in the data are spurious but that profile evidence advanced is insufficient to prove validity. Jets of very low transverse energy have been discovered in experiments even when the threshold is set very low [42]. These 'minijets' have aspects of the associated profile which suggest they could simply be an artifact produced by the cone algorithm, such as has been shown in this paper. A search cone of a particular size and shape will find jets of the same size and shape. When an initiator hit is used as a trigger, the resulting jet–profiles always have an inner, hard core produced by that initiator. At low energies distinctive dips are seen on the edge of the search cone area. It could be said that although useful for reconstructing the partonic direction, the energy profiles, jet rates and even jet transverse energy spectra resulting from the cone algorithm tell us little more about the physics of the events than simply the average energy and the multiplicity of the constituent hits. These values of multiplicity and average energy are in fact functions of the energy of the event. As the jet energy increases the simple Monte Carlo has less predictive power; the jet shape becomes more difficult to reproduce. If the value of λ is kept at 1 GeV, the jets produced in the Monte Carlo begin to have different properties from data–jets at jet transverse energies above 15 GeV. This could, in principle, be rectified by increasing λ, but only at the cost of increasing the complexity of the model.

Chapter 5

Event Selection

5.1 Introduction

This chapter details the event and track selections used for this analysis and investigates the various methods for reconstructing the event kinematics.

5.2 Event Classification

The majority of the data that is recorded is due to beam–gas, cosmic–ray and photoproduction events. Only a small portion of the data is the neutral current DIS events studied in this analysis.

The topology of a particular event is used to determine the event classification. The event classes used by this analysis are the neutral current low Q^2 (NCLQSQ) and the neutral current high Q^2 (NCHQSQ) classes.

The low Q^2 selection requires an electron to be found in the SpaCal and a corresponding track in the BDC. The radial distance between the "centre of gravity" of the SpaCal electron cluster and the BDC track is not allowed to be greater than 2 cm and the maximum distance in the azimuthal direction is 2.5 cm. The radius of the SpaCal cluster is also restricted to 3.5 cm. To reject those events where energy leaks out of the innermost part of SpaCal into the beam pipe a cut is applied to remove events whose radial distance from the BDC hit to the beam line is less than 9 cm.

To be considered for the high Q^2 class an event requires an electron candidate in the Liquid Argon Calorimeter. Electron candidates require more than 50% of their energy in the electromagnetic section of the calorimeter. The event must have less than 40 GeV of missing transverse momentum. These two criteria are set loosely enough to ensure that high Q^2 events are not rejected due to detector or reconstruction effects. The electron candidate must also pass one of the following two constraints:

- $10^\circ \leq \theta_e \leq 45^\circ$ and $E_T^e \geq 8$ GeV
- $45^\circ \leq \theta_e \leq 160^\circ$ and $E_T^e \geq 5$ GeV

An event is then classified as high Q^2 if it has at least one "good" central or forward track. To be defined as good the track must pass one of the selections detailed below.

5.3 Event Selection

The initial event selection requires events not to be coincident with electronic noise in the calorimetry. Subsequent selections require that the data were taken when all the high voltages of the detectors relevant to the analysis were switched on. The following selections were also applied. Each of the kinematic cuts is shown on the x, Q^2 plane in Fig. 5.1, together with the 1996 data, and discussed and motivated in the following sections.

5.3.1 Electron Selection

The number of photo–production events occurring in the H1 apparatus is much higher than the number of DIS events. In photo–production the electron scatters through a small angle and is lost down the beam pipe. However, photo–production remnants, such as low energy pions, can be misidentified as low energy electrons. This photo–production contamination is removed by ensuring that the energy of the scattered electron is greater than 14 GeV in the low Q^2 sample.

It was noticed in 1996 that with high Q^2 data there was a problem with the confinement of the scattered electron in the BBE region of the Liquid Argon calorimeter (see Figs. 1.6 and 1.7). It was decided to remove all events with an electron in this region so only

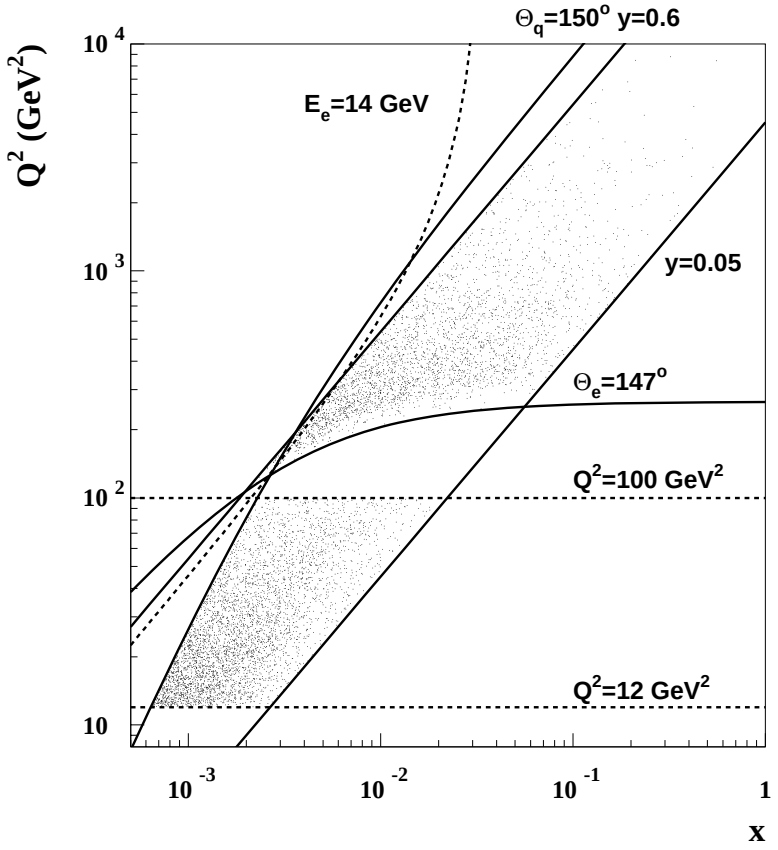

Figure 5.1: *The kinematic cuts applied to 1996 H1 data. The numbers of events have been reduced for presentational purposes.*

electrons with $10° < \theta_e < 147°$ were accepted, also a cut on the calorimeter z impact position ($z_{pos} > -140$cm) was applied. The removal of these events produces a hole in kinematic plane (see Fig. 5.1). This does not effect the analysis as all the variables used in the analysis vary smoothly in this region.

5.3.2 Detector Acceptance

At low Q^2 a further cut on kinematic quantities is applied. The polar angle of the struck quark (θ_{quark}) is calculated using four momentum conservation with the scattered lepton and assuming that the quark is massless. To maintain good detector acceptance $10° < \theta_{quark} < 150°$ is required, which means that the majority of the hadronic system will be inside the acceptance of the H1 trackers.

5.3.3 Vertex Position

The H1 tracking system is used to determine the z position of the event vertex. A well defined z–vertex (and also accurate calorimetry) ensures that the kinematic variables are well determined by the scattered electron properties and also removes cosmic–ray events. In this analysis the data are required to have a reconstructed event vertex within 30 cm of the nominal vertex position.

5.3.4 Diffractive Events

Most DIS events produce considerable energy in the forward region, which is usually associated with the proton and is known as the proton remnant. However about 6% of the DIS events observed at H1 have very little detected forward energy. These large rapidity gap (or diffractive) events are postulated to be produced by the exchange of a colourless object between the proton and the virtual boson, and are not modelled by the Monte–Carlos used in this analysis. These events are removed from the data sample by ensuring there is greater than 0.5 GeV of energy deposited in the Liquid Argon Calorimeter in the region $4.4^\circ < \theta < 15^\circ$.

5.3.5 QED Radiation

In the very large and very small y regions QED radiative corrections are large [43]. To minimise this problem a cut on the y variable calculated by both the Electron (see Section 5.5.1) and Jacquet–Blondel methods (see Section 5.5.2) is applied. The cut requires y, taken from both the Electron only and the Jacquet–Blondel methods, to be in the range $0.05 < y < 0.6$. To further reduce the radiative effects and remove photoproduction background an $E - p_z$ condition is imposed. $E - p_z$ is the sum $\Sigma_i(E^i - p_z^i)$ over all calorimeter energy deposits and it should be approximately equal to twice the electron beam energy (55 GeV). Lower values of $E - p_z$ are produced in photoproduction events where the large negative p_z of the electron and its energy E_i are missed making the sum much smaller. $E - p_z$ is required to be between 35 GeV and 70 GeV.

5.4 Track Selection

The H1 tracking system (described earlier) consists of a central and a forward tracker. Tracks which pass through the central tracker are subject to a central track selection whilst a similar selection is used for forward tracks. Tracks which pass through both chambers must undergo a combined track selection. The next sections detail the criteria used to select tracks originating from the interaction point.

5.4.1 Central Track Selection

1. $20^\circ < \theta_{\text{Track}} < 160^\circ$
2. Transverse momentum (P_T) > 0.15 GeV. This ensures that the track can escape the beam pipe and pass through both chambers of the CJC.
3. The track must be associated with a vertex so the distance of closest approach (DCA) of the track in the x–y plane to the z–axis is less than 2.0 cm.
4. The radial distance from the beam line to the start of the track (R_0) must be less than 50.0 cm, where the start of the track is defined as the innermost hit associated with that track.
5. Tracks with $\theta_{\text{Track}} < 150^\circ$ must be longer than 10.0 cm and tracks with $\theta_{\text{Track}} > 150^\circ$ must be longer than 5.0 cm.

5.4.2 Forward Track Selection

1. $6^\circ < \theta_{\text{Track}} < 25^\circ$
2. $p > 0.5$ GeV. The cut on momentum is to suppress the products of low momentum scattering in the end wall of the CJC.
3. Track momentum is determined by track curvature. Energetic particles produce a straight track and so the momentum error, $\delta p/p$, is large. These tracks are also subject to poor simulation. We require $\delta p/p \leq 1.0$.
4. $R_0 < 10.0$ cm.
5. The $\chi^2_{vertex\ fit}/NDF$ for a vertex fit has to be less than 10.0.

6. To suppress tracks that are associated with wrong hits in the forward tracker a fit is applied to each track and the requirement $\chi^2_{track\ fit}/NDF \leq 25.0$ enforced.

5.4.3 Combined Tracks

The following criteria are applied to tracks which traverse both trackers:

1. DCA < 5.0 cm.
2. $\chi^2_{track\ fit}/NDF \leq 50.0$
3. $p_T > 0.15$ GeV
4. $\delta p/p \leq 1.0$
5. $R_0 < 50.0$ cm.

5.4.4 Summary

Figs 5.2 and 5.3 are plots of event and track variables after the various selections have been applied for both data (points) and Monte Carlo (line) for the low and high Q^2 samples respectively. It can be seen from these plots that the data and Monte Carlo are in good agreement for all the distributions shown. Table 5.1 shows the number of events that occur in each of the Q^2 bins used in this analysis.

5.5 Reconstructing Event Kinematics

The kinematic variables x and Q^2 are essential when boosting to the Breit frame; it is therefore necessary to measure these variables as accurately as possible. There are several different ways to determine the event kinematics since the system is over constrained. The energies of the beams are already known and only another two variables are required to determine the kinematics. The following known or measured quantities are used in the differing methods:

- E_E = electron beam energy,

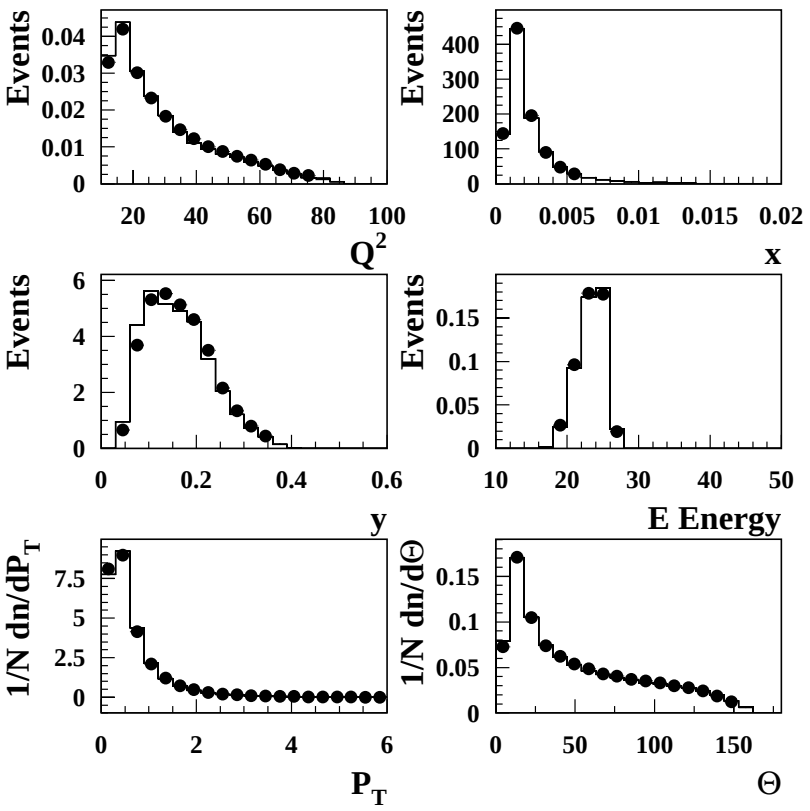

Figure 5.2: *Plots of event and track variables after the data selection has been applied for 1996 low Q^2 data (solid circles) and the MEAR Monte Carlo (solid line).*

- E_p = proton beam energy,
- E'_e = energy of scattered electron,
- θ_e = polar angle of scattered electron,
- γ = polar angle of outgoing scattered hadronic system.

5.5.1 The Electron Method

The Electron Method only uses information from the scattered electron. The neutral current DIS variables used in this thesis are calculated using this method. The boost to the Breit frame can then be performed independently of the hadronic system thus explicitly not biasing it. The Electron Method variables can be calculated thus:

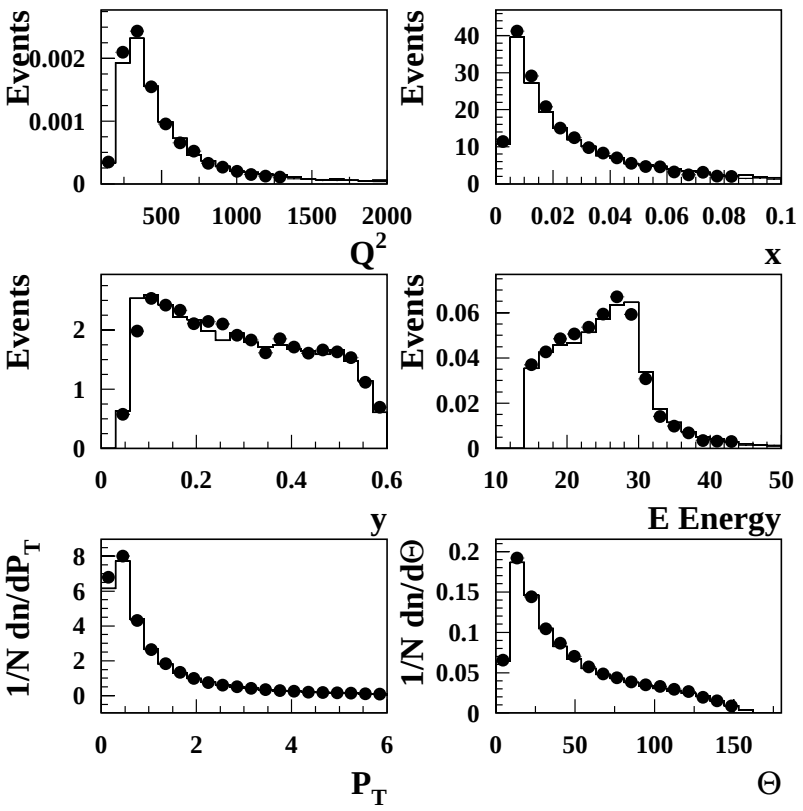

Figure 5.3: *Plots of event and track variables after the data selection has been applied for 1996 high Q^2 data (solid circles) and the MEAR Monte Carlo (solid line).*

$$Q_e^2 = 2E_e E'_e(1 + \cos\theta_e) \tag{5.1}$$

$$y_e = 1 - \frac{E'_e}{2E_e}(1 - \cos\theta_e) \tag{5.2}$$

$$x_e = \frac{E_e E'_e(1 + \cos\theta_e)}{E_p(2E_e - E'_e(1 - \cos\theta_e))} \tag{5.3}$$

where x_e is calculated from $Q_e^2 = s x_e y_e$. A problem with the electron only method is that QED radiation can effect the angle and energy of the scattered electron which results in a mis–calculation of the event kinematics.

Q^2 interval (GeV^2)	$\langle Q \rangle$ (GeV)	Events
12 - 15	3.7	14210
15 - 20	4.2	16731
20 - 40	5.3	32170
40 - 60	7.0	13287
60 - 80	8.3	8347
80 - 100	9.5	4989
100 - 175	12.6	229
175 - 250	14.6	967
250 - 450	18.3	3278
450 - 1000	25.0	2261
1000 - 2000	36.6	635
2000 - 8000	55.8	253

Table 5.1: *The average value of Q and the number of events in the Q^2 bins adopted for this analysis.*

5.5.2 The Jacquet–Blondel Method

The Jacquet–Blondel (JB) Method was developed for determining the kinematics of charged–current events. In this case the scattered lepton is a neutrino which passes undetected through the apparatus. The JB or hadron–only method only uses the information from the hadronic final state. Due to the loss of hadrons down the beam pipe this method produces a poor measurement of Q^2 but does give a precise measure of y at low to medium y ($y < 0.2$). In the following equations h denotes hadrons:

$$y_{JB} = \frac{\Sigma_h (E_h - p_{z,h})}{2E_e} \tag{5.4}$$

$$Q^2_{JB} = \frac{(\Sigma_h p_{z,h})^2 + (\Sigma_h p_{y,h})^2}{1 - y_{JB}} \tag{5.5}$$

$$x_{JB} = \frac{Q^2_{JB}}{s y_{JB}} \tag{5.6}$$

5.5.3 The Double Angle Method

The Double–Angle (DA) Method uses the electron scattering angle and the average angle of the hadronic final state. The DA method assumes an homogeneous energy measurement over the full solid angle but is independent of the absolute energy calibration of the calorimetry.

$$Q^2_{\theta_e\gamma} = 4E_e^2 \frac{\sin\gamma(1+\cos\theta_e)}{\sin\gamma + \sin\theta_e - \sin(\theta_e+\gamma)} \tag{5.7}$$

$$y_{\theta_e\gamma} = \frac{\sin\theta_e(1-\cos\gamma)}{\sin\gamma + \sin\theta_e - \sin(\theta_e+\gamma)} \tag{5.8}$$

$$x_{\theta_e\gamma} = x_o \frac{\sin\gamma + \sin\theta_e + \sin(\theta_e+\gamma)}{\sin\gamma + \sin\theta_e - \sin(\theta_e+\gamma)} \tag{5.9}$$

where $x_o = E_e/E_p$.

5.5.4 The Σ Method

The Σ Method reconstructs DIS kinematic variables independent of initial state QED radiation by reconstructing the initial electron energy. The Σ Method was first proposed in [44, 45]. The formulae for kinematic variables are as follows:

$$\Delta \equiv \Sigma + E'_e(1-\cos\theta_e) = 2E_e \tag{5.10}$$

where $\Sigma = \Sigma_h(E_h - p_{z,h})$. If no particles escape detection the quantity Δ will equal twice the incident electron energy. Thus substituting Δ into y_{JB} leads to:

$$y_\Sigma = \frac{\Sigma}{\Sigma + E'_e(1-\cos\theta_e)} \tag{5.11}$$

$$Q^2_\Sigma = \frac{E'^2_e \sin^2\theta_e}{1-y_\Sigma} \tag{5.12}$$

$$x_\Sigma = \frac{Q^2_\Sigma}{s y_\Sigma} = \frac{E_e'^2 \sin^2 \theta_e}{s y_\Sigma (1 - y_\Sigma)} \tag{5.13}$$

5.5.5 The Mixed Method

The mixed method utilises the y measurement from the JB method together with the Q^2 measurement from the electron method. This can be used to extend the DA or electron method measurements to lower y values andresults in:

$$x_{MI} = \frac{Q^2}{s y_{JB}} \tag{5.14}$$

5.5.6 Summary

Table 5.2 shows the resolution in x and Q^2 for the Q^2 bins used in this analysis for each of the reconstruction methods [46] and Figs. 5.4-5.7 show the resolution in Q^2 and x for the Q^2 bins used in this analysis for both the high and low Q^2 samples. It is clear from the table that the electron only method has a better resolution in Q^2 than any other method in all the Q^2 bins. The electron only method has a good resolution in x at low Q^2 but at high Q^2 the resolution from the double angle method is marginally better. The means of some of the figures have significant shifts from zero. The correction procedure (see Chapter 7) ensures that the shifts in the mean do not effect the analysis.

Q^2 interval	$\Delta x/x_T$					$\Delta Q^2/Q_T^2$				
(GeV^2)	EL	DA	JB	MI	Σ	EL	DA	JB	MI	Σ
12 - 15	0.26	0.53	0.41	0.43	0.35	0.074	0.12	0.25	0.074	0.081
15 - 20	0.25	0.53	0.48	0.43	0.34	0.063	0.094	0.34	0.063	0.070
20 - 40	0.25	0.44	0.67	0.43	0.32	0.077	0.11	0.57	0.077	0.083
40 - 60	0.25	0.40	0.94	0.42	0.32	0.095	0.14	0.89	0.095	0.10
60 - 80	0.27	0.36	0.97	0.43	0.33	0.10	0.12	1.00	0.10	0.15
80 - 100	0.28	0.34	0.93	0.40	0.29	0.13	0.15	0.95	0.13	0.13
100 - 175	0.25	0.33	0.29	0.40	0.26	0.18	0.21	0.25	0.18	0.19
175 - 250	0.31	0.31	0.33	0.37	0.28	0.17	0.20	0.30	0.17	0.20
250 - 450	0.31	0.29	0.40	0.33	0.27	0.14	0.19	0.41	0.14	0.15
450 - 1000	0.31	0.25	0.45	0.29	0.24	0.21	0.23	0.59	0.21	0.20
1000 - 2000	0.25	0.19	0.40	0.22	0.19	0.22	0.26	0.56	0.22	0.22
2000 - 8000	0.25	0.21	0.45	0.24	0.22	0.10	0.20	0.38	0.10	0.11

Table 5.2: *The rms resolution in Q^2 and x for the Q^2 bins used in this analysis for each of the reconstruction techniques. Note that for the mixed method Q^2 is defined so that it is the same as the electron only method.*

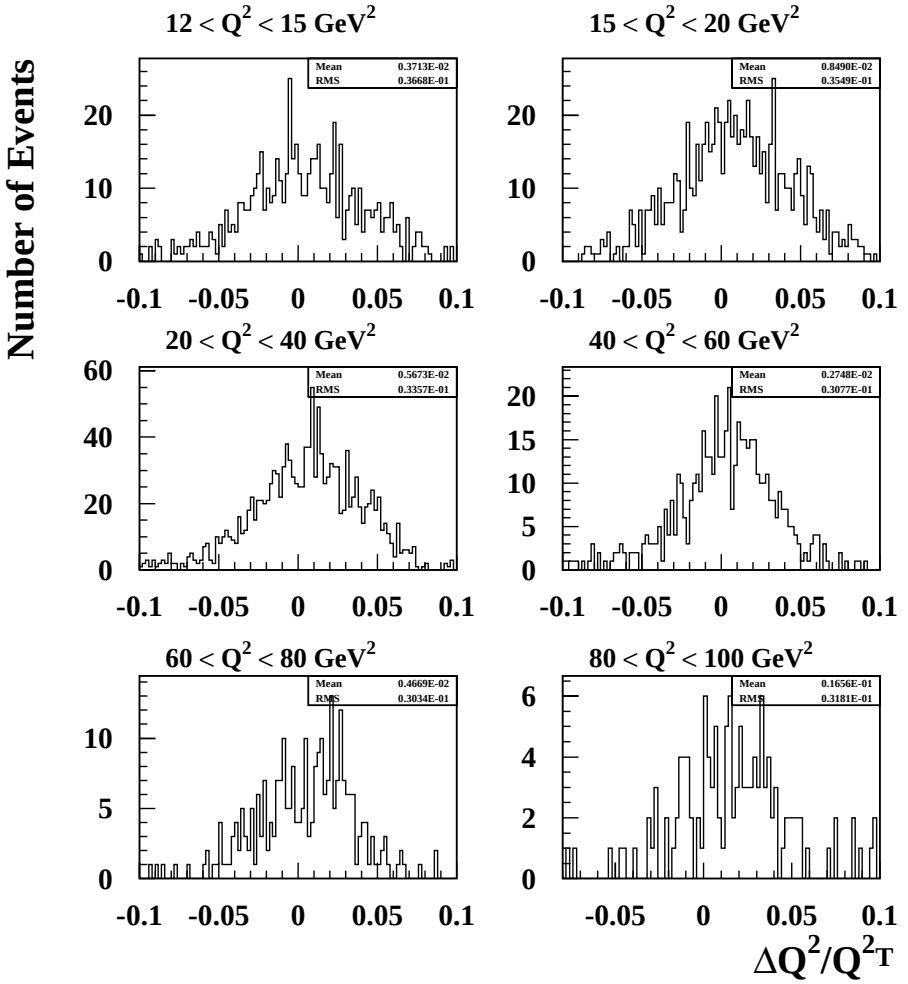

Figure 5.4: *The resolution in Q^2 over a range of low Q^2 bins.*

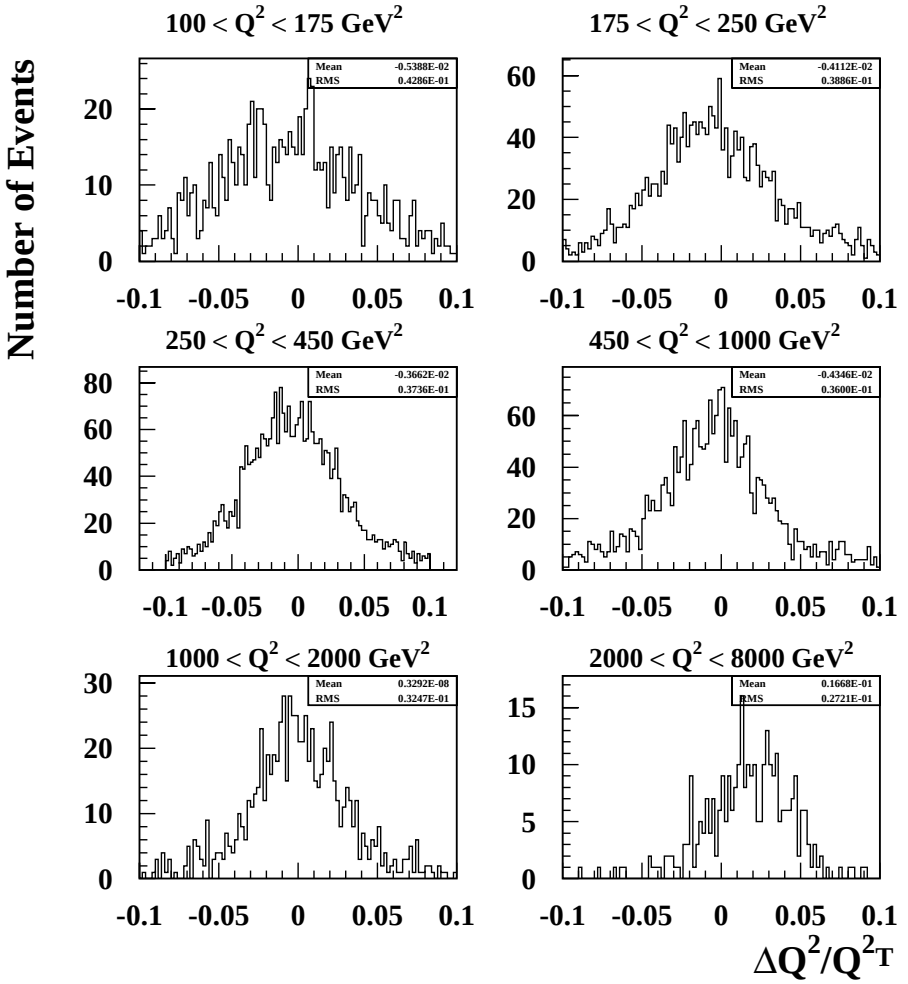

Figure 5.5: *The resolution in Q^2 over a range of high Q^2 bins.*

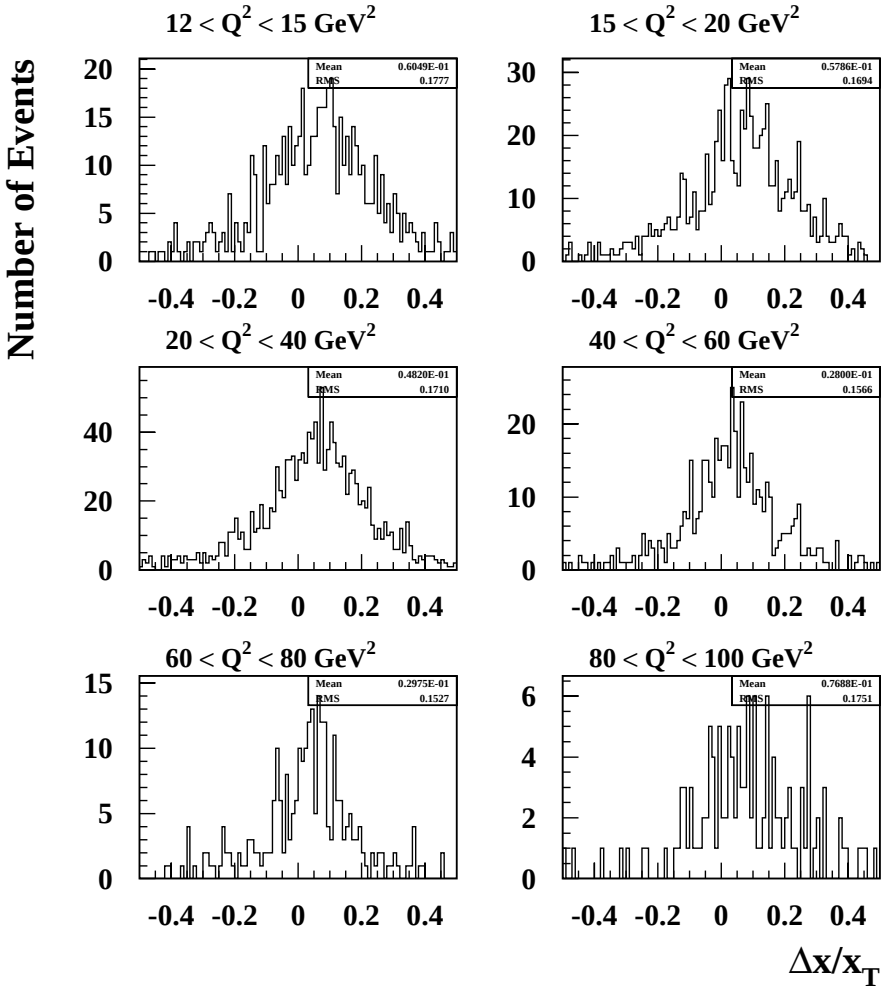

Figure 5.6: *The resolution in x over a range of low Q^2 bins.*

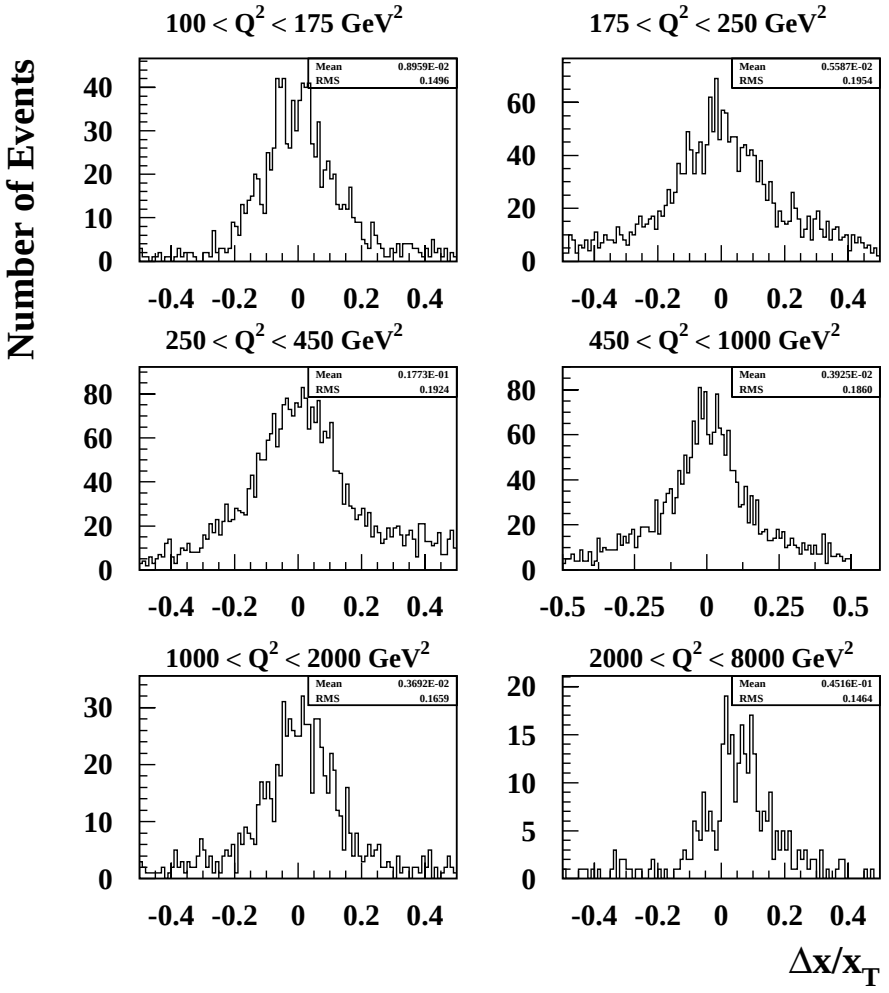

Figure 5.7: *The resolution in x over a range of high Q^2 bins.*

Chapter 6

The Breit Frame

6.1 The Breit Frame of Reference

The Breit Frame of Reference is co–linear with the hadronic centre of mass (HCM) frame, but with a further boost in the z-direction. In the Breit frame the positive z–direction is defined as the direction of the incoming proton. The extra boost is performed so that the incoming virtual photon has zero energy, zero transverse momentum and a z component of momentum equal to $-Q$, see Fig. 6.1. In the naïve quark parton model the incoming massless quark carries a fraction x of the proton's momentum and has an energy of $Q/2$ and a z component of momentum equal to $+Q/2$. After scattering the quark still has an energy of $Q/2$ but its z component of momentum is reversed ($p_z = -Q/2$), which is why the Breit frame is also known as the Brick Wall frame. The direction of the struck quark, the negative z–direction, is referred to as the current hemisphere. By comparison with e^+e^- events it can be shown that in the Breit frame Q is directly equivalent to the e^+e^- centre of mass energy, E^*.

Rapidity (Y) for a given track is defined by:

$$Y = \frac{1}{2}\ln\left(\frac{E + p_z}{E - p_z}\right) \tag{6.1}$$

where E is the energy and p_z is the longitudinal momentum of each track. E is calculated assuming each charged hadron has the mass of a pion. When $p >> m$, Y can be approximated by pseudo–rapidity (η) which is defined as $\eta = -\ln(\tan(\theta_{Breit}/2))$, the incoming proton moves in the positive z direction with $\theta = 0^\circ$ polar angle. The positive Y or η

direction is that of the incoming proton and the negative direction that of the virtual photon.

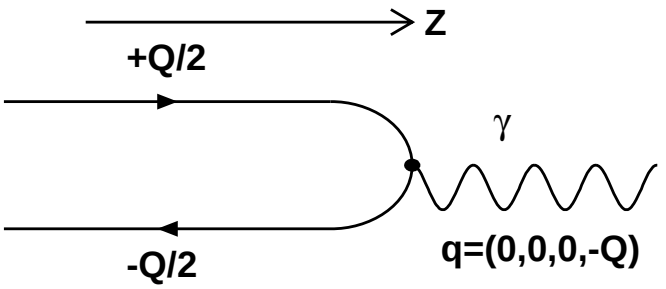

Figure 6.1: *A schematic diagram of the Breit frame of reference.*

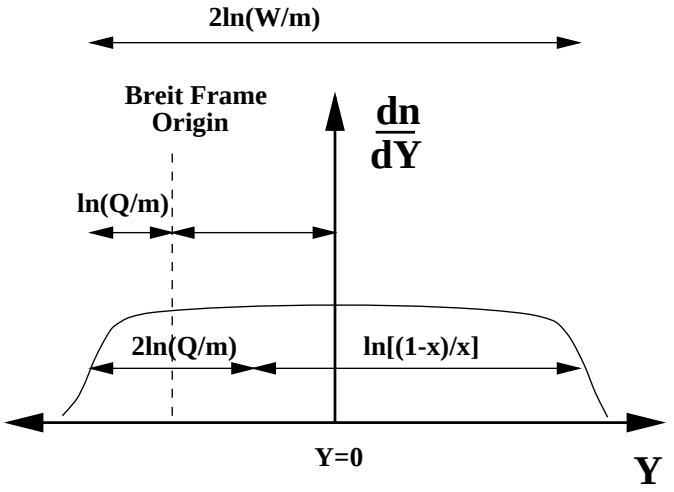

Figure 6.2: *The rapidity plateau as seen in the hadronic centre of mass.*

According to Feynman [23] the rapidity distribution of the charged tracks is expected to be a flat plateau as a result of the relativistic contraction of the target in the beam direction. In either the Breit Frame or the hadronic centre of mass frame, the phase space width of the whole distribution for hadrons of mass m scales with energy and can be expressed as:

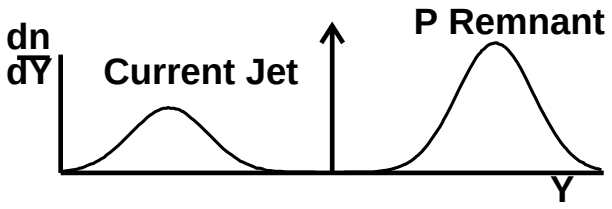

Figure 6.3: *The rapidity plateau as predicted by Gribov using QCD.*

$$2\ln(W/m) = 2\ln(Q/m) + \ln((1-x)/x) \tag{6.2}$$

since the total hadronic mass squared is $W^2 = Q^2(1-x)/x$ given negligible proton mass when compared to W (see Fig. 6.2).

In the Quark Parton Model (QPM) the hadronic final state of DIS consists of a (current) jet of hadrons originating from the struck quark and the particles produced by the proton remnant. In the laboratory the proton remnant has little transverse momentum, so the transverse momentum of the scattered lepton is balanced by the current jet. In the Breit frame there is no parton transverse momentum, the quark would be at $Y \to -\infty$ and the proton remnant would be at $Y \to +\infty$, and fragmentation produces a rapidity distribution similar to Fig. 6.3. In the Gribov model [47] see Fig. 6.3, the central or low momentum part of the Feynman distribution collapses due to destructive interference of the gluons.

Full QCD makes the whole picture substantially more complicated. The phase space between the current jet and the proton remnant is filled with particles produced from the emission of gluons created by the colour transfer between the struck quark and the proton remnant. This returns the shape of the rapidity distribution to something approaching the Feynman picture.

When the particles have low transverse momentum, reflecting the low p_t of the par-

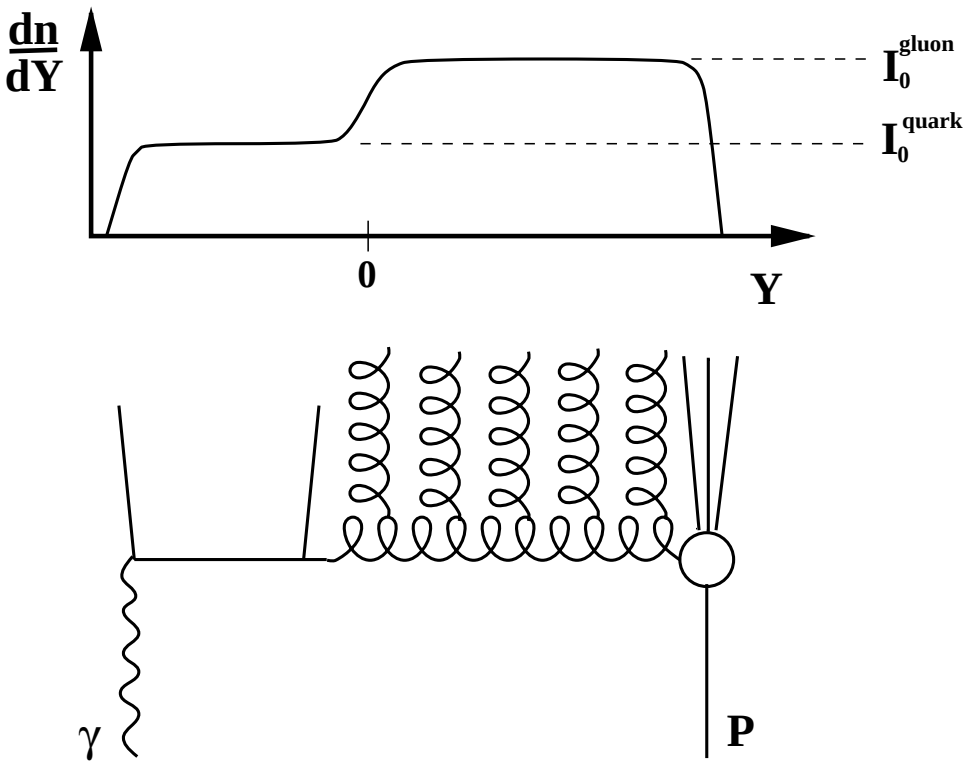

Figure 6.4: *The rapidity plateau at low p_T and the ladder type Feynman diagram that produces the step–like shape. The ratio $I_0^{gluon}/I_0^{quark} \approx 9/4$.*

tons, Local Hadron Parton Duality (LPHD) and colour charge predict [48] a difference in the respective heights (charged track multiplicity density) of the target and current regions. The exchanged gluon in the target regions produces a higher plateau in that area. The ratio of the heights reflects the ratio of the colour charge I_0^{gluon}/I_0^{quark} which is approximately 9/4 [49] see Fig. 6.4. This step like shape in the current hemisphere will be examined later in the analysis.

The current hemisphere of the Breit frame, when compared to the current hemisphere of the HCM frame, is dominated by the fragments of the struck quark. The high momentum proton remnants go entirely into the target hemisphere.

Another reason why the Breit frame was chosen for this analysis is illustrated in Fig. 6.5. In the laboratory frame low p_t tracks are removed, so it becomes impossible, in the lab, to examine tracks with a p_t below 0.15 GeV. The boost to the Breit frame changes the p_t behaviour, there is a correlation between p_t^{BREIT} and p_t^{LAB} (see Fig. 6.5) but it is still possible to study very low p_t^{BREIT} tracks after the p_t^{LAB} >0.15 GeV cut has been applied.

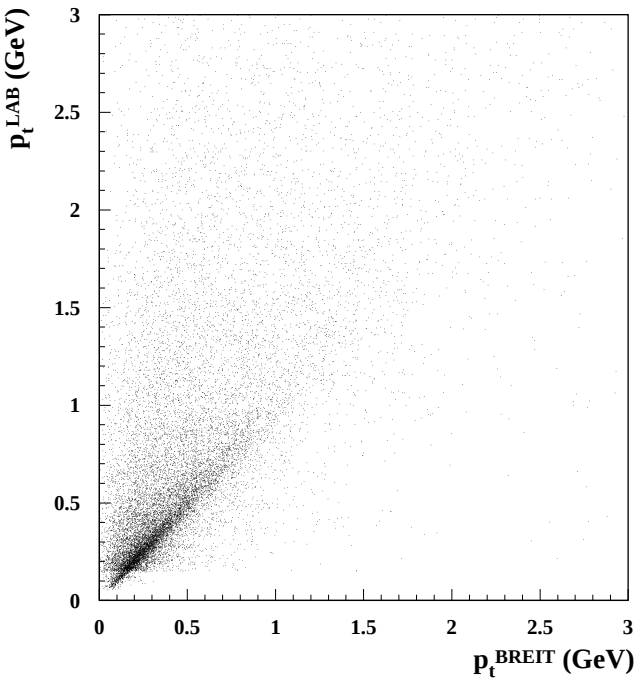

Figure 6.5: *A plot of p_t^{LAB} versus p_t^{BREIT} of charged tracks for high Q^2 data. The p_t cut ($p_t^{LAB} > 0.15$ GeV) placed on central tracks in the laboratory frame can be clearly seen.*

6.2 Higher Order Processes in the Breit Frame

Some first order QCD processes such as BGF and initial state CQCD do not have an analogue in e^+e^- physics. This is important as comparisons will be made later between the current hemisphere of the Breit frame and a single hemisphere of e^+e^-. Together with final state CQCD (which does occur in e^+e^- events) these leading order processes can depopulate the current hemisphere of the Breit frame (see Fig. 6.6). The depopulation can lead to events with empty current hemispheres. The treatment of these events is covered later in the analysis.

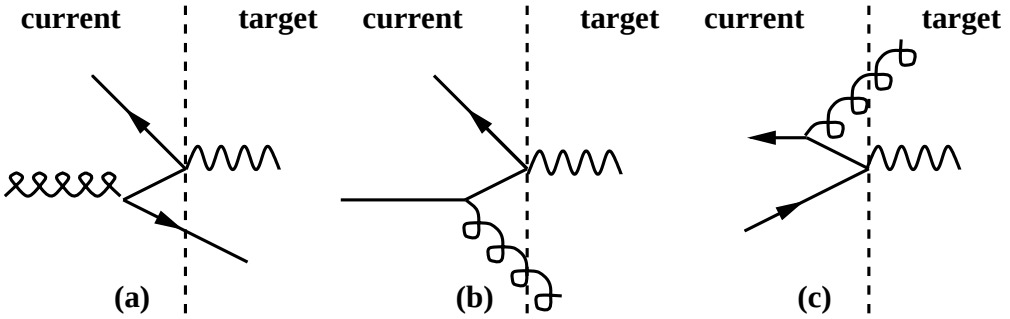

Figure 6.6: *Higher Order QCD processes can deplete the current hemisphere of the Breit frame. (a) BGF events and (b) Initial state CQCD processes do not occur in e^+e^- physics. (c) Final state CQCD events do occur in e^+e^- events.*

Chapter 7

Data Correction and Resolutions

7.1 Introduction

At no point in this analysis is a cross section calculated. All particle distributions are normalised by the number of events. The overall number of events is therefore unimportant and there is a certain freedom in the selection of the phase space for the sample of events used.

Data must be corrected for detector acceptance and inefficiencies. There are several different methods for performing this correction, the bin–by–bin method was used entirely for this analysis.

In addition the data can also be corrected for radiative effects. In DIS the incoming electron can radiate a real photon; this will change the four–vector of the electron and thus the kinematics of the event, particularly if the electron–only method is used, as in this analysis. If the kinematic variables x and Q^2 are not known precisely then the boost to the Breit Frame will not be performed correctly. This error can lead to events with an incorrect axis and hence under–populated or even empty current hemispheres. Monte Carlo programs model these radiative effects and can be used to determine a radiative correction to the data.

7.2 Data Correction

The analysis bins used in this work are chosen to be wider than the resolution but narrow enough to display any interesting physics properties. To correct for acceptance losses, the MEAR Monte Carlo is used for the whole of this analysis and radiative corrections are performed separately (see the next section). For the reconstructed Monte Carlo the detector response is modelled by H1–SIM which in turn uses the GEANT [50] package. The acceptance correction function F_i for the i^{th} bin is given by:

$$F_i^{\text{acc}} = \frac{n_i^{\text{gen}}}{n_i^{\text{rec}}} \tag{7.1}$$

where n is the number of events in the i^{th} bin after the generated events have undergone generator level selections and the reconstructed events have passed the same selection as the data. The error on this value is assumed to be uncorrelated and is given by:

$$\left(\frac{\delta F_i^{\text{acc}}}{F_i^{\text{acc}}}\right)^2 = \left(\frac{\delta n_i^{\text{gen}}}{n_i^{\text{gen}}}\right)^2 + \left(\frac{\delta n_i^{\text{rec}}}{n_i^{\text{rec}}}\right)^2 \tag{7.2}$$

The bin–by–bin corrections throughout this analysis are smoothly varying and are generally less than $\pm 20\%$ away from unity in any given distribution.

7.3 Radiative Corrections

Radiative corrections are performed in a similar way to acceptance corrections. In most cases the data are corrected back to the Born term by applying a radiative correction factor F_i^{rad} to the i^{th} bin:

$$F_i^{\text{rad}} = \frac{n_i^{\text{norad}}}{n_i^{\text{rad}}} \tag{7.3}$$

where 'rad' and 'no rad' refer to the generated MEAR Monte Carlo QED radiative effects turned on and off respectively. Again the radiative corrections within this analysis are small and smoothly varying in any given distribution.

The correction procedure is illustrated in Fig. 7.1, which plots the azimuthal angle of tracks in the Breit frame ($\phi_{\rm BREIT}$) for (a) raw data (D) compared to reconstructed Monte Carlo and (b) acceptance corrected data ($D \times F^{\rm acc}$) compared to generated Monte Carlo and finally (c) data corrected for radiation ($D \times F^{\rm acc} \times F^{\rm rad}$) compared to a non-radiative generated Monte Carlo. $\phi_{\rm BREIT}$ is a good variable for this comparison because radiative effects cause a rise in the distribution at $\phi_{\rm BREIT} = \pm\pi$. The acceptance corrected data still has this feature but the overall level has been raised to account for detector losses. Lastly the radiative corrections flatten out the distribution as expected.

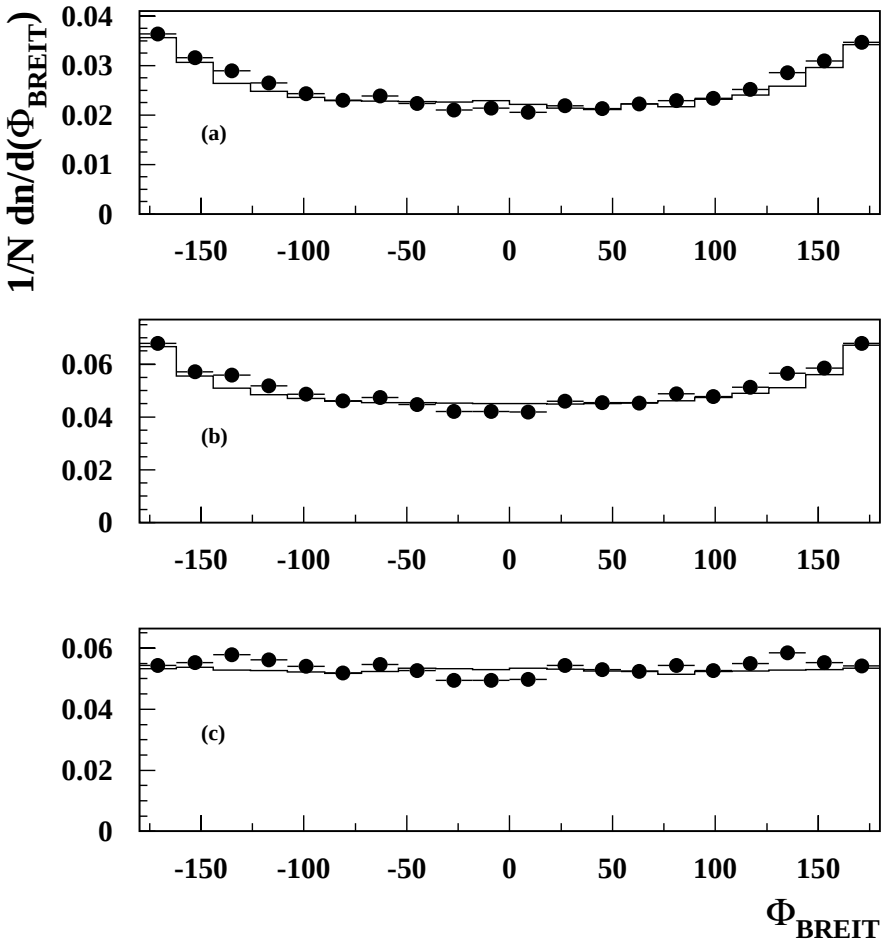

Figure 7.1: *The $\phi_{\rm BREIT}$ distribution for (a) raw data (points) compared to reconstructed Monte Carlo (line) (b) acceptance corrected data (points) compared to generated Monte Carlo (line) and (c) radiative corrected data (points) compared to a non-radiative generated Monte Carlo (line).*

7.4 Resolutions and Purities

The resolution in all variables consists of a small contribution from the reconstruction resolution and a large contribution from the boost resolution. The resolution in Y as a function of p_t, and E as a function of Q^2 for both high and low Q^2 data, which correspond to distributions presented later, are shown in Figs. 7.2–7.5 respectively.

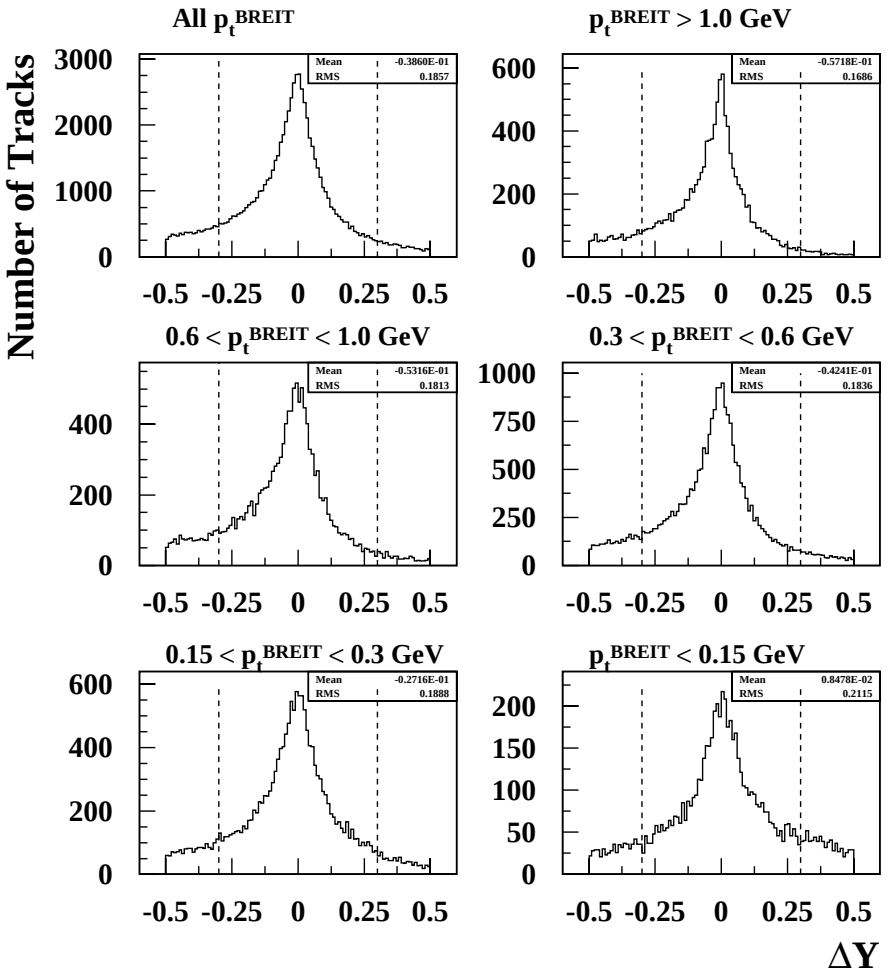

Figure 7.2: *The resolution in Y for a range of p_t bins for high Q^2 data. The bin–width ($Y \sim 0.6$) adopted is indicated by dashed lines.*

Purity is defined as the proportion of events that remain in a given analysis bin after the reconstruction procedure has been applied. The purities in Y and E are shown in Figs. 7.6–7.9. The purity is generally greater than 35% in all the bins of the analysis.

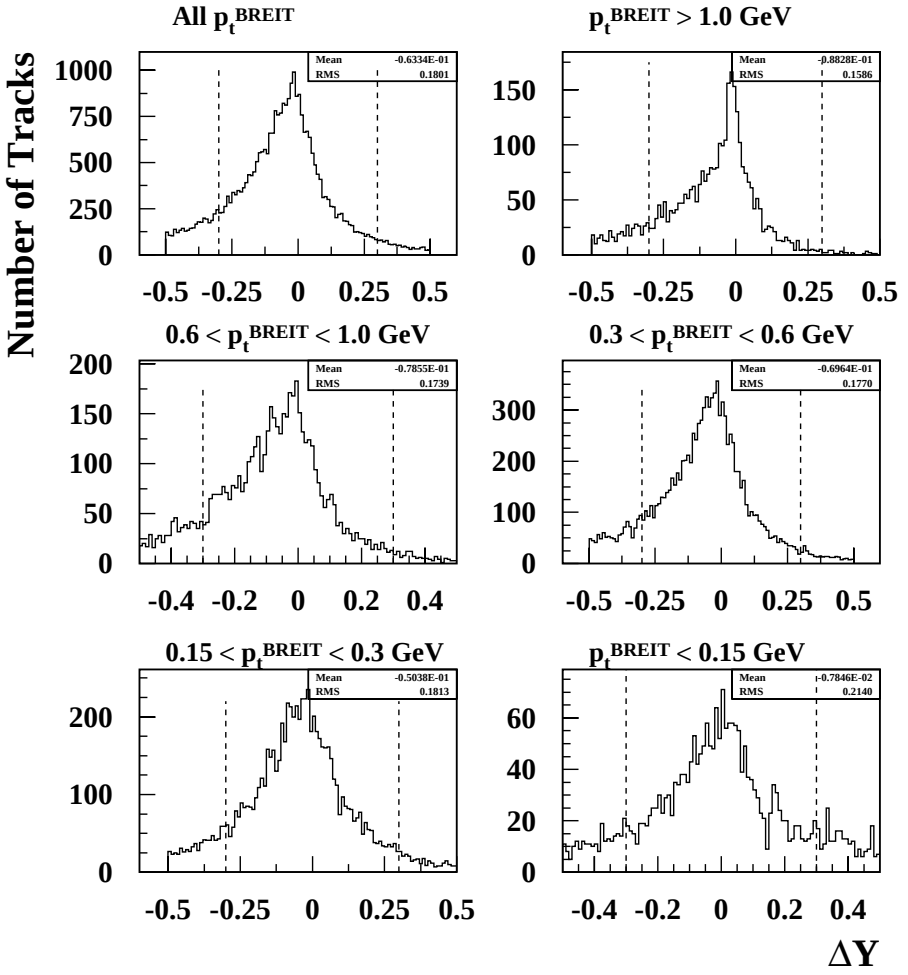

Figure 7.3: *The resolution in Y for a range of p_t bins for low Q^2 data. The bin–width ($Y \sim 0.6$) adopted is indicated by dashed lines.*

The bin–by–bin correction procedure works perfectly for the case where purity is high (resolution is low) and/or for the case where the data is well modelled by Monte Carlo. For intermediate cases there is a degree of dependence on the particular generated distribution. Independent checks on the accuracy of the modelling are made by using an alternative Monte Carlo (in this case MEPS). The MEAR Monte Carlo was found to describe the data well in all distributions presented in this analysis.

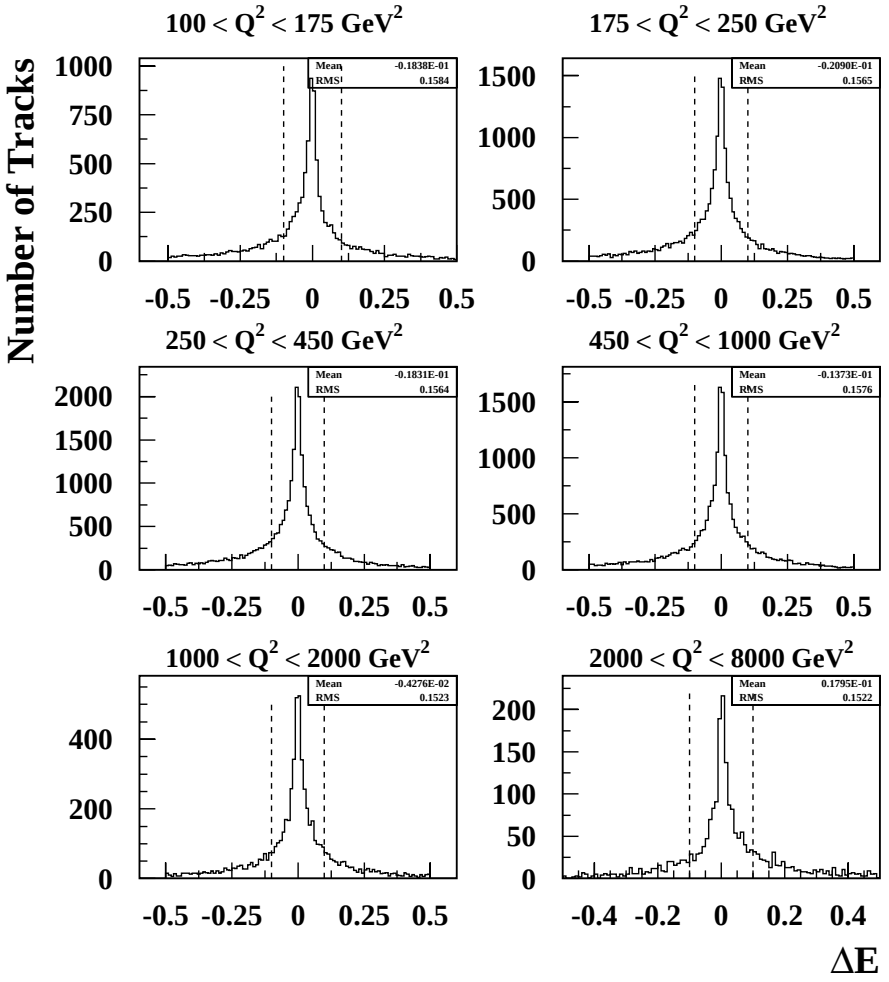

Figure 7.4: *The resolution in E for the high Q^2 bins used in this analysis. The bin–width ($E \sim 0.2$) adopted is indicated by dashed lines.*

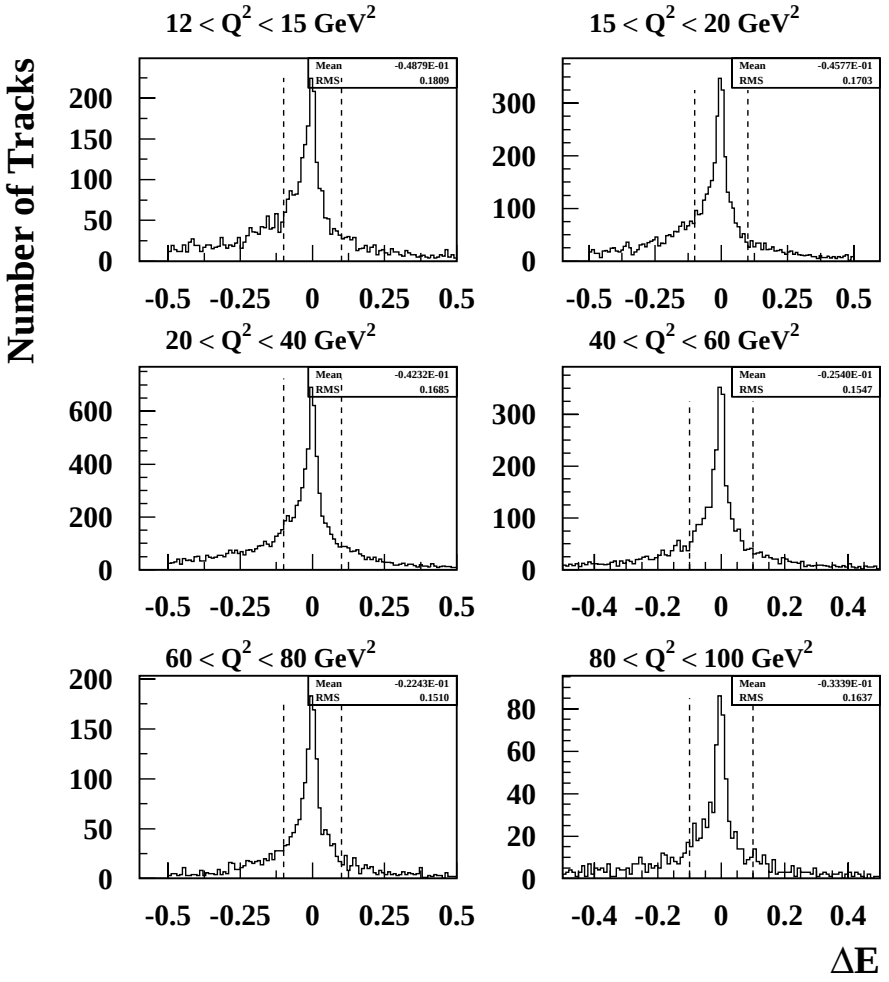

Figure 7.5: *The resolution in E for the low Q^2 bins used in this analysis. The bin–width ($E \sim 0.2$) adopted is indicated by dashed lines.*

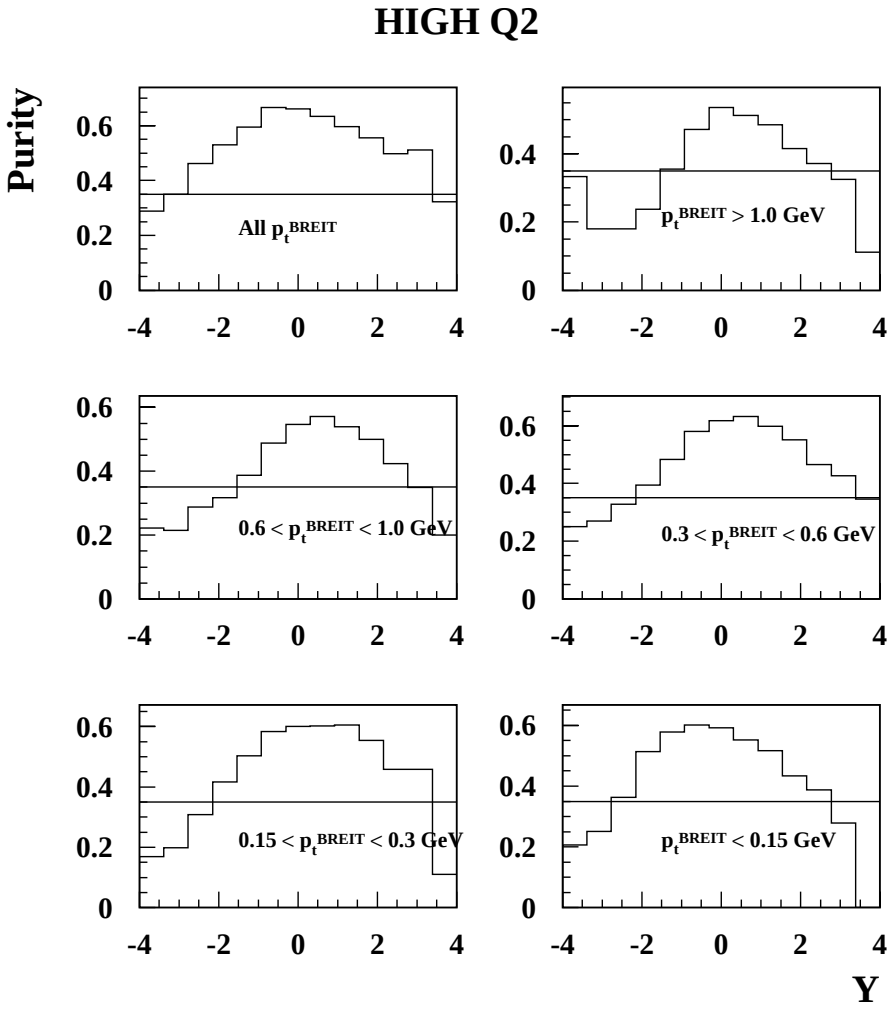

Figure 7.6: *The purity in Y for a range of p_t bins for high Q^2 data.*

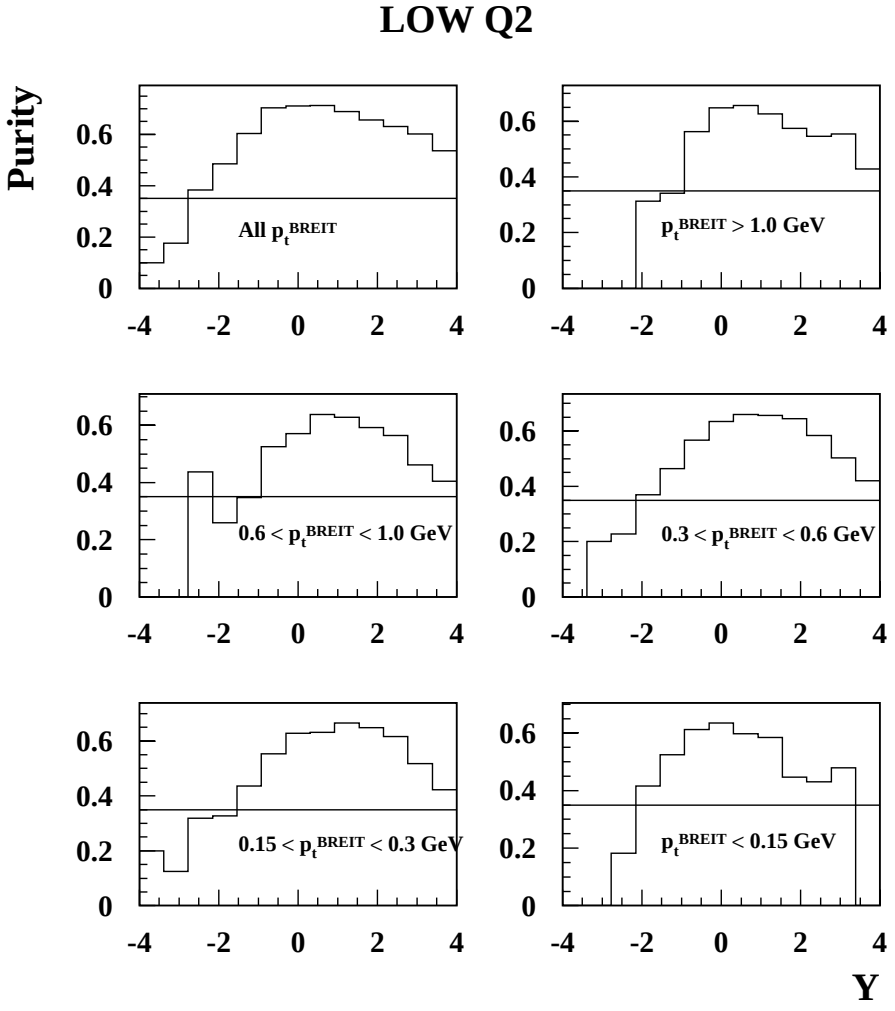

Figure 7.7: *The purity in Y for a range of p_t bins for low Q^2 data.*

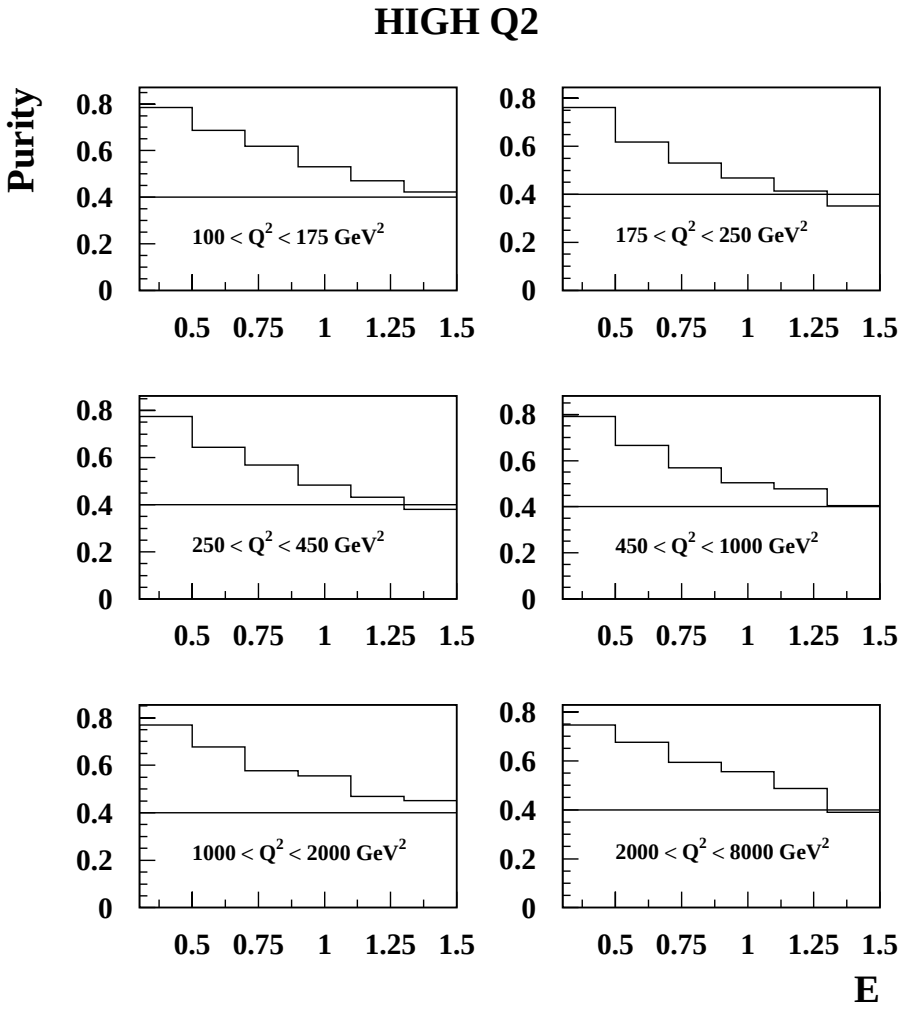

Figure 7.8: *The purity in E for the high Q^2 bins used in this analysis.*

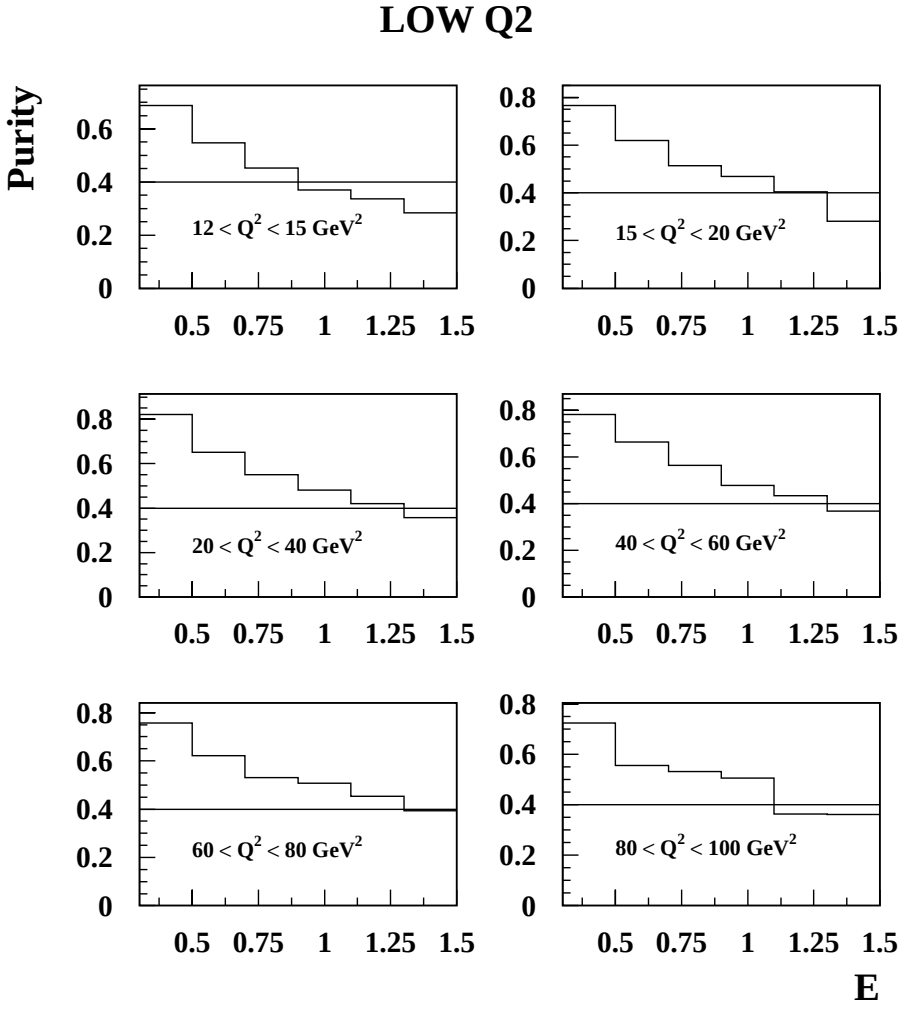

Figure 7.9: *The purity in E for the low Q^2 bins used in this analysis.*

Chapter 8

Thrust in the Breit Frame

8.1 Introduction

This chapter examines the event shape variable Thrust (T_z) and studies an event selection applied in a recent paper which used T_z to calculate α_s. The chapter then details a method for calculating the proportion of Boson–Gluon Fusion (BGF) events as a function of x using T_z. The BGF proportion is expected to decrease as x increases. If the proportion of the BGF events can be estimated for the data, and the cross section of BGF events is known, it is possible calculate the gluon density in the proton.

Event shape variables such as thrust (T_z) have been used by e^+e^- experiments to extract the strong coupling constant $\alpha_s(M_Z)$ independent of any jet algorithm [51]. A similar analysis can be performed with deep inelastic scattering events. The Breit frame is well suited to this analysis as the current hemisphere has been shown to be the analog of one e^+e^- hemisphere and good separation is achieved between the current and target regions. There is nearly 100% acceptance of the current hemisphere in the H1 detector.

The event shape variable thrust, T_z, is defined below. The sums extend over all hadrons h (defined experimentally as a calorimetric cluster in the detector with the scattered electron removed) with four–momentum $p_h = [E_h, \mathbf{p}_h]$ in the current hemisphere of the Breit Frame. In performing the boost to the Breit frame the cluster is assumed to have the mass of a single pion.

$$T_z = \frac{\Sigma_h |\mathbf{p}_h . \mathbf{n}|}{\Sigma_h |\mathbf{p}_h|} = \frac{\Sigma_h |\mathbf{p}_{zh}|}{\Sigma_h |\mathbf{p}_h|} \tag{8.1}$$

where $\mathbf{n}$ is the current hemisphere axis ($\mathbf{n} = [0, 0, -1]$). The normalised, uncorrected $1 - T_z$ spectra can be seen in Fig. 8.1. When the value of $1 - T_z$ is low for a particular event the event will have a well collimated jet of particles in the current hemisphere whilst the particles from an event with a high $1-T_z$ value will have a more isotropic distribution.

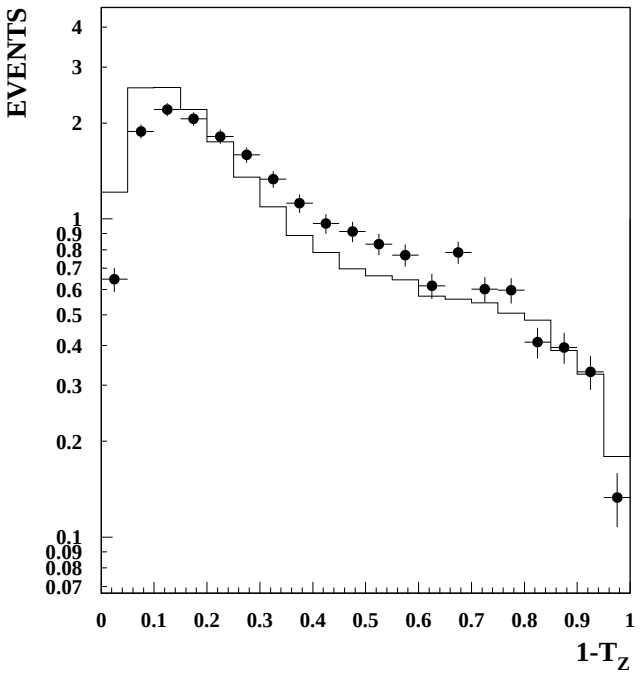

Figure 8.1: *The differential thrust T_z distribution for 1996 high Q^2 data (solid points) compared to MEAR Monte Carlo (solid line).*

A recent paper [52] examined event shape variables, including T_z, in deep inelastic scattering events in the Breit Frame. The results were compared to results from e^+e^- experiments and second order QCD calculations. The work of this chapter was motivated by one of the cuts in the event selection of that analysis. The cut imposed the following condition:

- The total hadronic energy in the Breit current hemisphere has to exceed 0.1 Q.

The $E_{BF} > 0.1Q$ cut was designed to suppress photoproduction events with a misidentified electron and to ensure that there was sufficient energy to calculate T_z but it was noted that the $E_{BF} > 0.1Q$ cut removed events that do not appear in e^+e^- physics, such as BGF events. The $E_{BF} > 0.1Q$ cut is very similar to the Breit frame energy flow

selection described below and used later in this analysis (see Chapter 9). The two cuts are compared in Fig. 8.2.

8.2 Variation of Thrust with E_{BF}/Q

The current hemisphere of a DIS Breit frame event may be compared to a single hemisphere of an e^+e^- interaction. To aid this comparison events which do not occur in e^+e^- physics can be rejected in a DIS sample. Boson Gluon Fusion and initial state Compton QCD events do not occur in e^+e^- physics. Both produce a lower than expected multiplicity in the current hemisphere of the Breit Frame (see Fig. 6.6). The Energy Flow Selection is designed to decrease these contributions to the event sample. The Energy Flow selection is made by creating a vector of the summed calorimeter cluster energy in the current hemisphere of the Breit Frame. The magnitude of that vector E_{BF} as a ratio to the Q can be plotted against the cosine of the polar angle of the vector ($\cos(\theta_{BF})$). From Fig. 6.1 it can be seen that the scattered quark in a QPM event will have energy $Q/2$ and a scattering angle (θ) of 180° ($\cos(\theta) = -1$). QPM type events are thus expected to cluster around the QPM point of Fig. 8.2 at (-1,0.5) whilst BGF events generally cluster in the lower right region. A simple geometric cut can be applied to remove the majority of BGF events. All events below the line joining the points (-1.0) and (0,0.5) can be removed; this cut is the Breit frame Energy Flow Selection (this Energy Flow Selection criterion appears as a line on the plane of Fig. 8.2) and is designed to produced an event sample with a higher purity of lowest order (more "e^+e^- like") events. There are fewer BGF events at high Q^2 so the Energy Flow Selection has less effect as Q^2 increases.

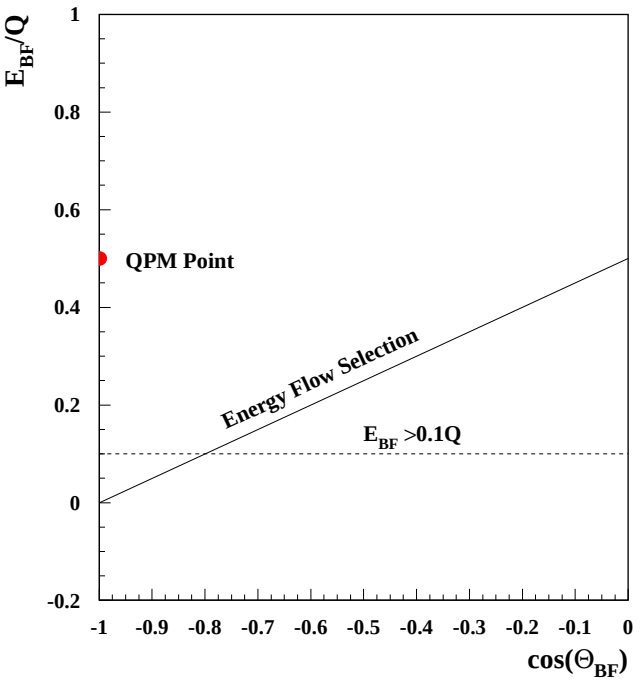

Figure 8.2: *The total summed calorimeter cluster four momentum vectors in the current ($z < 0$) hemisphere of the Breit Frame is plotted as a fraction of the event Q (E_{BF}/Q) against the cosine of the polar angle of the resultant vector ($\cos(\theta_{BF})$). The Breit frame energy flow selection is plotted as the solid line for comparison with the $E_{BF} > 0.1Q$ cut (dashed line).*

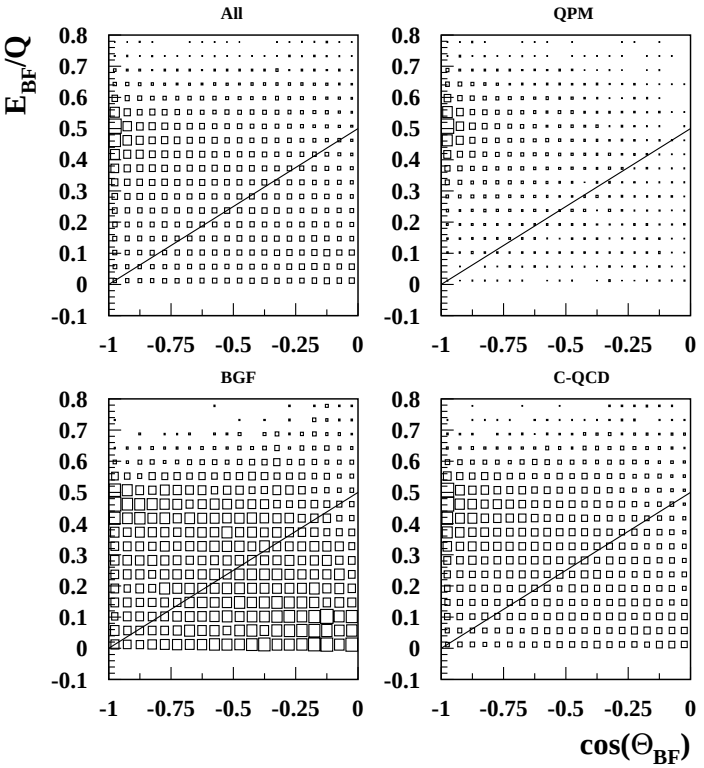

Figure 8.3: *The total summed calorimeter cluster four momentum vectors in the current ($z < 0$) hemisphere of the Breit Frame plotted as a fraction of the event Q (E_{BF}/Q) against the cosine of the polar angle of the resultant vector, $\cos(\theta_{BF})$, for low Q^2 reconstructed Monte Carlo. The distribution is also plotted for each of the different event types (QPM, BGF, and C–QCD).*

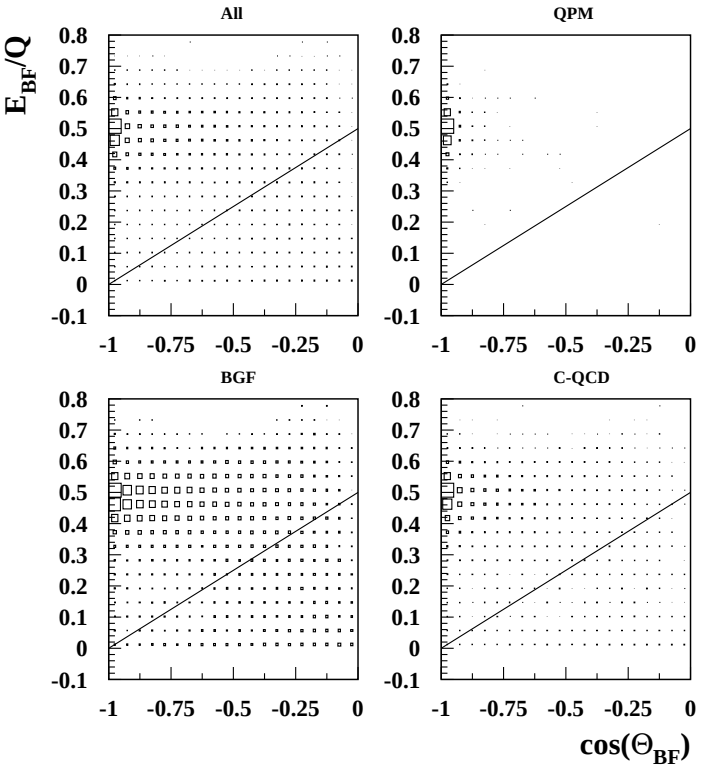

Figure 8.4: *The total summed calorimeter cluster four momentum vectors in the current ($z < 0$) hemisphere of the Breit Frame plotted as a fraction of the event Q (E_{BF}/Q) against the cosine of the polar angle of the resultant vector, $\cos(\theta_{BF})$, for high Q^2 reconstructed Monte Carlo. The distribution is also plotted for each of the different event types (QPM, BGF, and C–QCD).*

BGF events tend to cluster around the lower–right hand corner of Fig. 8.3, and generally have a more isotropic distribution than other DIS events because they are guaranteed two jets. BGF events thus tend to have a high $1 - T_z$ value and so the $E_{BF} > 0.1Q$ cut might bias the data sample to lower $1 - T_z$ values. To study this possibility the average $1 - T_z$ value was plotted as a function of E_{BF}/Q for uncorrected data (see Fig. 8.5).

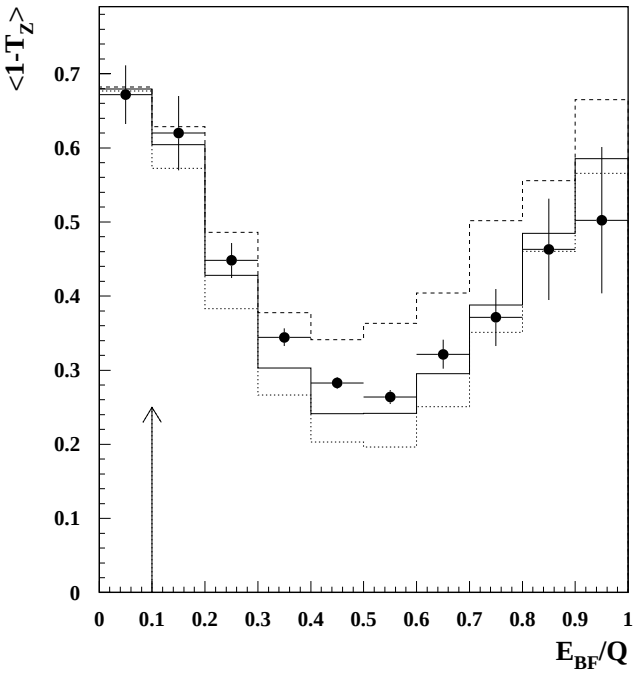

Figure 8.5: *The average thrust* $< 1 - T_z >$ *plotted as a function of the total summed calorimeter cluster four momentum vectors in the current* ($z < 0$) *hemisphere of the Breit Frame as a fraction of the event Q* (E_{BF}/Q). *The solid symbols are uncorrected 1996 high* Q^2 *data and the solid line is reconstructed MEAR Monte Carlo with a BGF fraction of* 32%, *the dashed line shows the MEAR Monte Carlo with only the BGF included (*100% *BGF) and the dotted line indicates the MEAR Monte Carlo with all the BGF events removed (*0% *BGF). The events to the left of the arrow are removed by the* $E_{BF} > 0.1Q$ *cut.*

The $E_{BF} > 0.1Q$ cut is removing events with a high $< 1-T_z >$ value (the $E_{BF} > 0.1Q$ cut is marked as an arrow in Fig. 8.5). This could bias the event sample to lower values of $< 1 - T_z >$. A correction factor for this cut could be calculated by varying the E_{BF}/Q cut and examining how the value of $< 1 - T_z >$ varies for the whole high Q^2 data sample. This is only done for the high Q^2 sample as the data in [52] is at high Q^2. It can be seen from Fig. 8.6 that the value of $< 1 - T_z >$ varies linearly with this E_{BF}/Q cut. A simple linear fit can be applied to the data to find the value of $< 1-T_z >$ when no E_{BF}/Q cut is

applied, this fit produces a value of $< 1 - T_z >= 0.346 \pm 0.002$ compared to 0.331 ± 0.003 when the $E_{BF} > 0.1Q$ cut was used. This means the values of $< 1 - T_z >$ in [52] should have been increased by 4% to account for the discussed bias. However, this will have little effect on the value for α_s in [52].

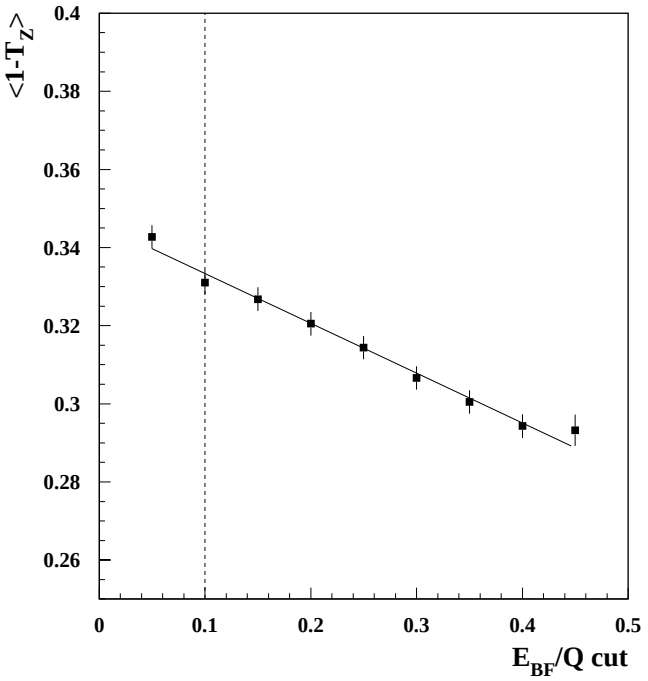

Figure 8.6: *The variation of* $< 1 - T_z >$ *with the applied* E_{BF}/Q *cut. The points are the high* Q^2 *data and the solid line is a simple linear fit. The dashed line indicates the position of the* $E_{BF} > 0.1Q$ *cut. Error bars are statistical and are point to point correlated as the spectrum is cumulative.*

8.3 BGF Proportion

The MEAR Monte Carlo prediction (solid line) in Fig. 8.5 appears to be systematically below the data. As T_z is sensitive to the proportion of BGF events an explanation for this discrepancy is that the BGF proportion within the Monte Carlo is not the same as in the data. It is possible to identify the different event types within the Monte Carlo in the following manner: if a parton entering the hard sub–process is a gluon the event is of a BGF type; if a gluon exits the hard sub–process the event is a C–QCD type event; if the partons entering and leaving the hard scatter are all quarks the event is a QPM type

event. Using this procedure the BGF events can either be removed completely from the simulated Monte Carlo sample (dotted line in Fig. 8.5) or all the other event types can be removed leaving just the BGF events (dashed line in Fig. 8.5). It is clear from Fig. 8.5 that neither of the extremes describes the data, but what proportion of BGF events best models the data? This question can be answered by weighting the BGF events in the Monte Carlo and using a fitting procedure to estimate which BGF proportion best fits the data.

If the different event types can be identified in the Monte Carlo it is trivial to calculate the BGF proportions in the Monte Carlo. The proportion of BGF events in the high (low) Q^2 MEAR Monte Carlo is 32% (44%). If the Monte Carlo is reweighted so that there is a BGF fraction of 60% and it is assumed that the $< 1 - T_z >$ versus E_{BF}/Q distribution varies linearly it is simple to perform a linear interpolation to estimate which BGF fraction best describes the data. This procedure uses a 1 parameter Minuit fit and can be applied over a number of x ranges for both the high and low Q^2 data to examine how the BGF fraction varies as a function of x. Tables 8.1 and 8.2 show the results of the fits for the high and low Q^2 data respectively. For comparison this process was repeated with the MEPS Monte Carlo (see Tables 8.3 and 8.4) and Fig. 8.7 shows the data using both Monte Carlos compared with generated values. It is clear from the plot that the BGF fraction in the two Monte Carlos disagree at high Q^2 (high x) resulting in different measured BGF fractions in the data. This problem may arise from the way BGF events are generated in the two Monte Carlos [53]. The BGF fractions for both Monte Carlos are generated as a function of the Mandelstam variable $\hat{s}$ ($\hat{s} = xs \simeq 2xk.P$) but the two Monte Carlos begin generating the BGF events at different $\hat{s}$ values resulting in the incompatible BGF fractions presented. Another potential problem is that the MEAR Monte Carlo generates the BGF events separately (see Chapter 3), this could lead to a wrong BGF proportion.

x bin	$\langle x \rangle$	BGF Fraction in Monte Carlo	BGF Fraction in Data and fitting error
All	0.0355 ± 0.0007	0.322 ± 0.004	0.54 ± 0.04
$0.0025 < x < 0.01$	0.00676 ± 0.00006	0.430 ± 0.008	0.58 ± 0.09
$0.01 < x < 0.025$	0.0164 ± 0.001	0.373 ± 0.007	0.52 ± 0.06
$0.025 < x < 1.0$	0.068 ± 0.001	0.229 ± 0.005	0.54 ± 0.07

Table 8.1: *The BGF proportions found in the MEAR Monte Carlo and the BGF proportions which best fit the data in a range of x bins for the high Q^2 samples.*

x bin	$\langle x \rangle$	BGF Fraction in Monte Carlo	BGF Fraction in Data and fitting error
All	0.00271 ± 0.0001	0.435 ± 0.004	0.41 ± 0.06
$0.0 < x < 0.00175$	0.001171 ± 0.000002	0.413 ± 0.006	0.37 ± 0.10
$0.00175 < x < 0.0025$	0.002087 ± 0.000003	0.449 ± 0.010	0.44 ± 0.11
$0.0025 < x < 1.0$	0.005091 ± 0.00002	0.458 ± 0.007	0.44 ± 0.07

Table 8.2: *The BGF proportions found in the MEAR Monte Carlo and the BGF proportions which best fit the data in a range of x bins for the low Q^2 samples.*

x bin	$\langle x \rangle$	BGF Fraction in Monte Carlo	BGF Fraction in Data and fitting error
All	0.0355 ± 0.0007	0.183 ± 0.003	0.22 ± 0.03
$0.0025 < x < 0.01$	0.00676 ± 0.00006	0.265 ± 0.007	0.35 ± 0.09
$0.01 < x < 0.025$	0.0164 ± 0.001	0.210 ± 0.006	0.24 ± 0.04
$0.025 < x < 1.0$	0.068 ± 0.001	0.115 ± 0.004	0.11 ± 0.05

Table 8.3: *The BGF proportions found in the MEPS Monte Carlo and the BGF proportions which best fit the data in a range of x bins for the high Q^2 samples.*

8.4 Discussion

The proportion of BGF events was found to be approximately 40% at low x but due to some problems it was not possible to predict the BGF proportion at high x. However, the BGF proportion is expected to decrease as x increases. Unfortunately this analysis suffers from a number of problems. The major drawback is that the work relies on the Monte Carlo for the definition of what constitutes a BGF event. This is compounded by the fact that different Monte Carlos begin generating BGF events in different regions of phase space and so produce different results for the final BGF proportions in the data. This problem probably stems from the value of $\hat{s}$ at which the Monte Carlos begin to generate the BGF events being different in the two Monte Carlos used. Other problems are thrown up by empty current hemisphere events, the value of T_z for events of this type is clearly undefined so they are simply ignored, in [52] the empty current hemisphere events are removed by the $E_{BF} > 0.1Q$ cut. The final problem involves the question of infra–red safety. The T_z is an infra–red safe variable since it integrates over low momentum contributions but it is not clear how ignoring the empty current hemisphere events may affect this and it is probable that the distribution as a function of E_{BF}/Q is not infra–red safe.

x bin	$\langle x \rangle$	BGF Fraction in Monte Carlo	BGF Fraction in Data and fitting error
All	0.00271 ± 0.0001	0.389 ± 0.007	0.38 ± 0.06
$0.0 < x < 0.00175$	0.001171 ± 0.000002	0.416 ± 0.010	0.42 ± 0.10
$0.00175 < x < 0.0025$	0.002087 ± 0.000003	0.427 ± 0.017	0.37 ± 0.14
$0.0025 < x < 1.0$	0.005091 ± 0.00002	0.335 ± 0.011	0.30 ± 0.09

Table 8.4: *The BGF proportions found in the MEPS Monte Carlo and the BGF proportions which best fit the data in a range of x bins for the low Q^2 samples.*

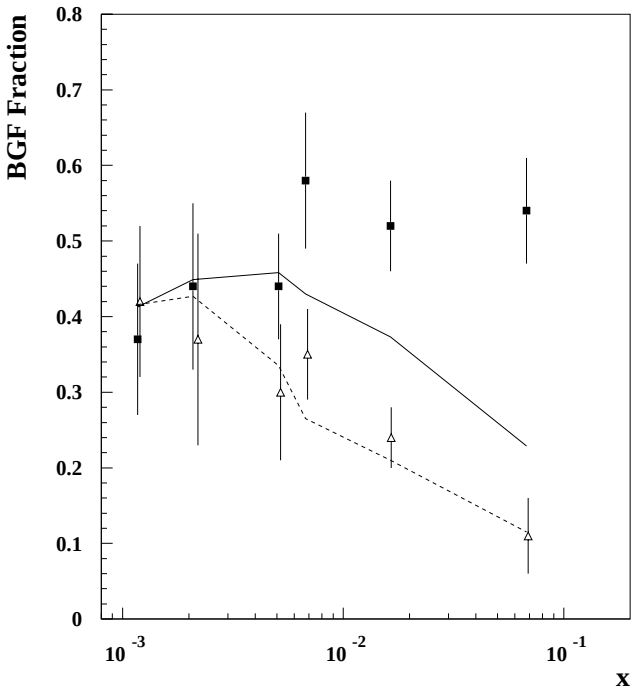

Figure 8.7: *The variation of the BGF fraction with x for the data using the MEAR Monte Carlo (solid points) and the MEPS Monte Carlo (open points) compared to the BGF fraction in the MEAR Monte Carlo (solid line) and the MEPS Monte Carlo (dashed line). The error bars arise from the error in the fitting procedure.*

Chapter 9

Fragmentation Spectra

9.1 Introduction

This chapter examines a number of fragmentation spectra in the Breit frame of reference. Rapidity distributions are shown over a range of p_t intervals. A search for the step in the rapidity spectrum, which was described in Chapter 6, is performed at low p_t. Models which behave like the BFKL and the DGLAP formalisms are compared to data at high p_t. Invariant energy spectra are also displayed along with MLLA/LPHD predictions. The invariant distributions are shown for low particle momenta and so are testing MLLA/LPHD down to very low energies.

In e^+e^- annihilation experiments, the momentum distribution of the hadrons scales with $\sqrt{s_{ee}} = E^*$, the centre of mass energy. In the past, e^+e^- experiments have used the scaled ratio of the momentum of any particular charged hadron to the maximum allowable energy ($x_p = 2p^{\pm}_{hadron}/E^*$) to describe hadronic spectra. When the current hemisphere of the Breit frame is compared to one hemisphere of an e^+e^- experiment the equivalent variable is $x_p = 2p^{\pm}_{hadron}/Q$. The distribution

$$D^{\pm}(x_p) = (1/N) \times dn^{\pm}_{tracks}/dx_p \tag{9.1}$$

is an event normalised charged track density, known as the fragmentation function (see Fig. 9.1). The fragmentation function rises steeply as x_p decreases and turns over in the region $x_p = 0$. If the fragmentation variable is changed to $\xi = \ln(1/x_p)$ then the turn over region is expanded (see Fig. 9.2). The Modified Leading Log approximation

(MLLA) to perturbative QCD predicts that for partons the ξ distribution should have an approximately Gaussian shape; Local Parton Hadron Duality (LPHD) suggests that the fragmentation function for hadrons should also be Gaussian. It is this Gaussian shape that has given the fragmentation function its other name of the "humped back plateau" [54]. The shape is a consequence of gluon coherence which suppresses wide angle soft gluon radiation. If gluon coherence did not occur the ξ distribution would have a shoulder in the low momentum (high ξ) region.

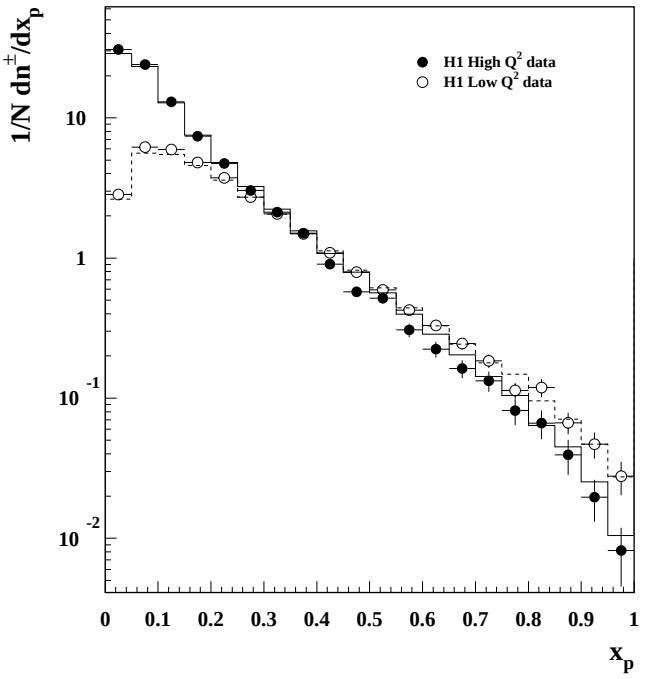

Figure 9.1: *The fragmentation function* $D(x_p) = (1/N)dn^{\pm}_{tracks}/dx_p$ *for the current hemisphere of the Breit frame. The open circles represent low* Q^2 *data and the solid circles high* Q^2 *data (statistical errors only). The lines are the expectation for the MEAR Monte Carlo.*

The evolution of the fragmentation function at low energies may be studied using the Lorentz invariant particle density [48], $(1/N_{evts}).Edn^{\pm}_{tracks}/d^3p$, which is related to the fragmentation function. The shape of the invariant distribution is sensitive to the running of the coupling constant α_s at small scales and, by comparison to e^+e^- experiments, can be used to confirm the universality of soft particle production. Perturbative QCD using the MLLA and LPHD predicts that hadronic spectra at low momentum should be independent of the parent parton. It was suggested in [55] that the comparison between a single hemisphere of e^+e^- and the current hemisphere of the Breit frame may be facilitated

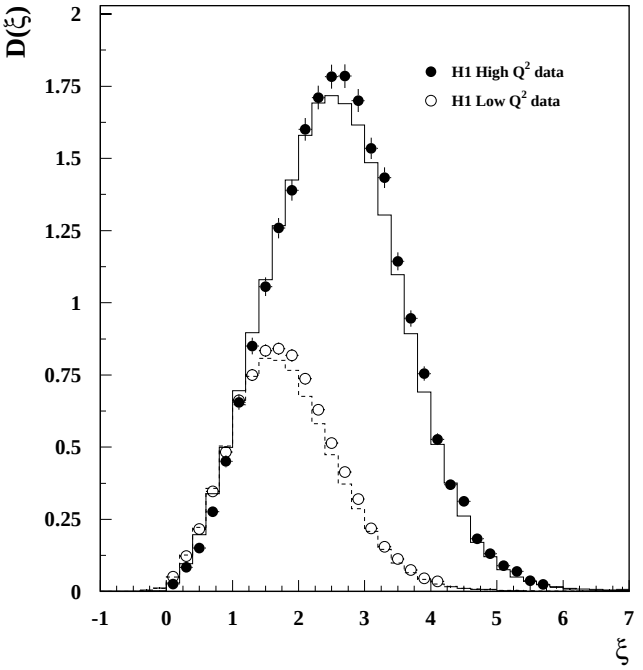

Figure 9.2: *The fragmentation function $D(\xi)$ for the current hemisphere of the Breit frame. The open circles represent low Q^2 data and the solid circles high Q^2 data (statistical errors only). The lines are the expectation for MEAR Monte Carlo.*

by examining the quantity dn/d^3p as a function of p. Again, Q is taken as being equivalent to the e^+e^- centre of mass energy, E^*.

As well as the above spectra this chapter also examines the behaviour of the rapidity and pseudo–rapidity plateaux as a function of transverse momentum. Certain theories [49] predict the formation of a plateau in the target hemisphere at low transverse momentum. The search for this plateau is detailed in this chapter. All of these analyses are performed in the Breit Frame of reference.

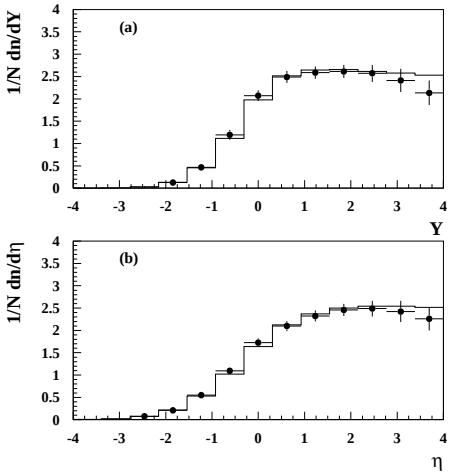

Figure 9.3: *(a) The corrected rapidity and (b) pseudo–rapidity plateaux produced by Low Q^2 H1 data (solid points), compared to generated Monte Carlo (solid line). The data were bin–by–bin corrected using the MEAR Monte Carlo. The error bars show the sum of statistical and relevant systematic errors in quadrature.*

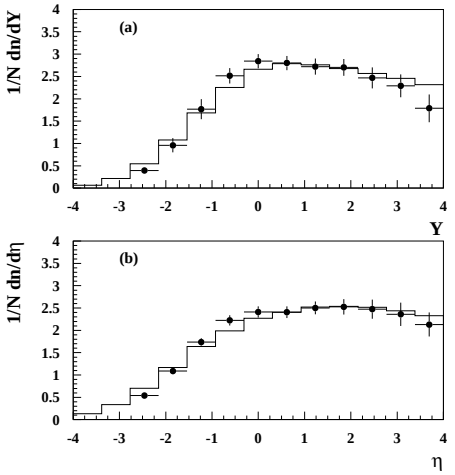

Figure 9.4: *(a) The corrected rapidity and (b) pseudo–rapidity plateaux produced by High Q^2 H1 data (solid points), compared to generated Monte Carlo (solid line). The data were bin–by–bin corrected using the MEAR Monte Carlo. The error bars show the sum of statistical and relevant systematic errors in quadrature.*

9.2 Rapidity Plateaux at Low p_t

The data were bin–by–bin corrected using the MEAR Monte Carlo. The correction factors are close to unity and smooth in the current region but increase significantly at higher Y values as the acceptance falls in the forward region. All plots in this analysis were normalised by the number of events (N) which passed the selection criteria discussed in Chapter 5. The corrected rapidity and pseudo–rapidity spectra can be seen in Figs. 9.3 and 9.4. The Monte Carlo (MEAR) describes the data well at both the reconstructed (not shown) and generated levels.

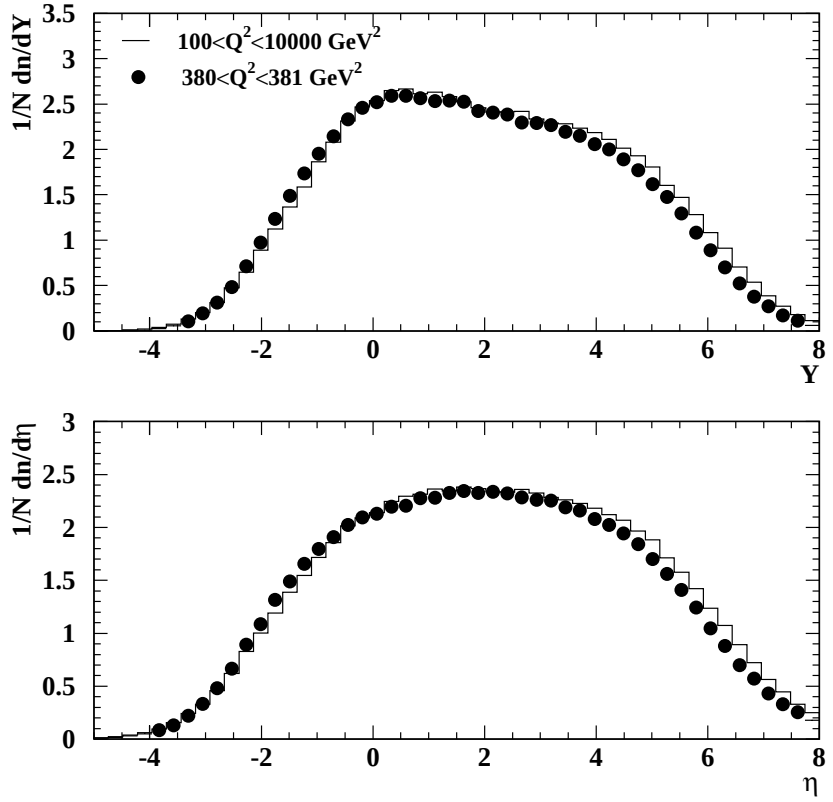

Figure 9.5: *The rapidity and pseudo–rapidity distributions generated over two Q^2 ranges but at the same average Q^2. The points were generated in the range* $380 < Q^2 < 381$ GeV^2 *and the line was generated in the* $100 < Q^2 < 10000$ GeV^2 *range by the MEAR Monte Carlo.*

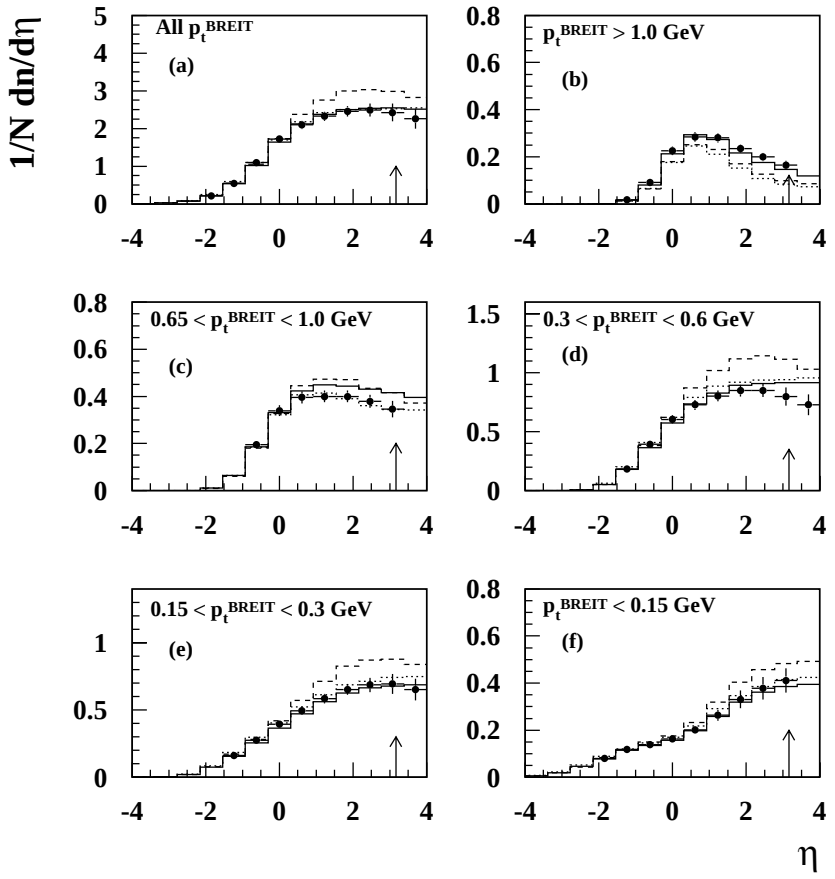

Figure 9.6: *The pseudo–rapidity distributions for (a) all charged tracks, and (b–f) for five indicated intervals of track transverse momentum, p_t^{BREIT}, in the Breit frame, all at low Q^2. The error bars show the sum of statistical and relevant systematic errors in quadrature. The arrow indicates the position of the origin of the hadronic centre of mass system for $< Q >$ (5 GeV) of the data. The histograms show the predictions of LO QCD Monte Carlo models, the solid line utilising a colour dipole fragmentation (MEAR), the dashed (dotted) lines utilising a parton shower with (without) soft colour interaction effects (MEPS).*

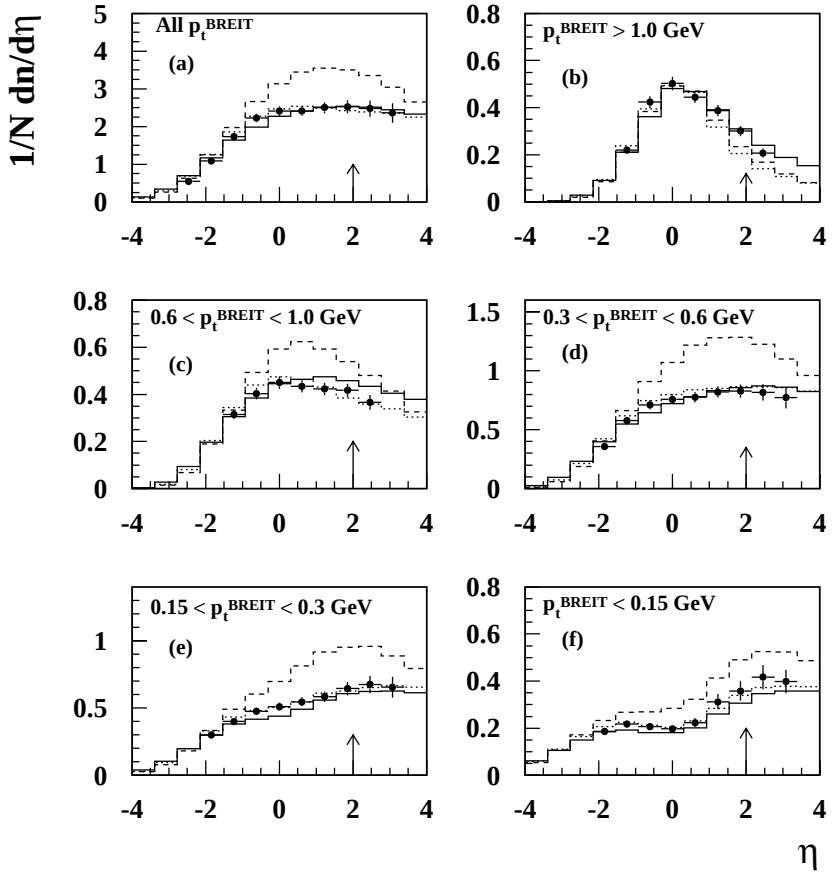

Figure 9.7: *The pseudo–rapidity distributions for (a) all charged tracks, and (b–f) for five indicated intervals of track transverse momentum, p_t^{BREIT}, in the Breit frame, all at high Q^2. The error bars show the sum of statistical and relevant systematic errors in quadrature. The arrow indicates the position of the origin of the hadronic centre of mass system for $< Q >$ (23 GeV) of the data. The histograms show the predictions of LO QCD Monte Carlo models, the solid line utilising a colour dipole fragmentation (MEAR), the dashed (dotted) lines utilising a parton shower with (without) soft colour interaction effects (MEPS).*

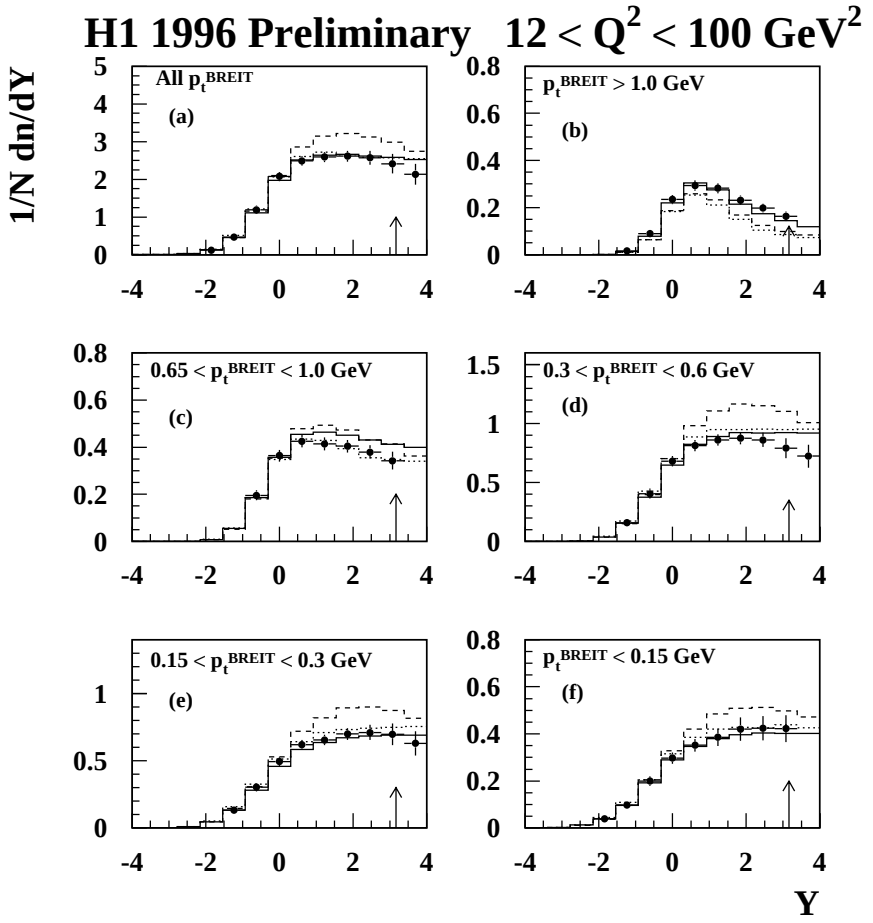

Figure 9.8: *The rapidity distributions for (a) all charged tracks, and (b–f) for five indicated intervals of track transverse momentum, p_t^{BREIT}, in the Breit frame, all at low Q^2. The error bars show the sum of statistical and relevant systematic errors in quadrature. The arrow indicates the position of the origin of the hadronic centre of mass system for $< Q >$ (5 GeV) of the data. The histograms show the predictions of LO QCD Monte Carlo models, the solid line utilising a colour dipole fragmentation (MEAR), the dashed (dotted) lines utilising a parton shower with (without) soft colour interaction effects (MEPS).*

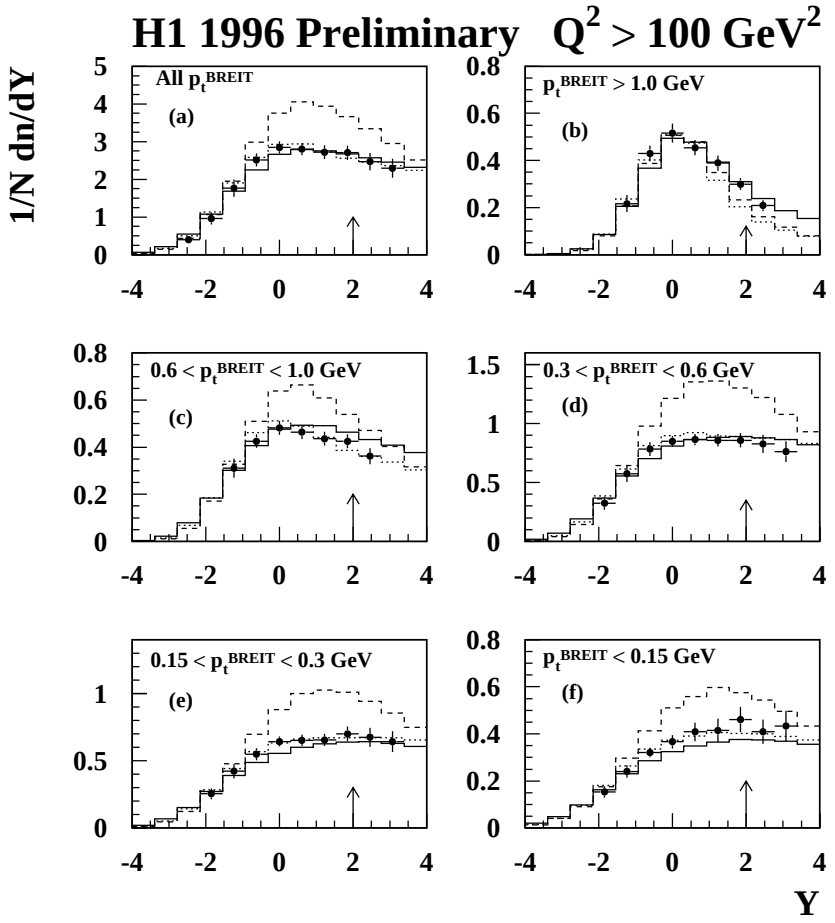

Figure 9.9: *The rapidity distributions for (a) all charged tracks, and (b–f) for five indicated intervals of track transverse momentum, p_t^{BREIT}, in the Breit frame, all at high Q^2. The error bars show the sum of statistical and relevant systematic errors in quadrature. The arrow indicates the position of the origin of the hadronic centre of mass system for $< Q >$ (23 GeV) of the data. The histograms show the predictions of LO QCD Monte Carlo models, the solid line utilising a colour dipole fragmentation (MEAR), the dashed (dotted) lines utilising a parton shower with (without) soft colour interaction effects (MEPS).*

The difference between the gentle rise of Fig. 9.4 (over $\Delta Y \approx 4$ units) and the steep prediction of the Feynman model [23] ($\Delta Y \approx 1$ to 2 units) was first thought to be caused by a smearing out of the rapidity distribution by the large Q^2 interval used in this analysis. This idea was tested by generating a rapidity distribution over a very wide Q^2 and comparing it to a rapidity distribution generated over a narrow range in Q^2 but at the same average Q^2. It can be seen in Fig. 9.5 that the resulting distributions lie on top of each other for both Y and η, so significant smearing does not occur. Possible other causes of the slow rise were investigated. The most likely explanation is the dominance of leading order diagrams (particularly BGF) causing the jet(s) in the current hemisphere to become non–aligned with the thrust axis (z–axis) in turn producing the observed slow rise. Fig. 9.5 can be compared with Fig. 6.2. The average value of W in Fig. 9.5 is approximately 135 GeV which gives a prediction for the full width of the plateau as 13.5 (using $\Delta Y = 2\ln(W/m)$ and taking m as the mass of the pion) which is slightly larger, but still in agreement with the observed width. The distributions do not have the same $\langle W \rangle$, hence the marginal differences in width. This is all purely kinematics but it is a useful check to see if the plateaux are behaving as expected.

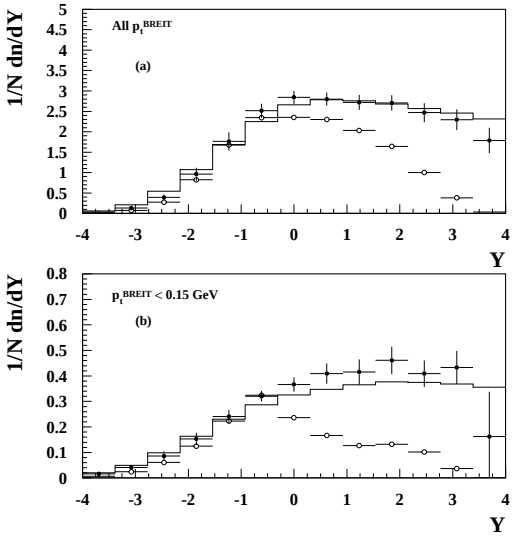

Figure 9.10: *The rapidity distributions for (a) all tracks and (b) tracks with $p_t < 0.15$ GeV. The solid points are corrected data, the open points are uncorrected data and the line is the generated MEAR Monte Carlo*

The shape of the rapidity plateau changes with the transverse momentum (p_t) of the particles. This is shown in Figs. 9.6–9.9 for Y and η at high and low Q^2 respectively. For all of these plots only the bins with acceptance greater than 20% and purity greater than

35% are shown. As the lower limit in p_t^{BREIT} decreases there is a loss of acceptance. This is due to the design of the H1 tracking system and the applied track selection cuts. The H1 tracking system is divided into a forward and a central tracker. Although the position of the forward tracker is not well defined in rapidity in the Breit frame, the rear edge of the forward tracker is generally greater than $\eta = 1.0$ and the forward face of the central tracker is usually below $\eta = 1.5$. Tracks have a cut placed on them to remove the low transverse momentum tracks that curl up in the beam pipe and are hence unmeasured or that lose energy in the beam pipe material. This cut removes tracks with $p_t^{LAB} < 0.15$ GeV. As there is a correlation between p_t^{LAB} and p_t^{BREIT} (Fig. 6.4), tracks with a low p_t^{BREIT} will be removed; this loss becomes greater as p_t^{BREIT} becomes smaller, as may be seen by the difference between the corrected and the uncorrected data in Fig. 9.10.

At low p_t^{BREIT} a second step in the pseudo–rapidity distribution becomes visible. In Figs. 9.6 and 9.7 there is a flattening of the distribution around $\eta = -1.0$. At low p_t ($p_t \sim m_\pi$) the approximation of η for rapidity becomes unsafe and the low p_t^{BREIT} tracks in the $Y = 0$ region have higher $|\eta|$ values causing a flattening. This secondary plateau is *not* the current plateau predicted in some theories [49] but an artifact of pseudo–rapidity. In fact the step is even evident in the Monte Carlo which is leading order and so would not be expected to reproduce this higher order structure. The step does not occur in the Y distributions (see Figs. 9.8 and 9.9). Indeed for Y, a flat plateau is evident at low p_t as predicted by Bjorken [15] and Feynman [23] using the simple parton model. As Q^2 increases the current hemisphere (negative Y) extends as $\ln Q$, and as p_t increases QCD evolves the flat plateau into an almost Gaussian shape peaking near zero, thus displaying the special role of the Breit frame. The hadronic centre of mass frame is colinear with the Breit frame so the two origins are displaced by a constant amount which can be calculated from the average values of the kinematic quantities; the position of the origin of the hadronic centre of mass is marked on each of the plots by a small arrow. For rapidity there is no evidence for the step predicted in [49] in any p_t^{BREIT} range, assuming that the size of the step is significantly greater than the bin width in Y (0.6).

In Deep Inelastic Scattering there is a class of events that do not produce energy flow between the proton remnant and the scattered quark. These diffractive or rapidity gap processes are governed by a colourless exchange, the 'pomeron', between the proton and the virtual photon. Diffractive processes are not described well by Monte Carlos. As an attempt to remedy this the MEPS Monte Carlo can be implemented with 'Soft Colour Interactions', which are intended to model diffractive events as a natural result of final state parton interactions. It can be seen in Figs. 9.6–9.9 that the soft colour interactions

predict much too large multiplicities in the target hemisphere particularly at high Q^2 and intermediate p_t. On the other hand, the Colour Dipole Model (MEAR) models the data very well in all p_t regions and the parton shower model (MEPS) without SCI describes the data fairly well but shows a deficiency of high p_t tracks in the target hemisphere for low Q^2 events. The CDM is like the BFKL model in that it does not have strong ordering in k_T while MEPS behaves more like the DGLAP formalism. This result agrees with previous work [57] in finding that a BFKL type model (CDM) gives better agreement with the data at high p_t.

Figs. 9.8 and 9.9 show rapidity spectra at low and high Q^2 respectively. For ease of comparison the two figures have the same vertical scales. It is noticeable that the increase in the charged track multiplicity in the high Q^2 sample (Fig. 9.8a peaks at about 2.6 while Fig. 9.9a peaks at around 3.0) is produced predominantly by high p_t tracks.

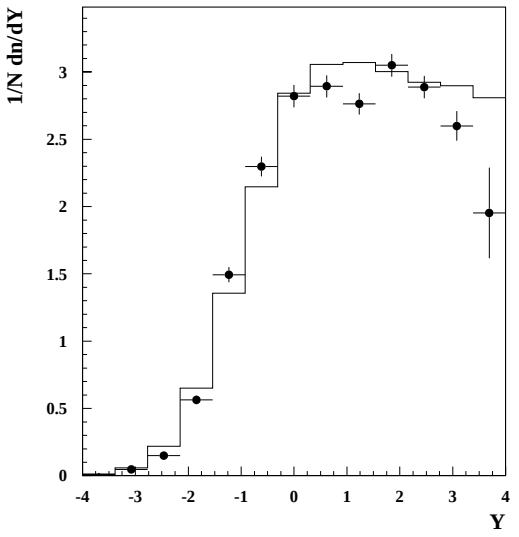

Figure 9.11: *The rapidity distributions for events at low x ($x < 0.01$) and high Q^2. The data are the points and the line is the MEAR Monte Carlo (statistical errors only).*

If the step in the current hemisphere is created by the ladder type Feynman diagram (Fig. 6.4) then cuts can be applied which favour this type of event, and the current step should then be enhanced. A number of tests were carried out to try and produce events which are dominated by the ladder diagram. These tests will be detailed next. Gluons inside the proton tend to carry a small fraction x of the proton's 4–momentum. The gluon ladder type of event generally has a low x value. A cut on the x variable should enhance the current step signal. This turns out not to be the case; the rapidity distributions at

low x (Fig. 9.11 for $x < 0.01$) are very similar to those in Fig. 9.4.

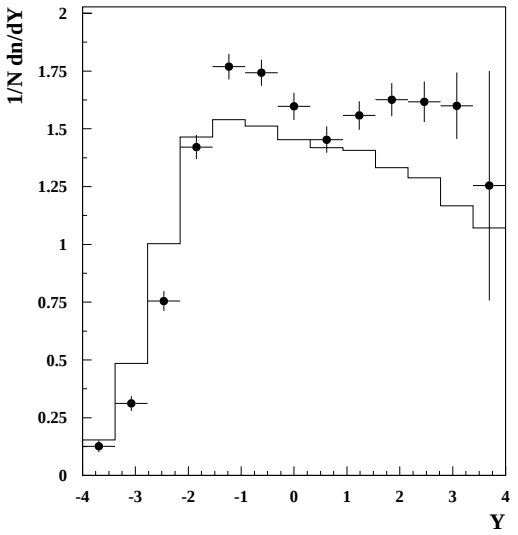

Figure 9.12: *The rapidity distributions for events with a low event p_T and high Q^2 - ($\Sigma_{clusters}|p_T^{Breit}| < 10.0$ GeV). The points are corrected data and the line is the MEAR Monte Carlo (statistical errors only).*

The proposed reason for the slow fall–off of the rapidity distributions, compared to the simple Feynman picture, is the leading order (BGF) events causing the current jet to be misaligned with the thrust axis [58]. To avoid such events one could either make a selection for jets which have a smaller angle with respect to the beams, or equivalently, calculate the $|p_T|$ of the *event* in the Breit frame and select those events with a low event p_T. It was thought that the low event p_T method was the most bias free method of examining the behaviour of the slow current fall–off. The low p_T events are selected by summing the p_t of the calorimeter clusters in the Breit frame and imposing $\Sigma_{clusters}|p_T^{Breit}| < 10.0$ GeV. As can be seen in Fig. 9.12 the rapidity distribution for low p_T events has a different shape and the Monte Carlo does not describe the data. There is a sharp rise in the current hemisphere and the target plateau is not quite as high as in Fig. 9.4. The low event p_T cut is effectively selecting QPM type events. The peak at negative Y is created by the struck quark which goes into the current hemisphere close to the thrust axis, so total p_T is kept low. Simple QPM type events will generally have less energy flow in the target region, due to the lack of gluonic radiation, and so the height of the plateau in this area is reduced.

The predicted step in the rapidity distribution between the current and target regions

is created by different rates of gluon radiation in those regions. The gluons would be of low momentum so the hadrons produced from them would also be soft. To select these predominately gluonic events a cut could be placed to limit the maximum transverse momentum of the tracks in an event, so an event would only be selected if the maximum track momentum was below an arbitrary value ($p_t^{MAX} < 2.5$ GeV). In addition a large number of the soft gluons would be expected so the overall event p_T would be large ($\Sigma_{clusters}|p_T^{Breit}| > 20.0$ GeV). Fig. 9.13 shows the rapidity distribution with both these conditions imposed, again there is no evidence of a step in the current region.

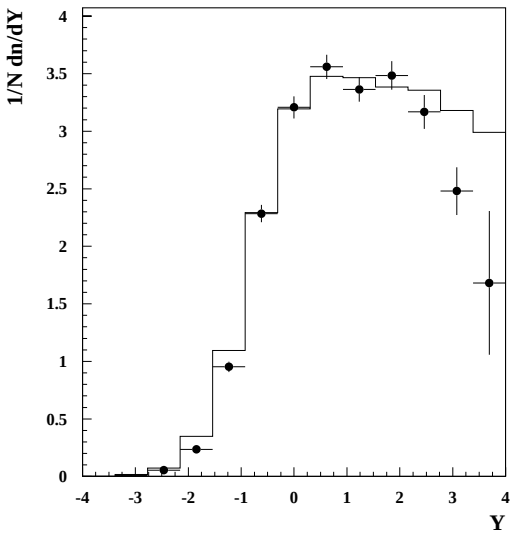

Figure 9.13: *The rapidity distributions for events with a high event p_T ($\Sigma_{clusters}|p_T^{Breit}| > 20.0$ GeV) but a low maximum track p_t ($p_t^{MAX} < 2.5$ GeV). The points are corrected data and the line is the MEAR Monte Carlo (statistical errors only).*

The Monte Carlo used in this analysis only generates events up to leading order (LO) in QCD. Although the ladder type diagram, which theoretically produces the current plateau, is of a higher order it does share one feature with LO Boson–Gluon fusion (BGF) events in that both of these event types have a quark "box" connecting the gluon string to the virtual photon. The major difference between the BGF events and the ladder diagram is that the BGF events do not have the gluon radiation in the target region. Each LO event type can be identified at the generated level in the Monte Carlo, so the spectra for each event type can be obtained (see Fig. 9.14). Fig. 9.14a is essentially the same as Fig. 9.4. The rapidity distribution for QPM events is shown in Fig. 9.14b. The structure and peak height in this figure is similar to Fig. 9.12 and again shows evidence for the backward going quark jet quite clearly. The last two figures for BGF and Compton QCD (C–QCD)

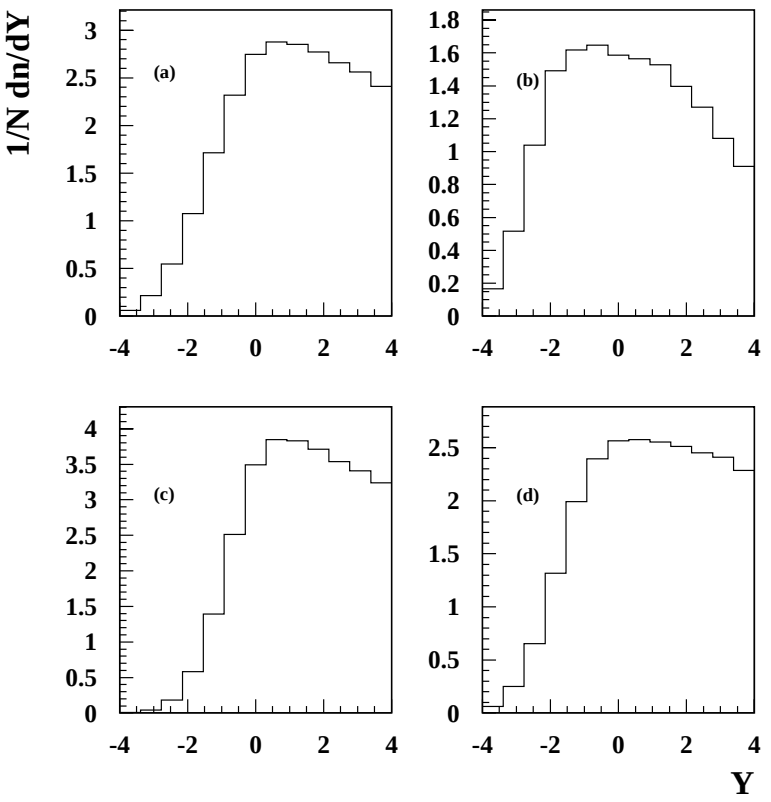

Figure 9.14: *The rapidity distributions for differently generated high Q^2 Monte Carlo (MEPS) zeroth and leading order event types. (a) All events (b) quark–parton model (QPM) events (c) boson–gluon fusion (BGF) events and (d) Compton–QCD (C–QCD) events.*

type events (Fig. 9.14c and Fig. 9.14d) have the same shape as the inclusive histogram, although the BGF distribution does fall off slightly faster in the current hemisphere. This suggests that the quarks produced in the quark box of the BGF diagram generally go into the target region and not the current region. The prediction, made in [49], of the step in the current hemisphere is based on the assumption that the particles produced in the region of the quark box of the Feynman diagram go into the current region of the Breit frame. This assumption is wrong and that is the reason why the step in the current region is not observed.

The differential Y-p_t distributions (dn/dYd^2p_t) can be plotted on a logarithmic scale versus Y in bins of p_t (Fig. 9.15) and against p_t^2 in Y intervals (Fig. 9.16). I use the nomenclature of [55] and dn/dYd^2p_t should be interpreted as the number density of

charged tracks in a given Y, p_x, p_y interval and is equal to $dn/2\pi p_t dY dp_t$ assuming azimuthal symmetry. Fig. 9.16 has had bins of $Y < -2.5$ removed as the purity in that region is poor. The differential distributions are related to both the rapidity distributions and the invariant spectra (see the next section).

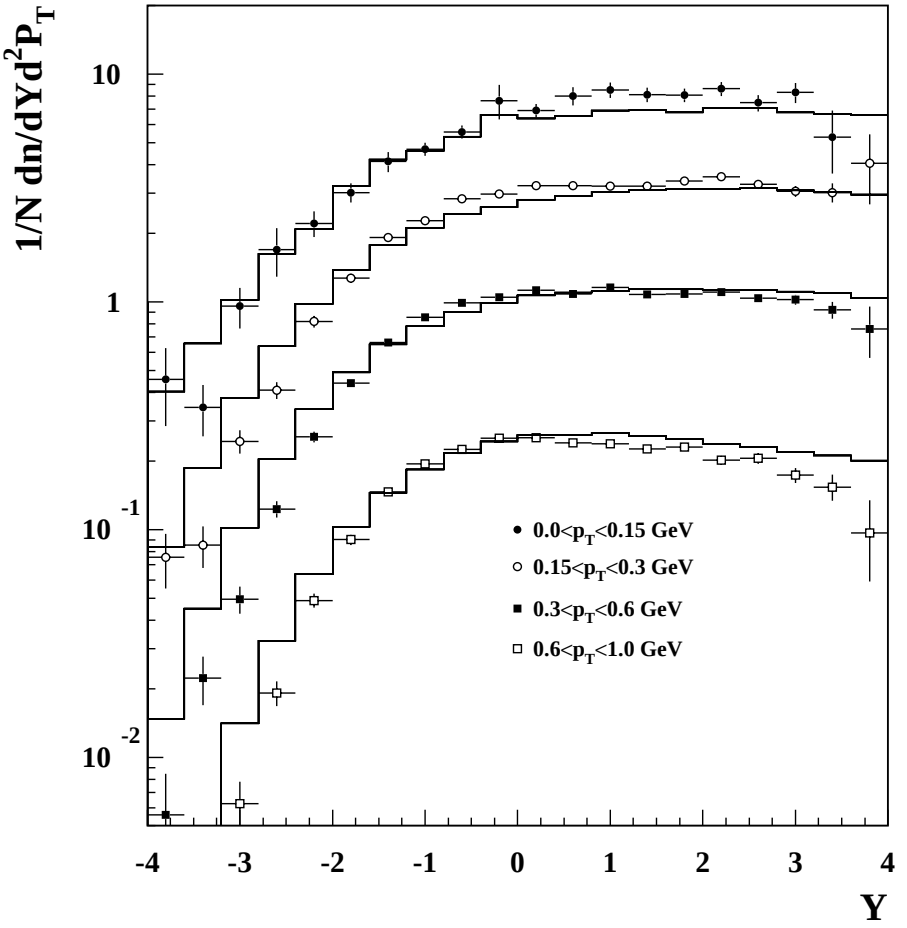

Figure 9.15: *$dn/dY d^2p_t$ versus Y in a range of p_t intervals for high Q^2 1996 data (points) and the MEAR Monte Carlo (solid line) . Statistical errors only.*

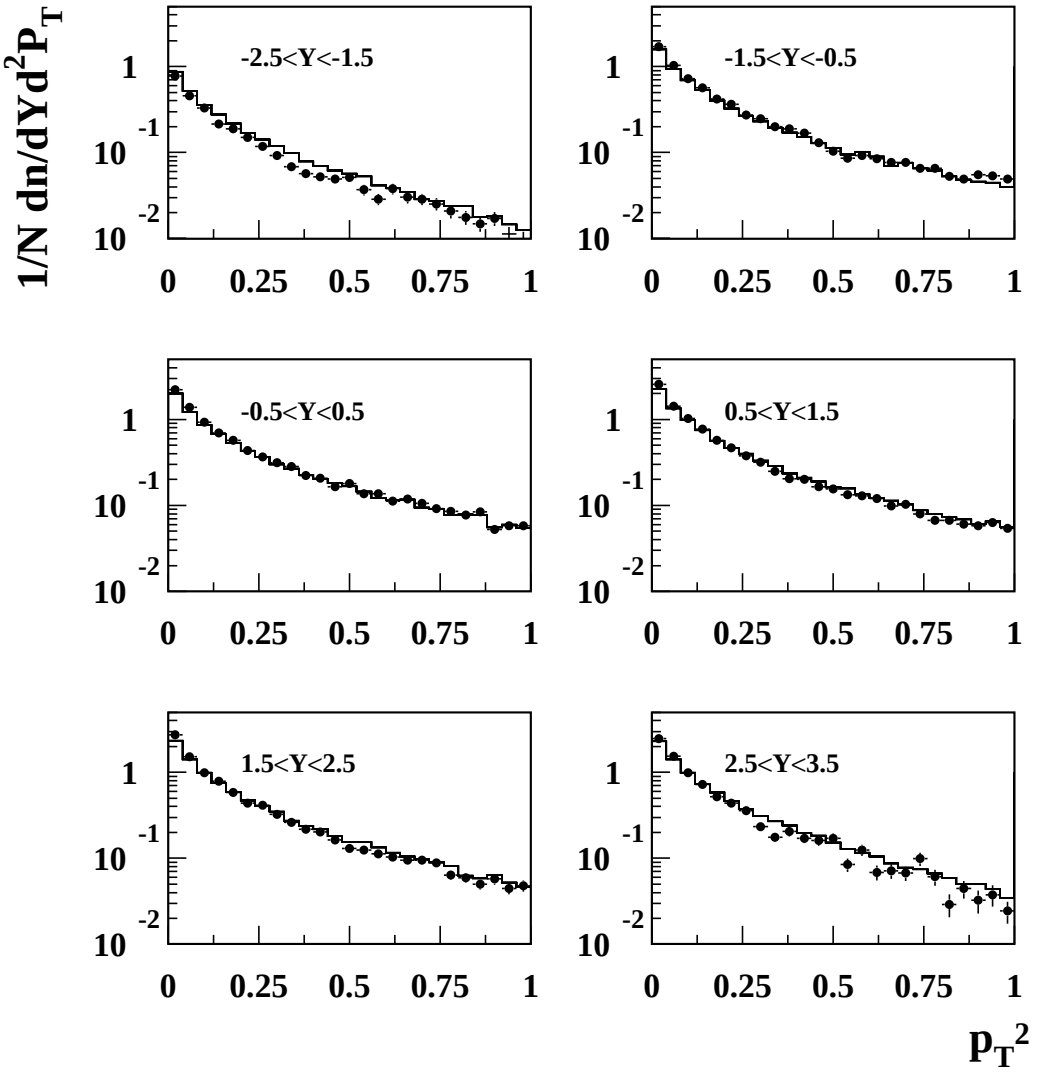

Figure 9.16: *dn/dYd^2p_t versus p_t^2 in a range of Y intervals for high Q^2 1996 data (points) and the MEAR Monte Carlo (solid line). Statistical errors only.*

9.3 Invariant Energy Spectra

The invariant energy density can be used to test the universality of soft particle production by comparing the distributions produced from one hemisphere of an e^+e^- experiment to the current hemisphere of the Breit frame. The invariant energy density is defined as Edn/d^3p, where p is the momentum of each charged track and E is the energy. In [55] E is computed as if the hadron had a mass of Q_0 (=270 MeV$\approx \Lambda_{QCD}$) which is the cut–off mass of the parton shower, so that the energy of each track is $E = \sqrt{Q_0^2 + p_{hadron}^2}$. The invariant distributions for the low and high Q^2 1996 data are given in Fig. 9.17, where $d^3p = 4\pi p_{hadron}^2 dp_{hadron}$ has been taken and the data is compared with MLLA/LPHD predictions at the same $\langle Q \rangle$ values for quark fragmentation (e^+e^-). These are the calculations of [48] which the authors show are in agreement with e^+e^- data. The MLLA/LPHD predictions are very sensitive to the running of the strong coupling constant, α_s, as the energy scale alters in the parton shower. Fig. 9.17 shows a prediction utilising a fixed value of α_s (set to 0.215 [59]) and normalised to $\langle n^{\pm} \rangle$ multiplicities in e^+e^- experiments. This fixed α_s prediction clearly does not describe the data. Unfortunately the MLLA/LPHD predictions are only in leading order so this cannot be turned around to calculate a value of $\Lambda_{\rm QCD}$. The discrepancies visible at low Q^2 are related to the contributions of leading order, particularly boson–gluon fusion, diagrams that are neither present in the MLLA/LPHD calculations nor in e^+e^- data [60] and [61]. BGF events along with initial state C–QCD (which do occur in e^+e^- experiments) can de–populate the current hemisphere of the Breit frame. If the energy flow selection is applied (see Chapter 8; solid circles in Fig. 9.17) the low Q^2 data rise towards the prediction but the high Q^2 are hardly affected (the energy flow selected data sits on top of the unselected data), thus further illustrating that low Q^2 data has a higher BGF fraction than the high Q^2 data.

The invariant distributions can be compared to the double differential rapidity plateaux from the previous section. As shown in [55]

$$\lim_{p_t \to 0, Y \to 0} \frac{dn}{dY d^2 p_t} \simeq \lim_{p \to 0} E \frac{dn}{d^3 p} \tag{9.2}$$

This behaviour should hold approximately for p_t not much larger than the particle masses ($\approx Q_0$). The value of $\frac{dn}{dY d^2 p_t}$ (Fig. 9.15) as $p_t \to 0$ and $Y \to 0$ is approximately 6–8 GeV^{-2} which agrees reasonably well with the high Q^2 invariant distribution $E\frac{dn}{d^3p}$ (Fig. 9.17b) as $p \to 0$ ($E \to Q_0 = 270$ MeV) , thus supporting equation 9.2.

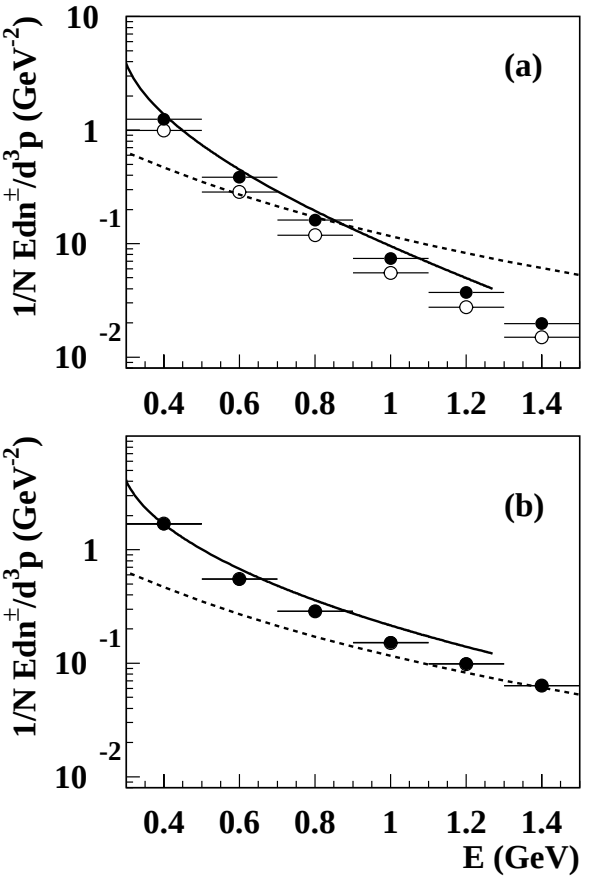

Figure 9.17: *The invariant charged hadron energy spectrum in the current hemisphere for (a) low Q^2 data and (b) high Q^2 data. The solid lines show the MLLA/LPHD prediction calculated at $\langle Q \rangle$ for each data set. The dashed lines show a prediction using a fixed value of α_s. The open circles are for the entire data sample and the solid circles are the data after the energy flow selection has been applied. In the high Q^2 sample the energy flow selected data sits on top of the unselected data.*

In Fig. 9.18 the data are divided into twelve intervals of Q^2 and only the regions which have a purity greater than 40% are shown. There is an incremental spacing between each of the spectra of 0.5 GeV on the abscissa. The MLLA/LPHD predictions become unreliable as E increases so the most important data points are those at low E (the uppermost points for each Q^2 interval). Again a discrepancy between the data and the MLLA/LPHD prediction is visible at low Q^2 (the energy flow selection has not been applied). As Q^2 increases the data approach the prediction. This again suggests that BGF events, that reduce the multiplicity in the current hemisphere, are less common at high Q^2. At higher Q^2 values, data show a clear trend to approach a common limit at low energy (E), independent of Q^2, in agreement with the theoretical predictions.

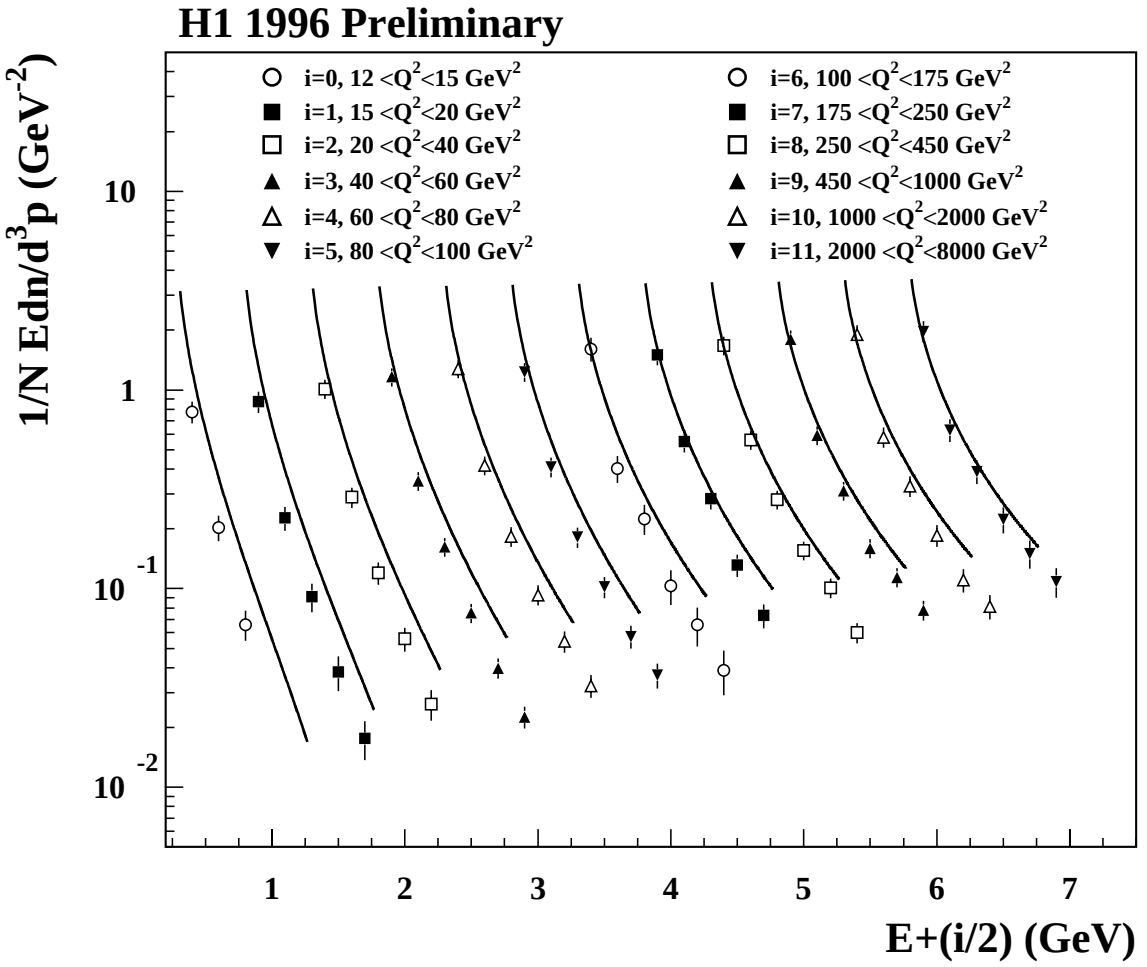

Figure 9.18: *The invariant charged hadron energy spectrum (Edn/d^3p) in the current hemisphere in twelve intervals of Q^2, with a regular incremental spacing of 0.5 GeV on the abscissa. The solid lines show the prediction of MLLA/LPHD calculated at the $\langle Q \rangle$ for each distribution. The error bars show the sum of statistical and systematic errors added in quadrature.*

To facilitate the comparison between a single hemisphere of e^+e^- and the current hemisphere of the Breit frame it was suggested in [55] that the quantity dn/d^3p be examined as a function of p. This quantity behaves in a similar way to the invariant energy spectrum (Edn/d^3p), but independent of any mass assumption. Again the prediction becomes unreliable as p grows so the low p points should be concentrated on. The data again approach the MLLA/LPHD prediction made for e^+e^- as scale energy (Q^2) increases (see Fig. 9.19). These are important results as they show that MLLA/LPHD works down to very low energies.

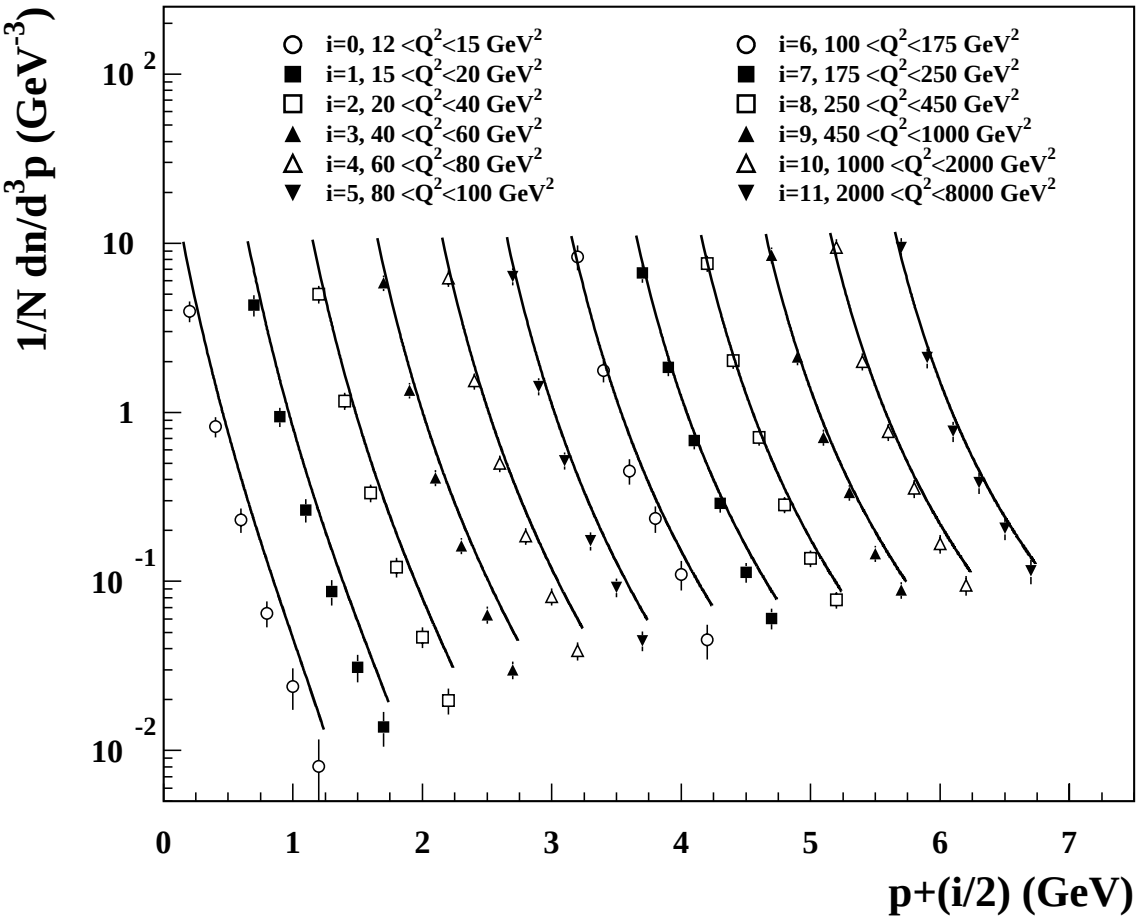

Figure 9.19: *The invariant charged hadron spectrum (dn/d^3p) in the current hemisphere in twelve intervals of Q^2, with a regular incremental spacing of 0.5 GeV on the abscissa. The solid lines show the prediction of MLLA/LPHD calculated at the $\langle Q \rangle$ for each distribution.*

9.4 Systematic Uncertainties

Systematic errors from the following sources were considered:

- the particular Monte Carlo model used in acceptance correction of the data;
- the electromagnetic energy scale (calibration) of the LAr and SpaCal calorimeters;
- the uncertainty associated with the modelling of secondary particle production in the forward tracker;
- the efficiency of the track reconstruction code;
- an acceptance asymmetry in the Central jet chambers (CJC) of the Central track detector.

9.4.1 Monte Carlo Acceptance Correction

The MEAR Monte Carlo was used for all acceptance correction within this analysis. To account for the uncertainty in this procedure the correction factors from MEAR were compared to those from the MEPS Monte Carlo and the difference between the two results was interpreted as the error for each bin.

9.4.2 Electromagnetic Energy Scale

In this analysis the kinematic variables are determined from the scattered electron, therefore a mismeasurement of the electron energy directly affects the boost to the Breit frame. There is an uncertainty on the energy scale of both calorimeters, $\pm 1\%$ for SpaCal and $\pm 3\%$ for the Liquid Argon calorimeter. This systematic error produces forward–backward (interpreted conservatively as a point to point) uncertainty in the rapidity plateaux and a 9% error on the overall multiplicity in the current hemisphere on the Breit frame for both the high and low Q^2, which is included in the invariant distributions.

9.4.3 Forward Tracker

A particle that enters the forward track detector has to pass through a large amount of dead material first. This large amount of dead material can cause the production of secondary particles, which are difficult to model with Monte Carlo. A 10% systematic has been placed on the number of all forward tracks and then scaled proportionately for the content of each bin [62].

9.4.4 Track Reconstruction Efficiency

A visual scan of typical DIS events reveals that some obvious tracks produced in the detector are not reproduced by the reconstruction software. This track reconstruction inefficiency is below the 5% level. On the other hand, it has been argued that the reconstruction software is more sensitive (μm level) than the human eye (mm level) at determining what is a valid track. A $\pm 5\%$ error is applied to all track numbers to account for possible track reconstruction uncertainty as well as the CJC asymmetry (see next section).

9.4.5 CJC Asymmetry

During the 1996 and 1997 run periods it was noticed that signal response in the lower half of the CJC slowly decreased with time. The Monte Carlo modelling of this effect was not perfect so a systematic error is applied to the data to allow for this, found by comparing numbers of tracks with vertical up and down components of laboratory momentum. A 5% error is applied to all numbers of tracks to account for this CJC asymmetry and the uncertainty in the track reconstruction efficiency.

9.4.6 Error Summary

Combined systematic errors are greater than statistical errors in all the bins of the rapidity analysis and they dominate in the forward direction. For the invariant spectra analysis the systematic and statistical errors are more comparable but the systematic errors grow with Q^2.

9.5 Summary

Local parton hadron duality coupled with the modified leading logarithm approximation predict the formation of a plateau in the current region of the Breit frame at low p_t. The ratio of colour charge between the quark box and the gluon radiation in a ladder type Feynman diagram suggests the ratio of the height of the plateau in the target region to the height of the current plateau to be approximately 9/4. Despite using a variety of cuts, no evidence for the existence of such a current plateau was found. A possible explanation for the lack of a current plateau is that the particles produced from the quark box in the ladder diagram do not always travel into the current hemisphere but go into the target region where they contaminate the gluon radiation from other events. At high p_t the data favour a model which behaves like the BFKL formalism (CDM) rather than the DGLAP formalism (MEPS).

Invariant distributions have been examined over a range of Q^2. Agreement with MLLA/ LPHD predictions is observed as the energy scale (Q^2) increases. The discrepancy between the data and the prediction, which is more evident at low Q^2, can be attributed to the leading order events which are not present in e^+e^- physics or the prediction. These events, particularly BGF events, generally have a lower multiplicity in the current hemisphere of the Breit frame resulting in a lower value of Edn/d^3p. The agreement shows that MLLA/LPHD works down to very low energies.

Y Range	$1/N\ dn/dY$		
	No p_t Cut	$p_t > 1.0$ GeV	$0.6 < p_t < 1.0$ GeV
$-4.0 < Y < -3.38$	0.0003 ± 0.0003	–	–
$-3.38 < Y < -2.77$	0.003 ± 0.002	–	–
$-2.77 < Y < -2.15$	0.025 ± 0.006	–	0.0002 ± 0.0001
$-2.15 < Y < -1.54$	0.13 ± 0.02	0.0007 ± 0.0009	0.007 ± 0.003
$-1.54 < Y < -0.92$	0.47 ± 0.06	0.016 ± 0.005	0.06 ± 0.01
$-0.92 < Y < -0.31$	1.19 ± 0.11	0.09 ± 0.01	0.20 ± 0.02
$-0.31 < Y < 0.31$	2.07 ± 0.12	0.23 ± 0.02	0.36 ± 0.02
$0.31 < Y < 0.92$	2.49 ± 0.13	0.29 ± 0.02	0.43 ± 0.03
$0.92 < Y < 1.54$	2.59 ± 0.14	0.28 ± 0.02	0.41 ± 0.03
$1.54 < Y < 2.15$	2.61 ± 0.15	0.23 ± 0.02	0.40 ± 0.03
$2.15 < Y < 2.77$	2.57 ± 0.19	0.20 ± 0.02	0.38 ± 0.03
$2.77 < Y < 3.38$	2.41 ± 0.26	0.16 ± 0.02	0.34 ± 0.04
$3.38 < Y < 4.0$	2.14 ± 0.28	0.12 ± 0.02	0.31 ± 0.05

Table 9.1: *$1/N\, dn/dY$ for the Y and p_t bins shown for the low Q^2 data sample. The error is the sum of statistical and systematic errors added in quadrature.*

Y Range	$1/N\ dn/dY$		
	$0.3 < p_t < 0.6$	$0.15 < p_t < 0.3$ GeV	$p_t < 0.15$ GeV
$-4.0 < Y < -3.38$	–	–	0.0003 ± 0.0003
$-3.38 < Y < -2.77$	–	0.0006 ± 0.0015	0.003 ± 0.002
$-2.77 < Y < -2.15$	0.004 ± 0.002	0.009 ± 0.003	0.012 ± 0.004
$-2.15 < Y < -1.54$	0.033 ± 0.008	0.047 ± 0.009	0.039 ± 0.008
$-1.54 < Y < -0.92$	0.16 ± 0.02	0.13 ± 0.02	0.10 ± 0.01
$-0.92 < Y < -0.31$	0.41 ± 0.04	0.30 ± 0.03	0.20 ± 0.02
$-0.31 < Y < 0.31$	0.68 ± 0.05	0.49 ± 0.04	0.30 ± 0.02
$0.31 < Y < 0.92$	0.81 ± 0.05	0.62 ± 0.04	0.35 ± 0.03
$0.92 < Y < 1.54$	0.86 ± 0.05	0.66 ± 0.04	0.39 ± 0.04
$1.54 < Y < 2.15$	0.87 ± 0.05	0.70 ± 0.04	0.42 ± 0.05
$2.15 < Y < 2.77$	0.86 ± 0.06	0.71 ± 0.06	0.42 ± 0.05
$2.77 < Y < 3.38$	0.79 ± 0.09	0.70 ± 0.08	0.42 ± 0.06
$3.38 < Y < 4.0$	0.72 ± 0.10	0.63 ± 0.09	0.38 ± 0.09

Table 9.2: *$1/N\, dn/dY$ for the Y and p_t bins shown for the low Q^2 data sample. The error is the sum of statistical and systematic errors added in quadrature.*

Y Range	$1/N\ dn/dY$		
	All p_t	$p_t > 1.0$ GeV	$0.6 < p_t < 1.0$ GeV
$-4.0 < Y < -3.38$	0.04 ± 0.01	0.0002 ± 0.0003	0.0006 ± 0.0007
$-3.38 < Y < -2.77$	0.13 ± 0.03	0.002 ± 0.001	0.010 ± 0.004
$-2.77 < Y < -2.15$	0.39 ± 0.07	0.016 ± 0.004	0.05 ± 0.01
$-2.15 < Y < -1.54$	0.96 ± 0.16	0.07 ± 0.01	0.16 ± 0.03
$-1.54 < Y < -0.92$	1.77 ± 0.22	0.22 ± 0.04	0.31 ± 0.04
$-0.92 < Y < -0.31$	2.51 ± 0.17	0.43 ± 0.03	0.43 ± 0.03
$-0.31 < Y < 0.31$	2.84 ± 0.16	0.52 ± 0.04	0.48 ± 0.03
$0.31 < Y < 0.92$	2.80 ± 0.16	0.45 ± 0.03	0.46 ± 0.03
$0.92 < Y < 1.54$	2.72 ± 0.18	0.39 ± 0.03	0.44 ± 0.03
$1.54 < Y < 2.15$	2.70 ± 0.19	0.30 ± 0.02	0.42 ± 0.03
$2.15 < Y < 2.77$	2.47 ± 0.23	0.21 ± 0.02	0.36 ± 0.03
$2.77 < Y < 3.38$	2.29 ± 0.25	0.17 ± 0.02	0.33 ± 0.04
$3.38 < Y < 4.0$	1.79 ± 0.31	0.11 ± 0.04	0.19 ± 0.06

Table 9.3: *$1/N\ dn/dY$ for the Y and p_t bins shown for the high Q^2 data sample. The error is the sum of statistical and systematic errors added in quadrature.*

Y Range	$1/N\ dn/dY$		
	$0.3 < p_t < 0.6$	$0.15 < p_t < 0.3$ GeV	$p_t < 0.15$ GeV
$-4.0 < Y < -3.38$	0.005 ± 0.003	0.013 ± 0.005	0.016 ± 0.005
$-3.38 < Y < -2.77$	0.036 ± 0.008	0.04 ± 0.01	0.041 ± 0.009
$-2.77 < Y < -2.15$	0.13 ± 0.02	0.11 ± 0.02	0.09 ± 0.02
$-2.15 < Y < -1.54$	0.32 ± 0.06	0.25 ± 0.04	0.15 ± 0.02
$-1.54 < Y < -0.92$	0.57 ± 0.07	0.42 ± 0.05	0.24 ± 0.03
$-0.92 < Y < -0.31$	0.78 ± 0.06	0.55 ± 0.05	0.32 ± 0.02
$-0.31 < Y < 0.31$	0.85 ± 0.05	0.64 ± 0.04	0.37 ± 0.03
$0.31 < Y < 0.92$	0.86 ± 0.05	0.65 ± 0.04	0.41 ± 0.04
$0.92 < Y < 1.54$	0.86 ± 0.05	0.65 ± 0.05	0.41 ± 0.05
$1.54 < Y < 2.15$	0.86 ± 0.06	0.70 ± 0.05	0.46 ± 0.05
$2.15 < Y < 2.77$	0.83 ± 0.08	0.68 ± 0.07	0.41 ± 0.05
$2.77 < Y < 3.38$	0.76 ± 0.09	0.64 ± 0.08	0.43 ± 0.06
$3.38 < Y < 4.0$	0.70 ± 0.13	0.55 ± 0.12	0.16 ± 0.18

Table 9.4: *$1/N\ dn/dY$ for the Y and p_t bins shown for the high Q^2 data sample. The error is the sum of statistical and systematic errors added in quadrature.*

Q^2 Range	$1/N\ Edn^{\pm}/d^3p$ (GeV^{-2})					
(GeV^2)	$0.3 < E < 0.5$	$0.5 < E < 0.7$	$0.7 < E < 0.9$	$0.9 < E < 1.1$	$1.1 < E < 1.3$	$1.3 < E < 1.5$
12-15	0.78 ± 0.10	0.20 ± 0.03	0.066 ± 0.01	0.028 ± 0.007	0.012 ± 0.004	0.0057 ± 0.003
15-20	0.87 ± 0.11	0.23 ± 0.03	0.091 ± 0.01	0.038 ± 0.007	0.018 ± 0.004	0.0079 ± 0.003
20-40	1.01 ± 0.11	0.29 ± 0.03	0.12 ± 0.02	0.056 ± 0.008	0.026 ± 0.005	0.014 ± 0.002
40-60	1.16 ± 0.12	0.35 ± 0.04	0.16 ± 0.02	0.075 ± 0.008	0.040 ± 0.005	0.023 ± 0.003
60-80	1.28 ± 0.14	0.42 ± 0.05	0.18 ± 0.02	0.093 ± 0.01	0.054 ± 0.007	0.032 ± 0.004
80-100	1.23 ± 0.14	0.41 ± 0.05	0.18 ± 0.02	0.10 ± 0.01	0.057 ± 0.008	0.037 ± 0.005
100-175	1.61 ± 0.22	0.40 ± 0.06	0.23 ± 0.04	0.10 ± 0.02	0.066 ± 0.01	0.04 ± 0.01
175-250	1.50 ± 0.17	0.55 ± 0.06	0.28 ± 0.03	0.13 ± 0.02	0.073 ± 0.01	0.048 ± 0.007
250-450	1.67 ± 0.18	0.56 ± 0.06	0.28 ± 0.03	0.16 ± 0.02	0.10 ± 0.01	0.060 ± 0.007
450-1000	1.80 ± 0.19	0.59 ± 0.06	0.31 ± 0.03	0.16 ± 0.02	0.11 ± 0.01	0.078 ± 0.009
1000-2000	1.90 ± 0.22	0.58 ± 0.07	0.33 ± 0.04	0.19 ± 0.02	0.11 ± 0.01	0.081 ± 0.010
2000-8000	1.97 ± 0.25	0.63 ± 0.08	0.39 ± 0.05	0.22 ± 0.03	0.15 ± 0.02	0.11 ± 0.018

Table 9.5: *$1/N\ Edn^{\pm}/d^3p$ for the E and Q^2 intervals shown. The error is the sum of statistical and systematic errors added in quadrature.*

Q^2 Range	$1/N\ dn^{\pm}/d^3p$ (GeV^{-3})					
(GeV^2)	$0.1 < p < 0.3$	$0.3 < p < 0.5$	$0.5 < p < 0.7$	$0.7 < p < 0.9$	$0.9 < p < 1.1$	$1.1 < p < 1.3$
12-15	3.97 ± 0.57	0.83 ± 0.1	0.23 ± 0.04	0.065 ± 0.01	0.024 ± 0.007	0.0081 ± 0.004
15-20	4.31 ± 0.61	0.94 ± 0.1	0.26 ± 0.04	0.087 ± 0.02	0.031 ± 0.006	0.014 ± 0.003
20-40	5.00 ± 0.60	1.17 ± 0.14	0.33 ± 0.04	0.12 ± 0.02	0.047 ± 0.007	0.020 ± 0.003
40-60	5.83 ± 0.63	1.35 ± 0.14	0.41 ± 0.04	0.16 ± 0.02	0.064 ± 0.007	0.030 ± 0.004
60-80	6.23 ± 0.70	1.53 ± 0.17	0.50 ± 0.06	0.19 ± 0.02	0.081 ± 0.01	0.039 ± 0.005
80-100	6.37 ± 0.75	1.42 ± 0.16	0.52 ± 0.06	0.17 ± 0.02	0.092 ± 0.01	0.044 ± 0.006
100-175	8.33 ± 1.4	1.77 ± 0.27	0.45 ± 0.08	0.24 ± 0.04	0.11 ± 0.02	0.045 ± 0.01
175-250	6.65 ± 0.81	1.85 ± 0.21	0.68 ± 0.08	0.29 ± 0.04	0.11 ± 0.01	0.060 ± 0.008
250-450	7.58 ± 0.82	2.03 ± 0.22	0.71 ± 0.08	0.28 ± 0.03	0.14 ± 0.02	0.078 ± 0.009
450-1000	8.51 ± 0.92	2.13 ± 0.23	0.71 ± 0.08	0.34 ± 0.04	0.15 ± 0.02	0.090 ± 0.01
1000-2000	9.46 ± 1.1	2.00 ± 0.23	0.77 ± 0.09	0.35 ± 0.04	0.17 ± 0.02	0.095 ± 0.01
2000-8000	9.43 ± 1.3	2.10 ± 0.28	0.77 ± 0.1	0.38 ± 0.06	0.21 ± 0.03	0.12 ± 0.02

Table 9.6: *$1/N\ dn^{\pm}/d^3p$ for the p and Q^2 intervals shown. The error is the sum of statistical and systematic errors added in quadrature.*

Chapter 10

H1 Data Analysis Conclusions

Corrected thrust, rapidity, pseudo–rapidity and invariant energy distributions have been produced in the Breit frame of reference and compared to theoretical predictions.

Thrust (T_z) distributions are plotted as a function of the summed calorimeter cluster four momentum vectors in the current hemisphere of the Breit frame, divided by Q (E_{BF}/Q). These plots are used to determine the proportion of BGF events in the data as a function of x. The method for determining the BGF fraction in the data is Monte Carlo dependent and unfortunately gives inconsistent results. Despite this, the BGF fraction does appear to rise as x decreases as expected.

Rapidity distributions were examined over a range of p_t in the Breit frame. The MEAR (Colour Dipole Model) Monte Carlo gave a good description of the data over most of the Y range for all p_t intervals. However, Monte Carlos utilising Soft Colour Interactions did not describe the data well, particularly in the target region at intermediate p_t values. At high p_t models that are similar to the BFKL formalism describe the data better than models similar to the DGLAP formalism. No evidence for the existence of a predicted plateau in the current hemisphere at low p_t was found.

Invariant distributions have been presented for the current hemisphere of the Breit frame and compared to MLLA/LPHD predictions made for e^+e^- experiments. Q is taken as being equivalent to the e^+e^- centre of mass energy, E^*. The discrepancy between the data and MLLA/LPHD predictions becomes greater at low Q^2 and higher energies, E, and is attributed to contributions from leading order, especially boson-gluon fusion, diagrams. At the higher Q values the data show a clear tendency to approach a common limit at low particle energy, independent of Q and in agreement with the prediction. The

data are incompatible with predictions made using a fixed value of α_s.

Bibliography

[1] HERA, A Proposal for a Large Electron–Proton Colliding Beam Facility at DESY, DESY HERA 81–10(1981).

[2] H1 Collaboration, I. Abt et al., Nucl. Instr. and Meth. A 386 (1997) 310-347.

[3] H1 Collaboration, I. Abt et al., Nucl. Instr. and Meth. A 386 (1997) 348-396.

[4] H1 Collaboration, XXVIII ICHEP, Warsaw, July 25–31 1996, pa17–026

[5] Yu. L. Dokshitzer, Sov. Phys. JETP 46 (1977) 641.
V. N Gribov and L. N. Lipatov, Sov J. Nucl. Phys. 15(1972) 438, 675.
G. Alterelli ang G. Parisi, Nucl. Phys. B 126 (1977) 298.

[6] H1 Collaboration, T. Ahmed et al., Nucl. Phys. 439B (1995) 471.

[7] Zeus Collaboration, M. Derrick et al., Zeit. Phys. C65 (1995) 379.

[8] E. A. Kuraev, L. N. Lipatov and V. S. Fadin, Sov. Phys. JETP 45 (1977) 199.
Y. Y. Balitsky and L. N. Lipatov, Sov. J. Nucl. Phys. 28 (1978) 822.

[9] H1 Collaboration, S. Aid et al., Phys. Lett. 470B (1996) 3.

[10] H1 Collaboration, T. Ahmed et al., Nucl. Phys. B429 (1994) 477.

[11] Zeus Collaboration, M. Derrick et al., Phys. Lett B315 (1993) 481.

[12] H1 Collaboration, C. Adloff et al., Z. Phys. C74 (1997) 191.

[13] Zeus Collaboration, J. Breitweg et al., Z. Phys. C74 (1997) 207.

[14] R. P. Feynman Phys Rev Lett 23, 1415 (1969).

[15] J. D. Bjorken and E. A. Paschos, Phys. Rev. 185 (1969), 1975.

[16] G. Altarelli and G. Parisi, Nucl. Phys. B 126 (1977) 297.

[17] G. Gustafson, Phys. Lett. 175B (1986) 453.
G. Gustafson, U. Pettersson, Nucl. Phys. 306B (1988) 746.
B. Andersson, G. Gustafson, L. Lönnblad, U. Pettersson, Zeit. Phy. C43 (1989) 625.
B. Andersson, G. Gustafson, L. Lönnblad, Nucl. Phys. 339B (1990) 393.

[18] L. Lönnblad, Compt. Phys. Commun. 71 (1992) 15.

[19] OPAL Collaboration, M. Z. Akray et al., Zeit. Phys. C47 (1990) 505.

[20] Proceedings of the Workshop "Physics at HERA", edited W. Buchmuller and G. Ingleman, Hamburg, Germany, Vol. 3 (1992).

[21] T. Sjöstrand, "Pythia 5.7 and Jetset 7.4 Physics and Manual", CERN-TH.7112/93 (1993)

[22] Ya. I. Azimov, Yu. L. Dokshitzer, V. A. Khoze and S. I. Troyan, Zeit. Phys. C31 (1986) 213.
L. V. Gribov, Yu. L. Dokshitzer, V. A. Khoze and S. I. Troyan, Phys. Lett B202 (1988) 276.

[23] R. P. Feynman and R. D. Field, Nucl. Phys. 136B (1978) 1.

[24] G. Marchesini et al., Comput. Phy. Commun. 67 (1989) 13.

[25] G. Ingelman, A. Edin, J. Rathsman, LEPTO 6.5 – A Monte Carlo Generator for Deep Inelastic Lepton-Nucleon Scattering. DESY 96-057 (1996).

[26] K. T. Donovan and G. Thompson, Z. Phys. C73, (1997) 641.

[27] ZEUS Collaboration, XXVIII ICHEP, Warsaw, July 25–31 1996, pa02–043

[28] H1 Collaboration, S. Aid et al., Nuclear Physics B 449 (1995) 3.

[29] J.E. Huth et al., Research Directions for the Decade, Snowmass, (1990), World Scientific, Singapore.

[30] JADE Collaboration, W. Bartel et al., Z. Phys. 33 (1986) 23.

[31] N. Brown and W.J. Stirling, Z. Phys. C53 (1992) 629.

[32] CDF Collaboration, F. Abe et al, Phys. Rev. D45 (1992) 1448.

[33] S.D. Ellis, J. Phys. G17 (1991) 1552.

[34] L.A. del Pozo, Ph.D. Thesis, Cambridge University, (1993).

[35] G. Giacomelli and M. Jacob, Phys. Rep. 55 (1979) 38.

[36] C. Schwanenberger, "Systematische Untersuchung von Jetprofilen in harten gamma-p-Streuprozessen bei HERA", Diplom Thesis, University of Heidelberg.

[37] R.P. Feynman, Phys. Rev. Lett. 23 (1969) 1415.

[38] V. Hedberg et al., Z. Phys. C63 (1994) 49.

[39] H1 Collaboration, S. Aid et al., Zeitschrift für Physik C70 (1996) 17.

[40] Zeus Collaboration, XXVIII ICHEP, Warsaw, July 25–31 1996, pa02–040.

[41] UA1 Collaboration, G. Arnison et al., Physics Letters 132B (1983) 214.

[42] UA1 Collaboration, C. Albajar et al., Nuclear Physics B309 (1988) 405.

[43] Proceedings of the Workshop "Physics at HERA", edited W. Buchmuller and G. Ingleman, Hamburg, Germany, Vol. 1 (1992).

[44] U. Bassler, "Premiere mesure sur l'etat final hadronique de la diffusion profondement inelastique a HERA," Dissertation, Univ. de Paris VI (1993).

[45] H1 Collaboration, T. Ahmed et al., Nucl. Instrum. Methods A361 (1995) 197.

[46] D. Traynor, private communication.

[47] V. N. Gribov, Proceedings of the VIII Winter School of the LNPI. Vol. 2, Leningrad (1973).

[48] V. A. Khoze, S. Lupia, W. Ochs, Phys. Lett. B394 (1997) 179.

[49] W. Ochs, Proc. of the Ringberg workshop "New Trends in HERA Physics", Tegernsee, Germany, 25-30 May 1997. hep-ph/9709248.

[50] R. Brun et al., GEANT long writeup, CERN Program Library, W5103 (1989).

[51] S. Bethke, Proceedings QCD 94, Montpellier, ed. S. Narison, Nucl. Phys. B (Proc. Suppl.) (1995), 198.

[52] H1 Collaboration, C. Adloff et al., Phys. Lett. B406 (1997) 256.

[53] R. K. Griffiths, "The First Measure of Relative Partonic Contributions in DIS at HERA using an Average Hadronic Charge," University of London thesis, (1998).

[54] D. Kant, Nuc. Phys B (Proc. Suppl.) 71 (1999) 31.

[55] V. A. Khoze, S. Lupia and W. Ochs, "Perturbative Universality in Soft Particle Production," CERN-TH/97-199.

[56] V. A. Khoze and W. Ochs, "Perturbative QCD approach to Multiparticle Production," Durham DTP/96/36.

[57] H1 Collaboration, C. Adloff et al., Nuc. Phys. B485 (1997) 3.

[58] W. Ochs, private communication.

[59] S. Lupia, private communication.

[60] H1 Collaboration, C. Adloff et al., Nuc. Phys. B504 (1997) 3.

[61] H1 Collaboration, C. Adloff et al., 29th International Conference on High Energy Physics ICHEP98, Vancouver, Canada, July 1998. No. 531

[62] J. V. Morris, private communication.

Acknowledgements

This has turned out to be the most difficult section to write. First of all I'd like to thank my supervisor Graham Thompson for his help over the last three years. I should also acknowledge PPARC for their financial support - money well spent.

Other members of staff I have to thank are Murrough and Paul (K) for expertly looking after the computers, Michael for knowing exactly when tea is, Dave for his code, Simon for knowing when to go for a tasty kebab, Alex for showing us all the value of linux, and special thanks to Paul (D) for sorting out my computer problems both at work and at home. Thanks should also go to Peter Crew & Ted Lee, Paul Harrison, and Steve Lloyd. I must also mention Derek whom we all miss greatly - the lab is not the same without him.

I would also like to thank the various members of the group that is known as BHAG, without whom my work would have been considerably harder and who had to sit through my numerous talks.

My thesis wouldn't be complete without saying a big thanks to all my terminal room colleagues both past and present. So in some sort of order here goes. Cheers to Andy, Thanos, James for his friendliness, Iain, Andrew for his answers to quick questions, Eram, Rob for training me to be SpaCal expert (Ha Ha!), Martin for his T-shirts, Dan, Caroline for her devotion to salsa and her singing, Andrew (Caines) for giving us years of gossip, Dai, John, Kostas for answering the phone, Dan, Dan for being the SpaCal expert (Ha Ha!) and (my replacement) John.

I must also say cheers to Simon who put up with Faye and I for the last three years and, despite several attempts, managed not to burn our house down.

Finally I must thank three other people, my parents for their love and encouragement and my soulmate Faye for her love, support and inspiration.